TOWARDS A PERSONALISED BIOMECHANICAL TONGUE MODEL

sEMG measurements on the tongue and motor unit identification

E.S. van Staveren

TOWARDS A PERSONALISED BIOMECHANICAL TONGUE MODEL

E.S. van Staveren

December 2017

ANTONI VAN LEEUWENHOEK

NEDERLANDS KANKER INSTITUUT

UNIVERSITY OF TWENTE.

TOWARDS A PERSONALISED BIOMECHANICAL TONGUE MODEL

sEMG measurements on the tongue and motor unit identification

Eline S. van Staveren
Technical Medicine – Medical Sensing and Stimulation
November 2016 – December 2017

UNIVERSITY OF TWENTE.

ANTONI VAN LEEUWENHOEK
NEDERLANDS KANKER INSTITUUT

Masters Graduation Committee

Chairman and external member	Prof.dr.ir. H.J. Hermens Department of Biomedical Signals and Systems / Telemedicine Cluster University of Twente, Enschede, The Netherlands
Clinical supervisor	Prof.dr. L.E. Smeele Department of Head and Neck Oncology and Surgery Netherlands Cancer Institute, Amsterdam, The Netherlands
Technical Supervisor	Dr.ir. F. van der Heijden MIRA institute for Biomechanical Engineering and Technical Medicine University of Twente, Enschede, The Netherlands
Mentor	B.J.C.C. Hessink-Sweep, Msc. Technical Medicine University of Twente, Enschede, The Netherlands
Additional member	M. Eskes, Msc. Department of Head and Neck Oncology and Surgery Netherlands Cancer Institute, Amsterdam, The Netherlands

ABSTRACT

[Background] The Virtual Therapy Consortium is working on a functional predictive tool to facilitate evidence-based decisions on cancer treatment proposals. For this purpose, a biomechanical model is under development. The biomechanical model will contain high quality 3D animations incorporating patient specific anatomy, physiology, and neuromuscular information. In the case of tongue cancer, it is desired that the model demonstrates patient specific treatment effects on functions as mastication, swallowing, and audible speech. To accomplish these simulations a personalised tongue model is essential. **[Objective]** The goal of this thesis was to make the first steps towards addition of neuromuscular information to a generic biomechanical tongue model, for personalisation purpose. **[Methods]** The first step incorporated the development of an electrode setup to measure tongue muscle activation, using the patient-friendly surface electromyography (sEMG). Different electrode setups, using both current materials and new prototypes, were tested for technical and practical suitability. The two best performing grids were applied in an experiment with one healthy subject for tongue sEMG quality evaluation. To distinguish activation of individual tongue muscles, the second step involved identification of motor unit action potential trains (MUAPTs), referred to as decomposition. The recently developed sEMG decomposition approach (KmCKC) of Ning et al. [1] was analysed, optimised and tested on simulated EMGs. This decomposition method was also applied to the experimental tongue sEMG. The third step involved evaluation of the MUAPT propagation patterns for allocation of motor units to individual tongue muscles. **[Results]** In total, five electrode setups (three current materials and two new prototypes) were evaluated for nine formulated requirements. The existent ECoG grid and prototype Silic-12 grid appeared to be most promising for tongue measurements. During the experiment, the Silic-12 grid showed fewer dislocation artefacts in the tongue sEMG. In the second step, the KmCKC decomposition method showed reasonable results for MUAPT identification in simulated EMGs and provided insight in parameter settings. Unfortunately, its performance in the tongue sEMG could not be verified. The MUAPT propagation patterns over the Silic-12 electrodes allowed some tentative allocations of MU activities to specific superficial intrinsic tongue muscles. **[Conclusion]** The combination of sEMG measurements on the tongue with the Silic-12 grid and KmCKC decomposition algorithm showed potential for acquisition of neuromuscular information from the superficial intrinsic tongue muscles. Some major improvements should be made in future research before translation to input for the biomechanical tongue model can be initiated.

TABLE OF CONTENTS

CHAPTER 1 INTRODUCTION

Oral and pharyngeal cancer is a serious and growing problem worldwide, grouped together it is the sixth most common cancer in the world [2]. In Europe and the United States the tongue is the most common site for intraoral cancer, amounting 40-50% of oral cancers [2]. In the Netherlands, this entailed 395 new patients with tongue cancer in 2016 [3]. Currently, the first treatment of choice is surgery, with adjuvant radiotherapy if needed [4]. In addition, organ sparing therapies like chemotherapy, radiotherapy and photodynamic therapy are non-surgical options. Selection of a treatment for tongue carcinomas is based on knowledge, experience and intuition of the physician and multidisciplinary tumour board. However, the extent of functional loss differs per treatment, patient and tumour. Prediction of patient specific functional loss per treatment can be of great value.

The Virtual Therapy Consortium [5] is a collaboration of universities and hospitals that addresses this problem. Its mission is to create evidence-based foundations for treatment choices concerning not only head and neck cancer patients, but for each cancer patient where treatments could impair function. The goal is to construct a personalised, detailed, high resolution biomechanical model of each individual patient, a genuine virtual look-alike. The biomechanical model will contain high quality 3D animations incorporating anatomy, physiology, and neuromuscular information based on the patients' data from medical imaging and other biomechanical technologies. In the case of a patient with head and neck cancer, audio-visual dynamic representations of the functional sequelae due to different curative treatment options will be realized. In the future, this virtual patient demonstrates the effect on functions as mastication, swallowing, and audible speech. This functional predictive tool should facilitate evidence-based decisions on treatment proposals.

This master thesis will focus on adding neuromuscular information to the biomechanical model. This was done already for facial muscles affecting lip motion [6]. Another important muscle category is tongue musculature since its essential role in articulation, guiding food for mastication, squeezing food into the oropharynx as part of swallowing and oral cleansing [7]. The goal of this thesis was to make the first steps for addition of neuromuscular information in order to personalise a generic biomechanical tongue model (Figure 1.1). This goal entailed the following research questions:

- Is it possible to acquire sEMG signals from the tongue?

  Acquisition of surface electromyography (sEMG) from the tongue is much more challenging than extraoral sEMG acquisition. Since the tongue is a highly mobile and flexible anatomical structure, involving large variation in surface curvatures in a short amount of time. Moreover, the intraoral environment is very wet. A stable and reliable attachment of electrodes is therefore a challenge.

- Can the activities of different motor units in the tongue musculature be distinguished by decomposition of tongue sEMG?

  Since sEMG measures the activation of multiple tongue muscles together, a principle component problem arises for the identification of individual tongue muscle activation. Decomposition of the tongue sEMG into individual motor unit activities might be the first step towards identification of these individual tongue muscle activities.

- To what extent does tongue sEMG allow determination of the direction of muscle fibres belonging to one motor unit? And would it be possible to allocate the individual motor unit activities to a specific tongue muscle?

  The individual tongue muscles differ from each other in their muscle fibre directions and thus often intertwine. Observation of motor unit activity propagation on an electrode grid may help to associate the different motor unit activities to individual tongue muscles.

The first two steps are this thesis' main focus, however a first exploration for the third step is included. The needed background information is provided by Chapter 2. Chapter 3 is about the first step, development of a sEMG electrode setup and experiments on the tongue are described. Chapter 4 (second step) introduces a decomposition algorithm and reports about tests on simulated EMGs. All three steps are addressed in Chapter 5, here an experiment with a healthy subject is described. This experiment incorporates electrode grids, decomposition and anatomical interpretation. Chapter 6 and 7 provide a conclusion and future perspectives.

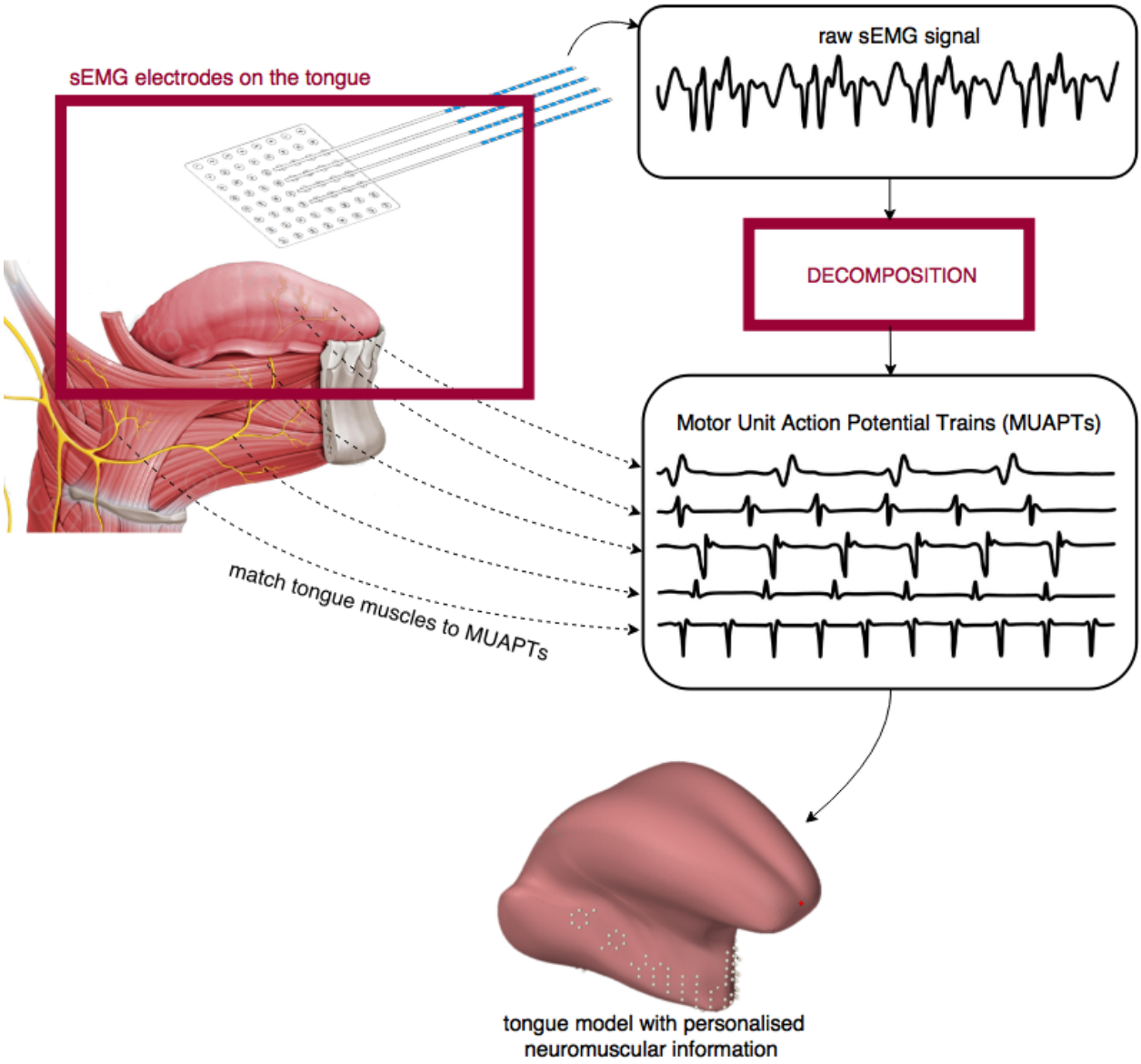

Figure 1.1 - Flowchart for achieving the final research goal. The red framed components represent the main points of focus (step 1 and 2) for this master thesis. [7][8]

2.1 ANATOMY

The tongue is essentially a mass of muscles and is covered by mucous membrane, containing numerous small lingual papillae. Due to the presence of multiple tongue muscles, it can assume a variety of shapes and positions. The muscles of the tongue do not act in isolation and some muscles include parts that can act independently, producing different, even antagonistic actions. In general, two muscle groups can be distinguished, extrinsic and intrinsic muscles. [7]

The four extrinsic muscles alter the position of the tongue, but they can change its shape as well. These muscles originate outside the tongue, with a proximal bone attachment and a distal attachment on the tongue (Figure 2.1). The m. genioglossus (GG) is biggest muscle of the tongue and is fan-shaped. When activated bilaterally the central part of the tongue depresses; activation of the posterior part pulls the tongue anteriorly for protrusion; activation of the most anterior part retracts the apex of a protruded tongue; and unilateral contraction deviates the tongue to the contralateral side. The m. hyoglossus (HG) is a thin muscle that depresses and retrudes the tongue base. The m. styloglossus (SG) is a small, short triangular muscle interdigitating with the m. hyoglossus. When contracted the muscle retrudes the tongue and elevates its sides. The fourth extrinsic muscle is the m. palatoglossus (PG), a narrow muscle capable of elevating the posterior part of the tongue and depressing the soft palate. [7]

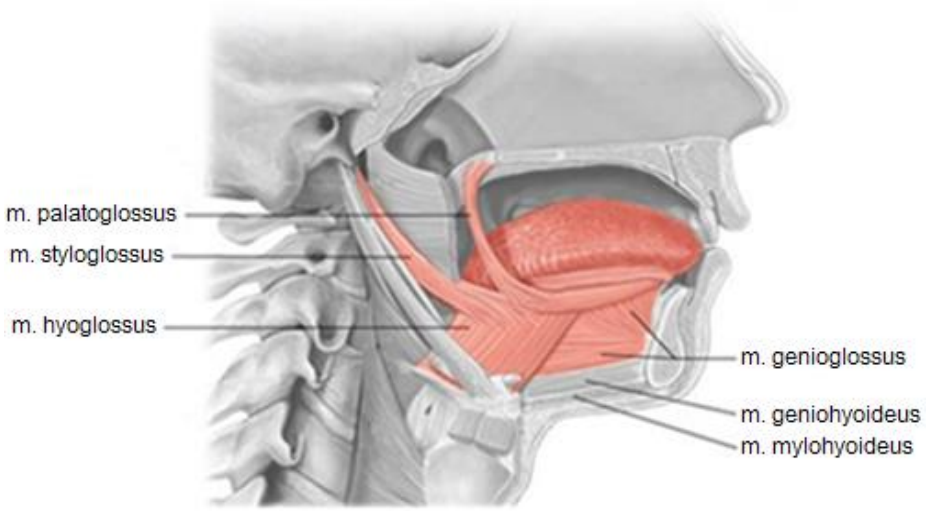

Figure 2.1 - Sagittal view of the tongue. The tongue and its four extrinsic muscles are depicted in color. The muscles forming the floor of the oral cavity are depicted in black and white. [9]

The four intrinsic muscles alter the shape of the tongue and are attached entirely within the tongue (Figure 2.2). The m. longitudinalis superior (SL) and inferior (IL) both shorten and thicken the tongue to retract. The m. longitudinalis superior is a thin superficial layer close to the mucous membrane and besides participation in retraction it elevates the apex and sides of the tongue. The m. longitudinalis

inferior is a narrow band close to the inferior surface of the tongue, performing depression of the apex. The m. tranversus (T) and verticalis (V) linguae consist of intersecting fibres acting simultaneously to protrude the tongue. Where the m. transversus linguae narrows and elongates and the m. verticalis linguae flattens and broadens the tongue. [7]

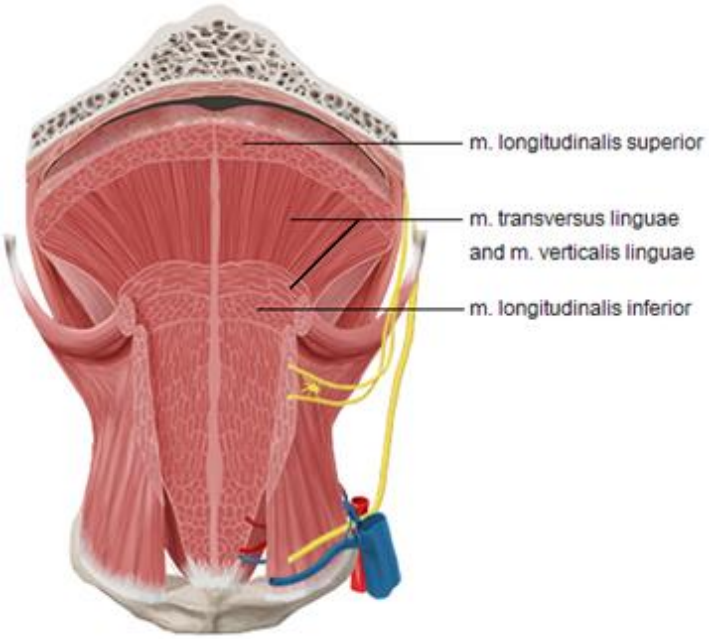

Figure 2.2 – Coronal view of the tongue. The tongue's surface and its four intrinsic muscles are depicted. [10]

All the muscles of the tongue receive motor innervation from the n. hypoglossus (XII), except for PG muscle which is supplied by the pharyngeal plexus [7]. The motor innervation of tongue muscles by the hypoglossal (XII) nerve has still not been described in detail. Moreover, tongue muscles have complex innervation with many terminal nerves entering single muscles. Mu and Sanders [11] researched the distribution of the XII nerve supply inside the tongue and the arrangement of motor endplates (MEPs) within each muscle. For this purpose, five adult human tongue specimens were assessed, exhibiting similar nerve branching and distribution patterns (Figure 2.3). The XII nerve enters the tongue at the ventrolateral aspect of the posterior tongue, bilaterally. The first split off occurs when the dorsal surface of the HG muscle is reached, this branch innervates the GH muscle. Then the XII nerve divides into its lateral (l-XII) and medial (m-XII) branches. The l-XII branching consists of two types, single and multiple branching. Single branching implies a short main trunk (~2 mm) followed by several branches to innervate the SL, SG, HG, and lateral IL muscles. Multiple branching involves the XII nerve which gives off multiple l-XII branches at different points on the nerve XII main trunk. The m-XII branches turn medially at the anterior edge of the HG muscle, cranially after passing between the two GG layers and anteriorly when T/V muscles are reached. The posterior third supplies the GG, posterior T and V (p-T/V), and medial IL muscles. At the level of the vallate papillae (VP) the m-XII splits off several branches, forming a dense

plexus to supply anterior T and V muscles (a-T/V). For sensation, the mucous membrane of the tongue is, among others, innervated by the n. lingualis (LN) and the lingual branch of the n. glossopharyngeus (IX). Besides sensory mediation, the most posterior LN branch seems to communicate with the l-XII nerve and supply innervation to the IL muscle. So, it is suggested that the LN contains motor axons as well. [11]

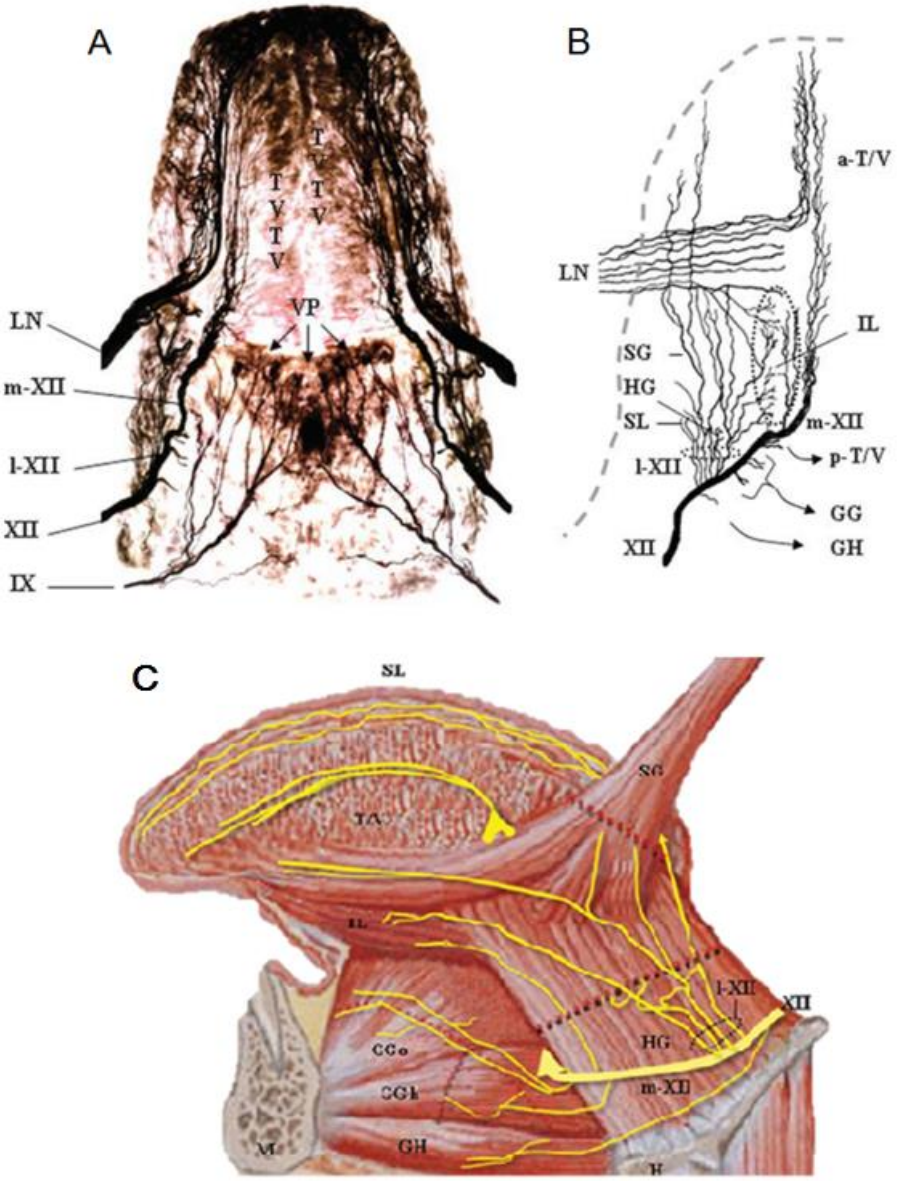

Figure 2.3 – Innervation of the tongue, according to Mu and Sanders. (A) Ventral view of the nerve map of an adult human tongue. The diameters of the main trunks were ranked LN > XII > IX. (B) Schematic drawing of nerve branching on the left hemi-tongue, ventral view. The horizontal oval indicates (multiple) branching of the l-XII nerve and the vertical oval shows the nerve supply pattern of the IL muscle. (C) Schematic illustration of the branching and distribution of the XII nerve, sagittal view. The locations of the motor endplate bands are indicated by dotted lines in the GG, HG, and SG. [11]

2.2 MODEL

The current tongue model has a surgery and radiation module for simulation of treatments and their functional consequences. Both treatment modules are still in development phase. The model consists of a biomechanical part and a visual part. The visual model translates the biomechanical simulation into a visual representation through a 3D surface mesh. The biomechanical model is created using the Finite Element Method (FEM), based on work of Buchaillard et al. [12]. They created a surface mesh that is filled up with small cubic shaped elements, forming a volume mesh (Figure 2.4 A). These elements contain properties like stress, strain, weight, and interactive behaviour, facilitating calculations on property changes of the complete tongue. Initially, different tongue musculature is indicated by fibres, spring-like structures, with the ability to pull their two endpoints towards each other (Figure 2.4 B). Elements in between these fibre endpoints are squeezed and not actively involved in muscle contraction. To overcome this physiological unrealistic situation, fibre muscles are converted to element muscles. All elements within a radius of two millimetres around a certain fibre are provided with contractile properties and directions. In this manner, muscle forces in the element muscles have the same direction as nearby fibres. [13]

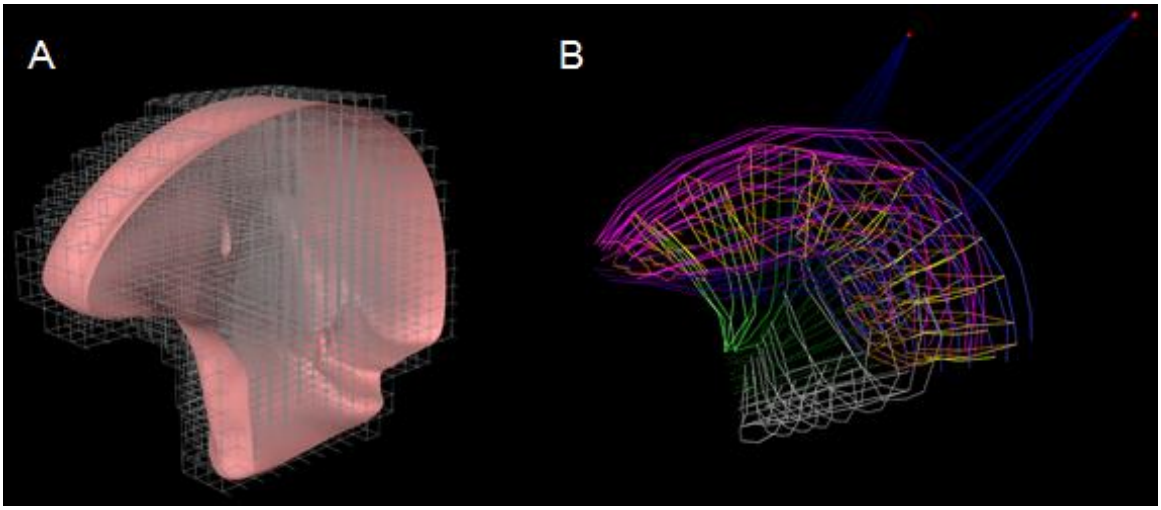

Figure 2.4 – The current tongue model. (A) Sagittal view of the 3D surface mesh, loaded with cubic FEM elements. (B) Lateral view of all 3D fibre muscles as defined by Buchaillard et al. [12], the colours indicate the different muscles. The PG muscles are not included. [13]

Two types of simulations can be generated with the tongue model, forward and inverse simulations. A forward simulation starts with manual activation of certain muscle fibres, resulting in a tongue model manoeuvre. Inverse simulation works in the opposite direction, a tongue manoeuvre is given and the corresponding combination of muscle fibre activation is calculated. The latter uses a cost function to find combinations of muscle activations. Since the solution to this problem is not unique, the found solution is not person-specific. Addition of person-specific EMG signals is one important step towards personalisation of these simulations. The cost function will receive an indication of where to look for its solution and EMG signals can be used as input for forward simulations.

2.3 EMG

EMG measures the algebraic summation of motor unit action potential trains (MUAPTs) from different active motor units within the electrode recording range [14]. A motor unit (MU) is defined as one motor neuron and all of the muscle fibres that it innervates (Figure 2.6) [16]. The number of muscle fibres per MU can vary from four to several hundred and each muscle is activated by at least one MU [15]. Each muscle fibre is activated via waves called 'intracellular action potentials' (IAP) which travel outward over the muscle fibre starting at the (motor) axon connection, roughly in the middle of the muscle fibre [17]. A MUAPT is the resultant depolarization wave of all the fibres (all IAPs together) in a particular MU [17]. And the summation of all MUAPTs forms the EMG signal.

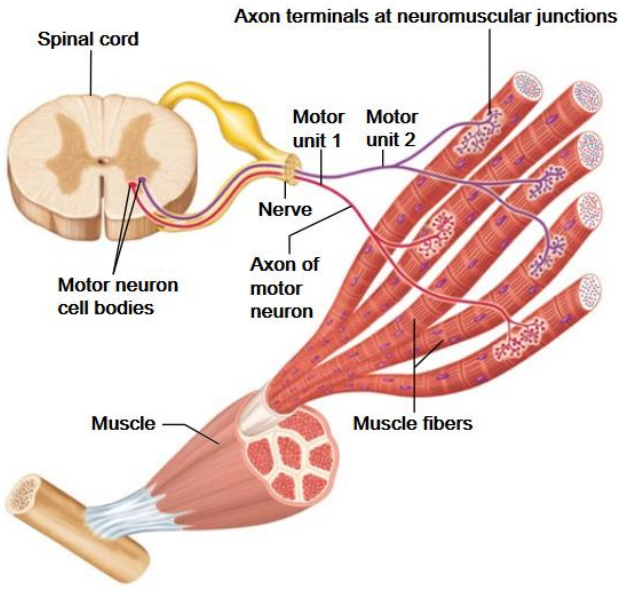

Figure 2.6 – Illustration of the MU definition. This specific muscle fibre bundle is innervated by two MUs. [15]

Figure 2.5 – sEMG of extrinsic and intrinsic tongue muscles with use of Ag/AgCl micro-electrodes. [27]

2.3.1 Previous tongue EMG measurements

The first EMGs of tongue muscles were acquired intramuscular with use of needle EMG [18][18][19][20]. The advantage of intramuscular EMG is some certitude of MUAPT origin. However, this method is invasive and therefore uncomfortable. This caused more recent studies to use sEMG, involving other difficulties. Surface EMG of the tongue entails attachment of electrodes in a wet and deforming environment and the necessity to distinct different MUAPTs, possibly originating from different muscles.

Only few studies performed sEMG measurements of tongue musculature. Three studies acquired sEMG of the GG muscle by placing electrodes under the tongue on the floor of the mouth, held in place by dental impression material on the mandibular teeth and mouth floor [21][22][23]. The oldest study concluded that the surface electrode satisfactorily reflects the bioelectric activity of the GG since the intramuscular

electrodes show similar patterns of muscle activity and highly coherent frequency spectra [21]. Another, more recent study, found that an unilateral configuration of two surface electrodes resulted in a more reliable estimate of GG activity compared to a bilateral configuration [23]. It is less sensitive to cross-talk from neighbouring muscles and artefacts due to non-propagating muscle fibre end-effects are reduced [23]. For measuring sEMG of intrinsic tongue muscles in humans, only a limited number of attempts is documented. Yoshida et al. [24] developed a surface electrode by painting a small dot with silver paste, adding a fine wire and a rubber cap on top. Two of these electrodes were used for measurements of the distal tongue musculature [24][25][26]. Recently, a colleague [27] used sintered disc shaped Ag/AgCl micro-electrodes for classification of different tongue movements (Figure 2.5), including extrinsic and intrinsic muscle measurements. Four electrodes were placed on the tongue with use of denture adhesive strips and four electrodes were placed submandibular, fixated with double-sided adhesives. Distinction between different tongue muscles appeared to be hard and inconclusive. It was recommended to develop a tongue-shaped flexible electrode array that can adhere to the tongue. The higher density of electrodes may enable distinction between MUAPTs originating from different tongue muscles.

2.4 DECOMPOSITION

Decomposition is defined as the process of separation into constituent parts. EMG can be decomposed into several constituent parts: time-frequency components [28], wavelet components [29], degrees-of-freedom force functions [30] or MUAPTs (Figure 1.1) [31]. The latter is the constituent part of interest for this thesis, since it provides information about individual motor units and therefore might facilitates muscle distinction (Figure 1.1). Decomposition of EMG requires that the MUAPs produced by the same motor unit are more similar in shape than the MUAPs produced by other motor units and that the MUAPs of each motor unit occur enough times without superposition, so their respective shapes can be determined [32]. These requirements involve many technical challenges, like excessive MUAP superposition, the large dynamic range of MUAP amplitudes, changes in action potential shape of a MU, and similar shaped MUAPs [31].

For decomposition of sEMG two main approaches are used [33]. The first approach is based on pattern recognition techniques for identification of recurrent MUAPs [33]. Gazzoni et al. [34] detected MUAPs with the use of the matched Continuous Wavelet Transform (CWT) followed by classification by a modified version of the multi-channel Adaptive Resonance Theory networks. The latter could adapt to slow changes in MUAP shape. This method showed the possibility of investigating anatomical and physiological properties of the detected MUs. However, the decomposition of MUAP superpositions was limited. Also the algorithm of Kleine et al. [35] could be improved for complex superposition situations. Their method consisted of two clustering steps, a Wards algorithm and an interactive clustering by manual inspection and adjustment. Here, both the spatial (waveform and amplitude differences between channels) and temporal (time-course of the potential in each channel) information of the high-density (HD) sEMG

were taken into account. MUAP templates were constructed from the assigned clusters, followed by template matching combined with a peel-off procedure (template subtraction from the EMG). An earlier version of this method [36] was used by Lapatki et al. [37] and demonstrated the valuable MUAP information after decomposition. The innervation zone and the main muscle fibre orientation of the MU were localized, corresponding to the location where the MUAP is generated and in which direction it propagates (Figure 2.7). A method performing better on the superposition problem is the one of Nawab et al. [31]. Their algorithm started with the identification of templates for the various MUAP shapes. Followed by an artificial intelligence technique, which searched for signal regions where the extracted templates are in superposition with each other or with unidentified MUAPs. Though, this required that the unidentified MUAPs account for less than 25% of the signal energy.

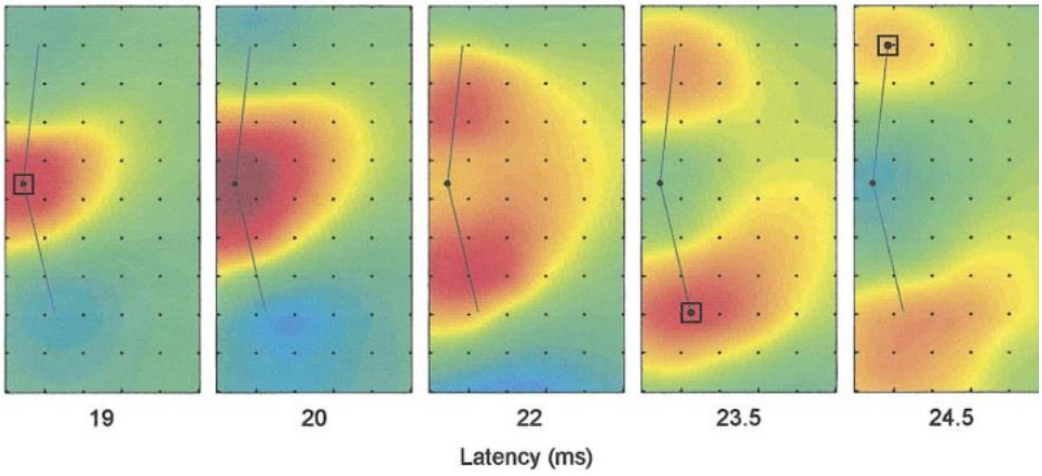

Figure 2.7 – Muscle fibre orientation after processing of propagating MUAP in the m. depressor anguli oris (DAO). Monopolar amplitude maps illustrate topographically the initiation of the potential (latencies 19 and 20) and its conduction in the upper and lower part of the DAO musle (latencies 22, 23.5 and 24.5). The dots in grid pattern are the sEMG electrode locations, the colour indicates the MUAP amplitude and the line with a dot in the middle is the muscle fibre direction with the motor neuron endplate, respectively. [37]

The second approach for sEMG decomposition entails blind-source separation techniques based on statistical properties of sEMG signals [33]. One popular and effective technique is Independent Component Analysis (ICA). Both Akazawa et al. [38] and Chen et al. [14] used ICA for decomposition of experimental sEMG. Here, Chen et al. [14] identified up to 19 MUAPTs with their FastICA peel-off framework. FastICA was used for MUAP waveform estimation and spike train identification. The resulting MUAPT was withdrawn from the original sEMG signal. This “peel off” strategy mitigated the effect of the already identified motor units on the FastICA convergence. So, more motor units could emerge. Another technique is the convolution kernel compensation (CKC) method, proposed by Holobar and Zazula [39], which estimates the innervation pulse trains (IPT) directly without calculating the unknown mixing matrix (matrix of impulse responses / MUAP shapes per electrode and per MU). Tests on simulated sEMG proved this technique to highly efficient since up to 30 MUs were completely reconstructed. Ning et al. [1]

developed a novel approach based on the classic CKC method. K-means clustering (KMC) is performed as an initial step to cluster the time instants fired by the same MU, followed by the CKC, which is modified with a novel multi-step iterative process to update the estimated MUAPTs iteratively. This K-means clustering – modified CKC (KmCKC) approach successfully reconstructed MUAPTs with high accuracy, at different levels of contraction. And it appeared to be robust against noise. During a test [1] on experimental sEMG of the first dorsal interosseous muscle, both the classic CKC and KmCKC method identified the first six MUs, but the last eight MUs could only be identified by the KmCKC approach.

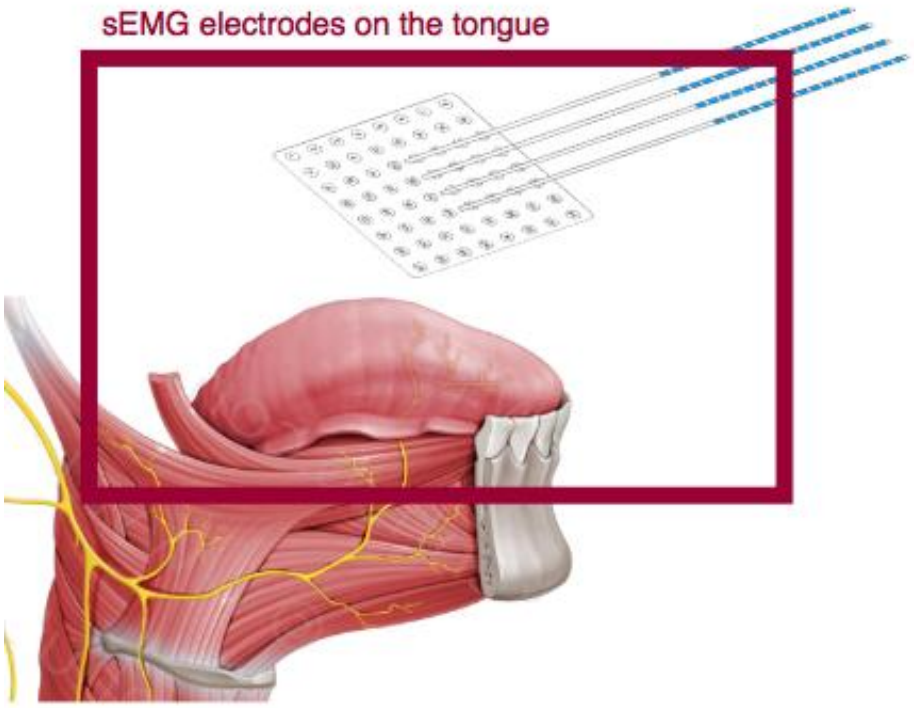
sEMG electrodes on the tongue

3.1 INTRODUCTION

This chapter addresses the exploration and development of a technique for surface electromyography (sEMG) measurements on the tongue. Being the first step towards addition of neuromuscular information to the biomechanical tongue model. In specific, the goal of this chapter is to find or develop one or more sEMG electrode setups with high potential for tongue measurements. This is done by selection of various current materials and development of new prototypes, which all were tested for the technical and practical requirements as formulated in advance.

3.2 REQUIREMENTS

An optimal electrode setup should be developed for sEMG measurements of tongue musculature. The setup requirements concern the subjects: use of a high density (HD) sEMG grid or multiple electrodes; electrode type; inter-electrode distance (IED); electrode pattern; fixation of electrodes on the mucous membrane of the tongue; tongue movement without restriction; in case of a grid, flexibility because of deformability of the tongue; cables should be suitable for sEMG signal conduction and it should be comfortable for the subject and affordable to a certain extent. All of these components together define practical use on the tongue and measurement properties. The technical considerations are outlined below and summarised together with the practical requirements (Table 3.1).

The electrodes for sEMG measurements are preferably miniature electrodes, with diameters below 5 mm, and specifically designed for EMG with an AgCl or Ag surface [40]. The advantage of skin-Ag or skin-AgCl contact is the almost resistive impedance in the EMG frequency range, while other metals present capacitive components involving additional filtering [41]. Furthermore, miniature electrodes are preferred for this application because of the HD requirement , on the other hand, skin-electrode noise decreases as the contact surface increases because of an averaging effect [40]. This skin-electrode noise is generally the most important source of noise in EMG recordings [40], therefore the size of the electrode contact surface and skin preparation (Section 5.1) should be considered carefully.

The number of electrodes, the electrode pattern and associated filter possibilities influence the number of MU and its anatomical properties that can be detected. For extraction of MU anatomical properties, combination of electrodes in longitudinal and transversal direction with respect to muscle fibres is essential [42][43]. It is a general characteristic of spatial filters based on electrode grids that they are not invariant to rotations [44]. This implies that orientation of the filter with respect to fibre's orientation influences the capacity to distinguish signals generated by close and far sources [44]. Furthermore, the use of a normal double differentiating (NDD) filter (Figure 3.1), also referred to as a two-dimensional Laplace filter, is described as an advantage in literature. In a simulation research [45] 83.8% of the contributing MUs were detected with a NDD filter and 81 (Laplacian) channels lined up in two directions (9x9), in comparison to 41.4% when using bipolar filtering in the same circumstances. The study also

showed the importance of electrode numbers because the NDD bidirectional percentage decreased to 56.3% when using four Laplacian channels (12 electrodes).

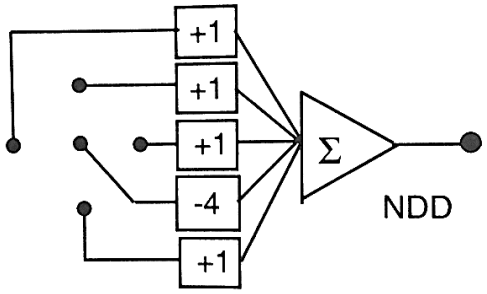

Figure 3.1 – Schematic representation of a NDD filter, one Laplacian channel involving five electrodes. [44]

Literature describes the wide impact of IED on spatial filtering and crosstalk. Decrease of IED limits the detection volume of the electrode system and consequently limit crosstalk [40]. This influence of IED is included in research of Buchtal et al. [46] and Gydikov et al. [47] about amplitude-distance relationship in EMG, where the distance is a measure for detection volume. They found an equation for the effect on detection amplitude (Volt) caused by the distance between motor unit and recording electrodes:

$$V = \frac{V_0}{(r / r_0)^D} \tag{3.1}$$

where r_0 is a reference distance to the electrical centre or innervation zone $(V = V_0)$ of the motor unit, V_0 and D are constants, of which the latter is a function of IED and the detection system [40]. Decreasing IED would imply higher values of D, so the detection amplitude is reduced, resulting in a smaller detection volume. Roeleveld et al. [48][49] also researched the influence of IED on detection volume, using bipolar sEMG recordings while varying IED from 6 to 84 mm. When IED < 40 mm, the relative contribution of superficial and deep motor units to the sEMG signal was not influenced. Decreasing IED (at least up to 6 mm) was found not to be a proper technique for reduction of the electrode view, contrary to the theory that IED can limit the detection volume [40]. However, more recently an optimal IED was found for crosstalk reduction in a sEMG study on the m. tibialis anterior. De Luca et al. [50] obtained bipolar signals with IED ranging from 5 to 40 mm (steps of 5 mm), where 10 mm IED appeared to have the lowest crosstalk contamination. Besides the possible influence on crosstalk, IED acts as a spatial filter. A bipolar sEMG measurement is a simple high-pass spatial filter, eliminating wavelengths longer than half of the IED [44]. Reduction of the IED will shift the cut-off frequency of the filter toward a higher frequency.

Table 3.1 – Summarised requirements for electrode setup in interest of sEMG measurements on the tongue.

Requirement	Specification
Electrode type	AgCl or Ag surface
Number of electrodes	≥ 12
Electrode pattern	Longitudinal and transversal direction with respect to muscle fibres
IED	≤ 10 mm
Fixation on the tongue	Firm
Flexibility (in case of a grid)	Capable of following tongue deformations
Tongue movement	Fully without restriction
Comfort	To a certain extent, not painful
Affordability	Reusable or low cost per electrode/grid

3.3 METHODS AND MATERIALS

3.3.1 CURRENT MATERIALS

Several available and possibly suitable electrodes or grids were selected and all technical requirements were scored good (or yes), intermediate or bad (or no). Together with the practical results from testing on the tongue (Section 3.3.3), the best electrode/grid was selected and prepared for actual sEMG tongue measurements.

3.3.2 GRID DEVELOPMENT

Two prototype electrode grids were developed, the second prototype being the improved version of the first. Since the grids should be flexible enough for following the tongues deformations, implying simultaneous flexibility in multiple direction, two silicone rubbers were selected as grid material. The first silicone was silicone rubber 620/TL95 (N.K.C. Harjon B.V., Dordrecht, The Netherlands) with a shore hardness of 25A. The shore hardness is indicating hardness and flexibility of the material, lower numbers indicate soft and flexible materials. The second silicone was Ecoflex 00-10 (Smooth-On, Macungie, Pennsylvania, USA). This silicone has a shore hardness of 10A and is certified by an independent laboratory to ISO 10993-10, Biological evaluation of medical devices, Part 10: Tests for irritation and skin sensitization [51]. For both prototype grids sintered cylindrical Ag/AgCl electrodes (TMSi, Oldenzaal, The Netherlands) were used, with a diameter of 4.10 mm and a height of 1.13 mm. The first prototype, referred to as Silic-4, contained four of these electrodes in an area of 35.0 by 35.0 mm with 17.5 mm IED. Its mould was designed in 3D Builder (app Microsoft Windows) (Figure 3.2 A). The second prototype, referred to as Silic-12, contained twelve electrodes within a cross-shape. Leaving various filtering techniques and bidirectional measurements to the possibilities. The outer dimensions of Silic-12 were based on my own tongue size. An area of 30.0 by 30.0 mm was available for the 12 electrodes with 4.10

mm diameter, resulting in a maximum IED of 7.0 mm. These dimensions were incorporated in the mould design (Figure 3.2 B), created with the 3D computer aided design (3D-CAD) program SolidWorks (Dassault Systèmes, Waltham, Massachusetts, USA). Both moulds were 3D printed on the University of Twente. The electrode locations were slightly lowered to hold the electrodes in place and prevent moulding of a silicone layer on the measurement surface. Not all electrodes were perfectly round, therefore the circular rims had a chamfer to realize the right position for every electrode. The lowered electrode locations also contained a hole with a smaller diameter (although not visible in Figure 3.2 A), for assistance pressure on the electrodes during removal of the grid from the mould. Furthermore, Silic-12 had two holes for leading away the electrode wiring. Before moulding, the moulds were greased with sunflower oil for reduction of silicone attachment and easier removal of the grid. No industrial spray could be used because of safety reasons for oral use. The electrodes were placed in the greased moulds, with

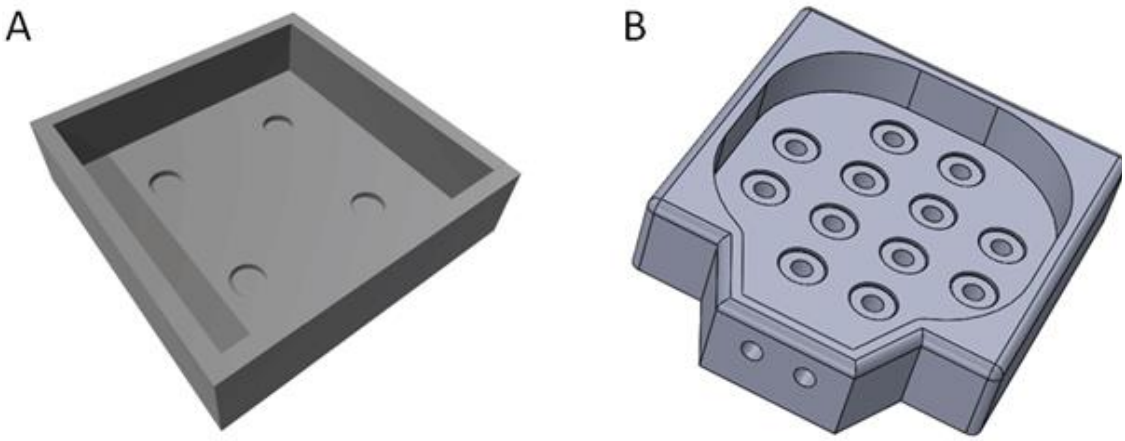

Figure 3.2 – Mould designs for the prototype sEMG grids. (A) For Silic-4, created in 3D Builder. (B) For Silic-12, created in 3D-CAD.

their silver leads bend in a curl and then upwards (Appendix Figure A1 A) with the purpose of strain relief. Then the silicone rubber 620/TL95 (for Silic-4) and Ecoflex 00-10 (for Silic-12) were prepared by mixing the silicone and its harder. These mixtures were carefully poured into the moulds till the electrodes and curled part of their leads were covered (Appendix Figure A1 A). When the curing time passed, individually shielded electrode cables (TMSi, Oldenzaal, The Netherlands) could be soldered to the electrode leads (Appendix Figure A1 B). The leads and open cable parts were positioned in a manner they did not touch leads or open cable parts of other electrodes, to prevent signal disturbance or mixture. A second silicone layer was added on top of it, for shielding and protection of the cabling. After the curing time, the grids could be carefully removed from their moulds.

3.3.3 EXPERIMENTS

All electrodes/grids were tested for their practical use on the tongue. The electrodes/grids were fixated to the tongue with denture prosthetic adhesive strips (Fittydent, Ridam Care BV, Breukelen, The Netherlands). Several tongue movements were executed; protrusion; tongue to the left; tongue to the right; tongue towards the chin and tongue towards the nose. These movements were filmed, and the performances of the electrodes/grids were scored for the practical requirements (good, intermediate or bad).

3.4 RESULTS

3.4.1 CURRENT MATERIALS

The electrodes/grids selected for this research (Figure 3.3) were separate micro electrodes (TMSi, Oldenzaal, The Netherlands), an HD sEMG grid (TMSi, Oldenzaal, The Netherlands), and an electrocorticography (ECoG) grid (Ad-Tech, Racine, Wisconsin, USA). Their scores for the technical requirements are incorporated in Table 3.2.

The micro electrodes (Figure 3.3 A) consist of a sintered Ag/AgCl cylindrical electrode with a 1.5 mm diameter on the measurement surface. Each electrode is protected by a plastic cab and connected to a shielded cable. Moreover, the 10 mm diameter of the plastic cab together with some additional interelectrode distance (IED) causes a maximum use of 6 to 8 electrodes on the tongue.

The HD sEMG grid (Figure 3.3 B) consists originally of 64 AgCl electrodes (8x8), unfortunately this grid is too wide for use on the tongue so two columns were eliminated. The remaining 48 electrodes (8x6) have a 2.0 mm diameter and a 4.0 mm IED. In total, the grid covers an area of 35.0 x 25.0 mm.

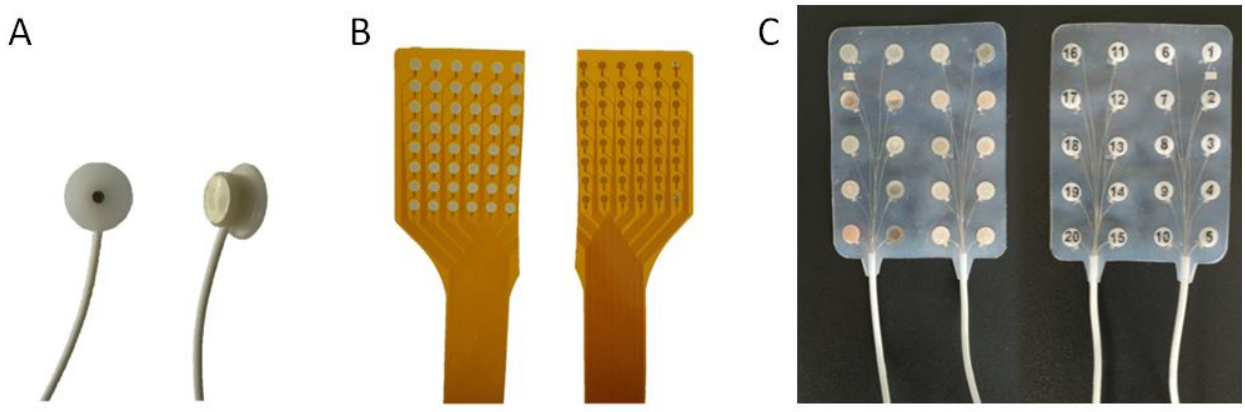

Figure 3.3 – Selected electrodes/grids for technical and practical evaluation for sEMG measurement on the tongue. (A) Separate micro electrodes. (B) Adjusted HD sEMG grid. (C) ECoG grid.

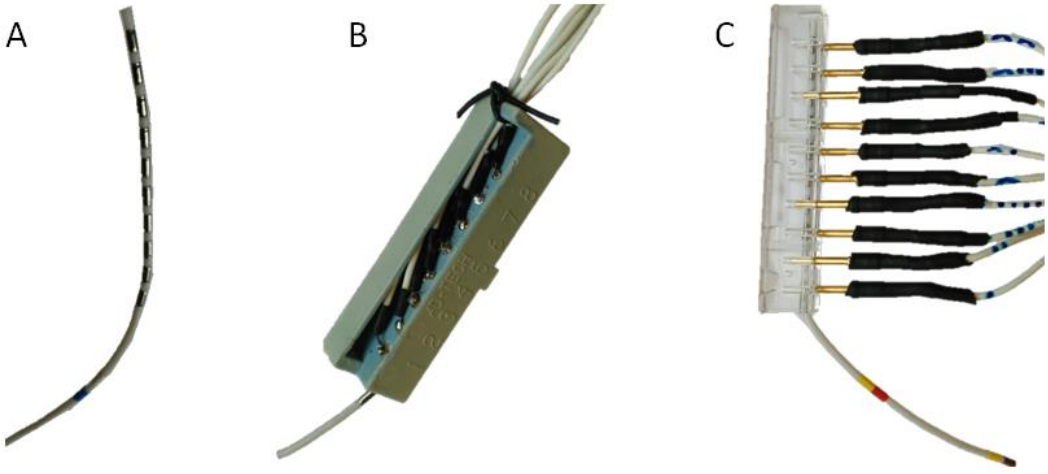

Figure 3.5 – Assembly of two connectors to ECoG grid. (A) One of two ECoG leads, holding 10 connection places. (B) Cabrio connector (Ad-Tech, Racine, Wisconsin, USA) with 8 connections. (B) Pin-hole connector with 10 brass pins (10 connections).

Figure 3.4 – Schematic representation of the ECoG grid with red colored inoperable electrodes. Electrodes 11 and 12 were inoperable because of the Cabrio-connector only holds 8 connections. The cause of inoperability of electrodes 17 and 20 was unknown.

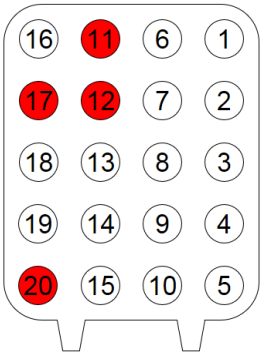

The ECoG grid (Figure 3.3 C) contains 20 platinum disc electrodes with a 10.0 mm IED and a 4.0 mm diameter of which a central 2.3 mm diameter is exposed to the measurement surface. The electrodes are embedded in a soft Silastic sheet [52], manufactured from high quality medical grade silicone and sterilized by gamma irradiation [53]. In addition, the grid is quite expensive, developed for intracranial EEG measurements and probably somewhat over qualified. On the other hand, since one ECoG grid is available and it scored highest (of all current materials) for the practical requirements (Table 3.2), this technique was tested for sEMG tongue measurements (Chapter 5). Therefore, the ECoG grid was prepared for use by assembly of two connectors (Figure 3.5) and measured with a multimeter (Figure 3.4).

3.4.2 GRID DEVELOPMENT

Two prototype grids, Silic-4 (Figure 3.6) and Silic-12 (Figure 3.7), were created. The soldered electrode lead-cable connections appeared to be fragile, some connections needed to be reattached during the production process. One connection (Silic-12, electrode 4) broke during addition of the second silicone layer and therefore could not be repaired. Both prototypes were scored for the technical requirements (Table 3.2) and measured with a multimeter (Figure 3.7 C). All Silic-4 electrodes were operable.

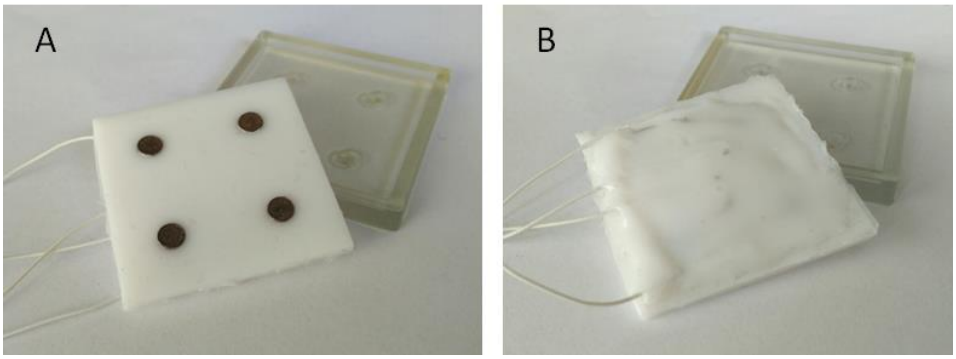

Figure 3.6 – The Silic-4 and its mould. (A) sEMG measurement surface. (B) The top side.

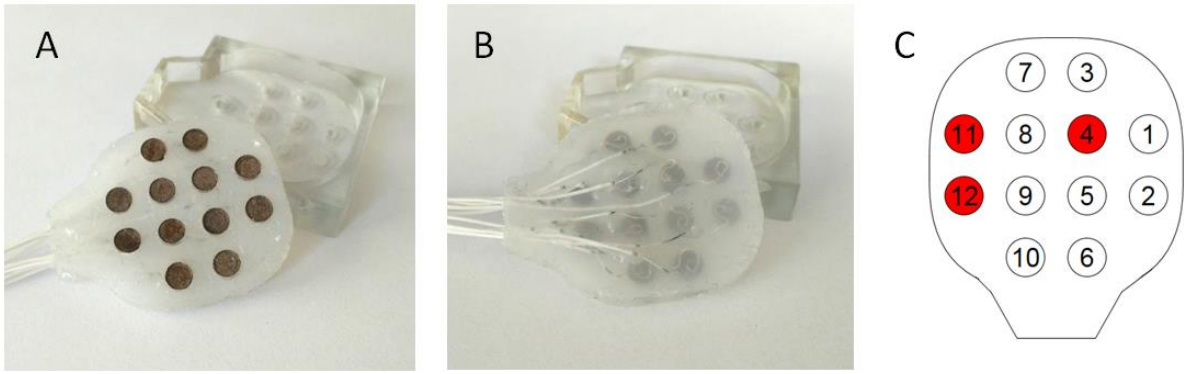

Figure 3.7 - The Silic-12. (A) sEMG measurement surface and the mould. (B) The top side and the mould. (C) Schematic representation (top side) with red colored inoperable electrodes. Electrode 4 was inoperable since the solder was broken. The cause of inoperability of electrodes 11 and 12 is unknown.

3.4.3 EXPERIMENTS

All five electrodes/grids were evaluated and scored (Table 3.2) for the practical requirements: fixation on the tongue, flexibility, tongue movement, comfort, and affordability. Together, fixation on the tongue and flexibility of the grids determined the extend of electrode displacement during tongue movement and deformations. Fixation on the tongue with the denture prosthetic adhesive strips appeared to be insufficient for almost all electrodes/grids. When testing the micro electrodes, the slightest tongue movements caused electrodes to come off (Figure 3.8 A). Conversely, the HD sEMG grid had a reasonable attachment to the tongue surface, but the grid came off easily since its disability to bend in two

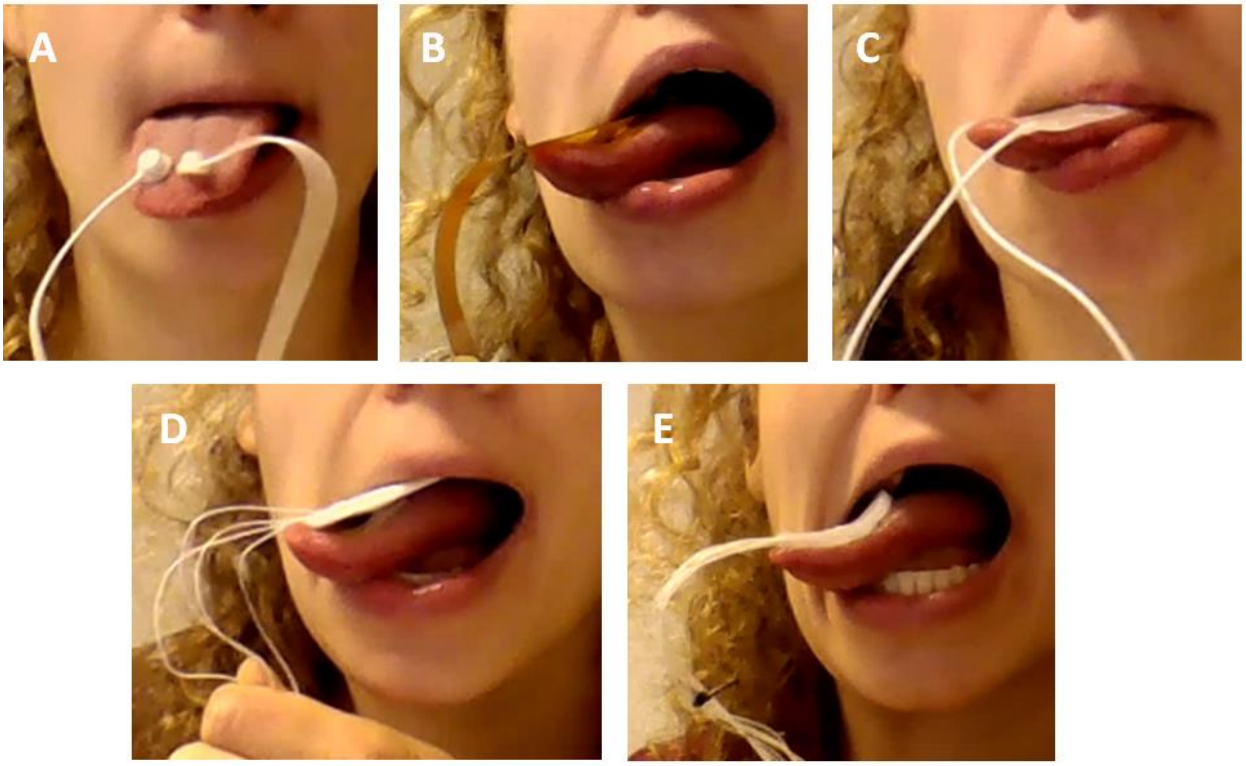

Figure 3.8 – Electrode/grid testing for its practical use on the tongue. A tongue movement to the right is shown. (A) Two micro electrodes, (B) HD sEMG grid, (C) ECoG grid, (D) Silic-4, (E) Silic-12.

directions simultaneously (Figure 3.8 B). The ECoG grid did have the advantage of its flexible silicone which could follow the tongue's deformations, in combination with a reasonable attachment to the tongue (Figure 3.8 C). Though, this specific ECoG grid was slightly large for application on the tongue, causing it to displace or come off occasionally because of contact with other parts of the mouth. The Silic-4 scored bad for both fixation and flexibility, the grid was too rigid to follow any tongue deformation and the adhesive strips did not attach to the silicone (Figure 3.8 D). The same holds for Silic-12, the adhesive strips did not attach to the silicone, however the combination of the grids' weight and it surface properties caused a reasonable fixation itself. Furthermore, the grid revealed its success to follow the tongues curvature (Figure 3.8 E). None of the grids caused discomfort or physical restriction of tongue movement. Although, a behavioural restriction of tongue movement was observed within all tests. The subject showed correcting lip motion and reduced range of tongue motion to contain the electrode/grid position (Figure 3.8 A, C, D). The affordability of the different electrodes/grids was mostly depending on reusability. The ECoG grid, Silic-4 and Silic-12 are made of porous silicone and contain grooves around the electrodes, which hampers the possibility to clean the grids for reuse. In addition, the ECoG procurement is expensive. The micro electrodes and HD sEMG grid are more suitable for hygienic cleaning and lower in procurement costs.

Table 3.2 – Scores per electrode/grid for each technical and practical requirement. The green checkmark indicates yes or good, the orange wave indicates intermediate, and the red cross indicates no or bad.

Requirements	Micro electrodes	HD sEMG grid	ECoG grid	Silic-4	Silic-12
Electrode type	✓	✓	✗	✓	✓
Number of electrodes	✗	✓	✓	✗	~
Electrode pattern	✓	✓	✓	✓	✓
IED	~	✓	✓	✗	✓
Fixation on the tongue	✗	~	~	✗	~
Flexibility (in case of a grid)		✗	✓	✗	✓
Tongue movement	✓	✓	✓	✓	✓
Comfort	✓	✓	✓	✓	✓
Affordability	✓	✓	✗	~	~

3.5 Discussion

Major fundamental and practical research could be done to the technical requirements for tongue grid development, but that was beyond the scope of this study. The technical requirements as stated in Section 3.2 were investigated in literature. For future tongue grid development, these requirements should be improved. The suitable type of electrodes should be researched since epidermal composition differs between skin and tongue. Furthermore, the number of electrodes should be increased, for identification of more MUs as described earlier (Section 3.2). More electrodes will involve smaller IED and electrode surfaces, their influence on sEMG tongue measurements is an important topic for further research.

The ECoG and Silic-12 grid showed highest potential for use on the tongue, since their capability to follow the tongues curvature and reasonable fixation. Though, the Silic-12 is expected to result in better sEMG measurements because of its more stable position on the tongue and more suitable electrode type. This was tested in Chapter 5.

The most crucial point of improvement for all electrodes/grids appeared to be the fixation on the tongue (Table 3.2). Several options can be explored in future research. One option being a vacuum electrode system, which is widely used within electrocardiography applications. For instance, available with four different vacuum levels and use of silicone around electrodes [54]. Application of such a system within micro electrodes or a silicone grid might realize a firm fixation to the tongue, especially since its applicability within a wet environment. On the other hand, the final goal is sEMG tongue measurements on patients with a malignant process on the tongue, which is generally very painful. Application of a vacuum on a malignant process is probably not a comfortable solution. A more comfortable option would be an adhesive grid surface based on the gecko's foot mechanism. The company nanoGriptech [55] developed gecko-inspired adhesives, using knowledge about the microscopic hears on a gecko's foot. Their Setex™ secures medical equipment to the skin, can be film-thin, conform to a wide range of shapes and can be designed with varying grip or friction strengths to fit the application's needs [55]. A Setex™ version suited for a wet environment with a firm grip and smooth method for release would be ideal. Another option is a tongue cover as fixation method. A rigid tongue cover with a rough surface was developed [56] as toothbrush (Figure 3.9 A and B). This tongue cover can potentially hold electrodes, the design suggests multiple positions for small electrodes (Figure 3.9 A). Its fixation is based on the size and shape of this cover, causing the tongue to be slightly squeezed into the cover securing the cover's position. The advantage of this cover is the possibility to fit additional sEMG electrodes to the downside of the tongue.

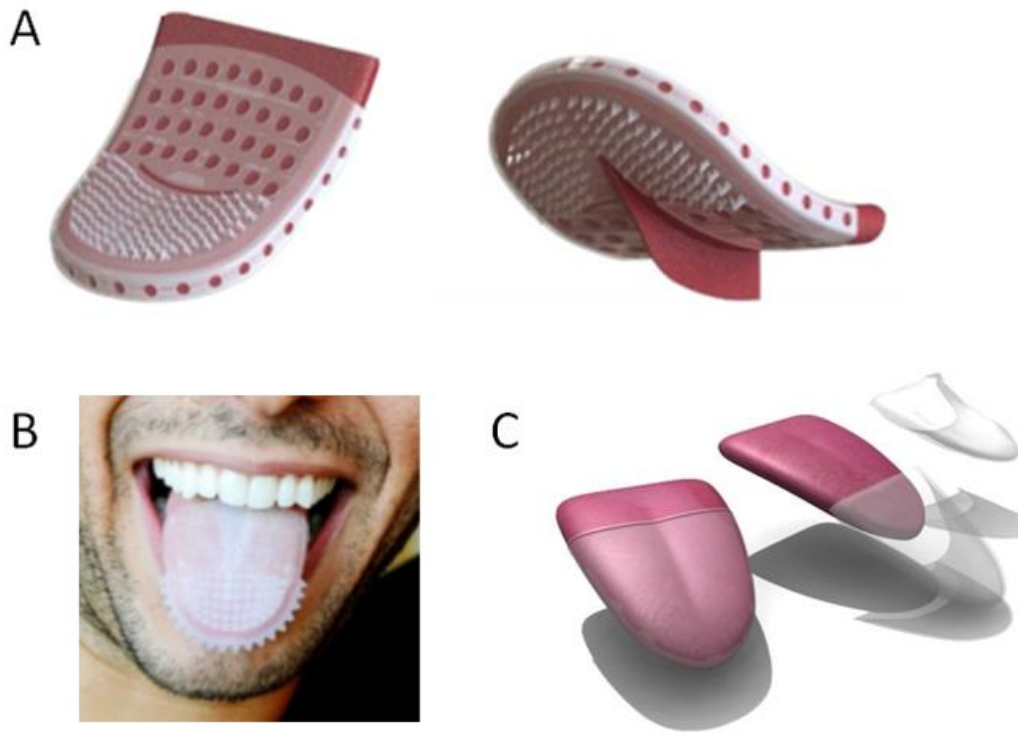

Figure 3.9 – Two tongue covers. (A) and (B) show the tongue cover designed to clean the teeth. [56] (C) Shows a latex tongue cover to protect from the taste of bitter medicine. [57]

The disadvantage is the rigidity of the cover, prohibiting tongue deformations and the tongue can potentially move within the cover causing shift of electrode placement. A flexible cover was developed [57] to protect the tongue from the taste of bitter medicine (Figure 3.9 C). This product probably was not a great success since the posterior part of the tongue is sensitive to bitter taste, this part of the tongue is not covered with this design. However, it might be suitable for holding small electrodes and secure a firm fixation, especially in combination with the earlier mentioned ideas of a vacuum or Setex™ fixation.

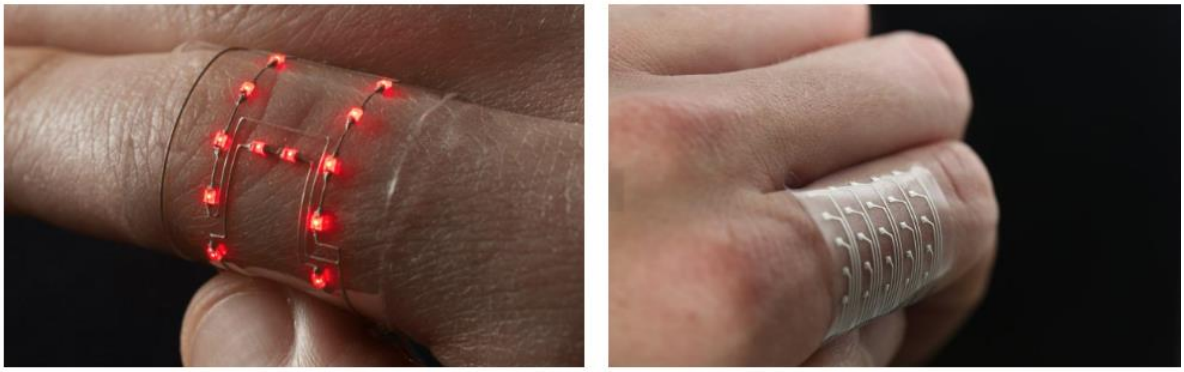

Figure 3.10 – Two hybrid 3D printed electronic devices with flexible and stretchable properties. Credits: Alex Valentine, Lori K. Sanders, and Jennifer Lewis / Wyss Institute at Harvard University. [58]

The practical experiments underlined the importance of flexible grids. The difficult part was, as experienced with the Silic-12, that the electronic components could not stretch and bend like the enveloping silicone. This was making the Silic-12 a fragile ensemble. For future tongue grid development 3D printing of flexible electronics should be explored and applied. Recently, a new hybrid 3D printing technique was developed (Figure 3.10) where soft, electrically conductive inks and rigid electronic components were combined into flexible, stretchable devices that move with the body [58]. This new technique was the first step towards soft electronic devices of nearly every size and shape, besides being lower-cost and mechanically robust [58].

The affordability was mainly based on purchase price and reusability. For hygienic reasons a low-cost grid for single use would be preferred. Moreover, single use grids could allow subject specific size adjustments as done with the HD sEMG grid in this study.

3.6 Conclusion

Two sEMG electrode setups with high potential for tongue measurements were found. Being the existent ECoG grid and the developed prototype Silic-12 grid, the latter is expected to perform best since its more stable position on the tongue and more suitable electrode type. However, improvement in the number of electrodes, the fixation to the tongue and robustness, while maintaining flexibility, is desired.

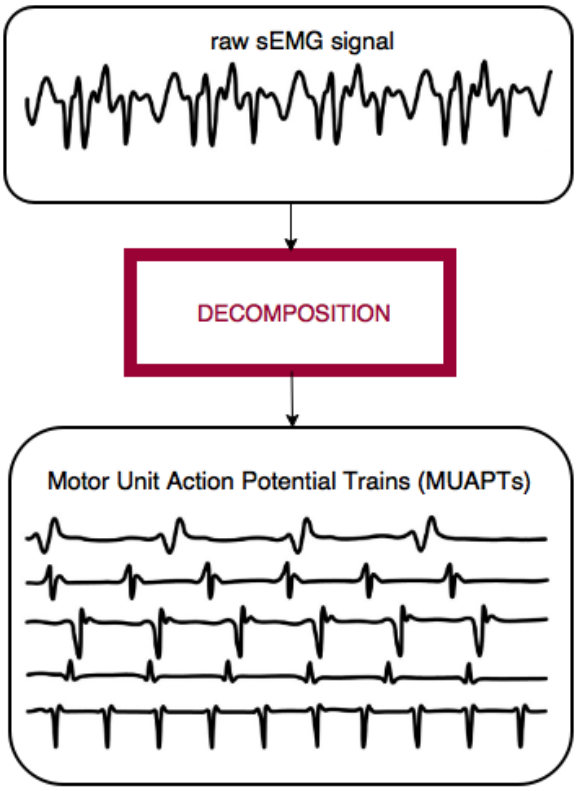
raw sEMG signal
DECOMPOSITION
Motor Unit Action Potential Trains (MUAPTs)

4.1 INTRODUCTION

This chapter addresses the issue of EMG decomposition for MUAPT identification. The identification of MUAPTs is an essential step towards differentiation of muscle activity from various tongue muscles (Figure 1.1). Specifically, the goal of this chapter is to achieve a decomposition algorithm and evaluate its performances. For this purpose, a promising algorithm from the literature is analysed and tested on simulated EMGs.

4.2 DECOMPOSITION TECHNIQUE

Based on the literature review given in Section 2.4, the recently developed hybrid surface EMG decomposition approach (KmCKC) of Ning et al. [1] was selected as the most promising algorithm. Their approach showed superior performance when compared to the classic convolution kernel compensation (CKC) method in terms of decomposition accuracy and robustness against noise. It combines the CKC method and the K-means clustering (KMC) method. The latter is used as an initial step to cluster time instants fired by the same MU followed by the classic CKC, which is modified with a novel iterative process for performance of MUAPT updates. In the next sections, an outline of the algorithm and the model on which it is based is given. The whole procedure is summarised in Figure 4.1 and illustrated in Figure 4.2.

4.2.1 THE MODEL

The foundation of this method is a linear time-invariant multi-input multi-output (MIMO) model for observation of sEMG signals, originating from a number of activated MUs [39][59][60]:

$$\mathbf{x}(n) = \mathbf{H}\mathbf{s}(n) + \mathbf{e}(n) \tag{4.1}$$

where $\mathbf{x}(n) = [x_1(n), \ldots, x_M(n)]^T$ contains M observations, in this case the M sEMG channels, with $x_i(n)$ being the n-th time sample of the i-th channel. $\mathbf{s}(n)$ represents the N sources, in this case MUs, in an extended form from time sample n till $n-P+1$. The MUAPTs, i.e. the activities of the MUs, are represented by a vector: $[s_1(n), \ldots, s_N(n)]^T$. Its extended version is the vector $\mathbf{s}(n)$, containing the most recent history of P time samples:

$$\mathbf{s}(n) = \left[s_1(n),\ s_1(n-1),\ \ldots,\ s_1(n-P+1),\ \ldots,\ s_N(n),\ s_N(n-1),\ \ldots,\ s_N(n-P+1)\right]^T \tag{4.2}$$

where P is the length of the finite impulse response. This vector forms a convolution with $\mathbf{H}$, a mixing matrix containing all channel responses of length P time samples. $h_{ij} = [h_{ij}(0), \ldots, h_{ij}(P-1)]$ is the response to the j-th source in the i-th channel. Finally, a zero-mean white noise, $\mathbf{e}(n)$, is added to each channel.

4.2.2 THE ALGORITHM

The goal in sEMG decomposition is to reconstruct $\mathbf{s}(n)$, while given only measurement vector $\mathbf{x}(n)$. For this purpose, the vector $\mathbf{x}(n)$ should be extended to a convolutive MIMO form by addition of K-1 delayed repetitions per channel (Figure 4.1 and 4.2, step 1) [60]:

$$\bar{\mathbf{x}}(n) \overset{def}{=} \left[x_1(n),\ x_1(n\text{-}1),\ \ldots,\ x_1(n\text{-}K\text{+}1),\ \ldots,\ x_M(n),\ x_M(n\text{-}1),\ \ldots,\ x_M(n\text{-}K\text{+}1) \right]^T \quad (4.3)$$

The same holds for the vector $\mathbf{s}(n)$ and the matrix $\mathbf{H}$ of size $KM \times N(P+K\text{-}1)$ [60]:

$$\bar{\mathbf{s}}(n) \overset{def}{=} \left[s_1(n),\ s_1(n\text{-}1),\ \ldots,\ s_1(n\text{-}K\text{-}P\text{+}1),\ \ldots,\ s_N(n),\ s_N(n\text{-}1),\ \ldots,\ s_N(n\text{-}K\text{-}P\text{+}1) \right]^T \quad (4.4)$$

$$\bar{\mathbf{H}} \overset{def}{=} \begin{pmatrix} \mathbf{H}_{11} & \cdots & \mathbf{H}_{1N} \\ \vdots & \ddots & \vdots \\ \mathbf{H}_{M1} & \cdots & \mathbf{H}_{MN} \end{pmatrix} \text{ with } \mathbf{H}_{ij} \overset{def}{=} \begin{pmatrix} h_{ij}(0) & \cdots & h_{ij}(P\text{-}1) & \cdots & 0 \\ \vdots & \ddots & \ddots & \ddots & \vdots \\ 0 & \cdots & h_{ij}(0) & \cdots & h_{ij}(P\text{-}1) \end{pmatrix} \quad (4.5)$$

The MIMO model becomes:

$$\bar{\mathbf{x}}(n) \ = \ \bar{\mathbf{H}}\bar{\mathbf{s}}(n) \ + \ \bar{\mathbf{e}}(n) \quad (4.6)$$

By calculating the Mahalanobis distance of $\bar{\mathbf{x}}(n)$ a so-called activity index is obtained (Figure 4.1 and 4.2, step 2) [39][60]:

$$\gamma(n) \ = \ \bar{\mathbf{x}}^T(n)\hat{\mathbf{C}}_x^{-1}\bar{\mathbf{x}}(n) \quad (4.7)$$

$\hat{\mathbf{C}}_x^{-1}$ is the estimated covariance matrix of $\bar{\mathbf{x}}(n)$ calculated over the entire record length. For an illustration, see Figure 4.2, step 1. The Mahalanobis distance is the squared length (L2 norm) of $\bar{\mathbf{x}}(n)$ after decorrelation. An analysis of equation (4.7), in which this decorrelation is applied (Appendix A2), shows that $\gamma(n)$ is proportional to the total number of sEMG excitations in an interval of K-1 samples preceding n.

The purpose of the step that follows is to find an index n_1 with which the identification procedure starts. Ning et al. [1] did not motivate their method of n_1 selection. A guess about their motivation is discussed in Section 4.5.1. The selection of n_1 is accomplished as follows. From the sequence $\gamma(n)$, an index n_0 is selected containing the median activity: $\gamma(n_0) = median\ (\gamma(n))$ (Figure 4.1 and 4.2, step 3). Since $\gamma(n_0)$ is the median activity, the assumption is that the interval just before n_0 is statistical representative for some level of activity originating from only a few active MUs. With n_0 the co-activity function $\rho(n_0, n)$ is constructed (Figure 4.1 and 4.2, step 3):

$$\rho(n_0, n) \;=\; \bar{\mathbf{x}}^T(n_0)\hat{\mathbf{C}}_x^{-1}\bar{\mathbf{x}}(n) \tag{4.8}$$

This function is proportional value to the number of sEMG excitations that the records $\bar{\mathbf{x}}(\mathrm{n}_0)$ and $\bar{\mathbf{x}}(n)$ share at the same points in time within the interval of K time samples; see Appendix A2. Then the index n_1 is selected for which the co-activity is maximum: $\rho(n_0, n_1) = \max \rho(n_0, n)$. Thus, n_1 is the index for which a maximum number of sEMG excitations are observed in the M channels that are similar to sEMG excitations that occur at n_0.

Once a suitable index n_1 is found, a sequence of indices is selected which shows high co-activity with n_1. Within $\rho(n_1, n)$, the k highest peaks are selected, denoted by $\varphi_{nc} = [n_{c1},\ n_{c2},\ \ldots,\ n_{ck}]$. The vectors $\bar{\mathbf{x}}(n_{ci})$ with $n_{ci} \in \varphi_{nc}$ contain sEMG excitations associated with a limited number of MUs since similar sEMG excitation patterns are present on these time instances, while taking all electrodes into account. Then, these sEMG excitation patterns are clustered in $nClus$ number of groups based on their shapes through K-means clustering (KMC). The group containing the largest number of elements is selected, denoted by $\varphi_{nv} = [n_{v1},\ n_{v2},\ \ldots,\ n_{vn}]$ (Figure 4.1 and 4.2, step 4). Most of these time instants should be fired by one MU. A first average sEMG excitation shape is obtained for the j-th source:

$$\mathbf{c}_{j0} \;=\; \frac{1}{card(\varphi_{nv})}\sum \bar{\mathbf{x}}(\varphi_{nv}) \tag{4.9}$$

And the MUAPT of the j-th source can be estimated:

$$\hat{\bar{\mathbf{s}}}_{j0}(n) \;=\; \mathbf{c}_{j0}{}^T\hat{\mathbf{C}}_x^{-1}\bar{\mathbf{x}}(n) \tag{4.10}$$

representing, like (4.8), a proportional value to the number of sEMG excitations that $\mathbf{c}_{j0}$ and $\bar{\mathbf{x}}(n)$ share at the same points in time (Figure 4.1 and 4.2, step 5). This acts as a matched filter. The template of this filter is improved h times. Starting with finding the r highest peaks in $\hat{\bar{\mathbf{s}}}_{j*}(n)$, the asterisk indicates the last version of $\hat{\bar{\mathbf{s}}}_{\mathbf{j}}(n)$ and is an increasing number till h. Their time of occurrence, denoted by $\varphi_{n*} = [n_{*1},\ n_{*2},\ \ldots,\ n_{*r}]$, is used for calculation of a new average sEMG excitation shape $\mathbf{c}_{j*}$ via (4.9). An improved MUAPT of the j-th source $\hat{\bar{\mathbf{s}}}_{j*}(n)$ is found with (4.10). In the next cycle, more reliable events are expected. So, r is incremented with a constant Np. This cycle continues till $\hat{\bar{\mathbf{s}}}_{jh}(n)$ is reached (Figure 4.1 and 4.2, step 6). Then, $\gamma(d)$ is set to zero with $d \in \varphi_{nv}$ (Figure 4.1 and 4.2, step 7). This entire process is repeated nMU (the maximum number of MUs that can be extracted) times, starting from the determination of n_0. Resulting in nMU estimated MUAPTs, with their corresponding sEMG excitation shapes per electrode in $\mathbf{c}_{j*}$.

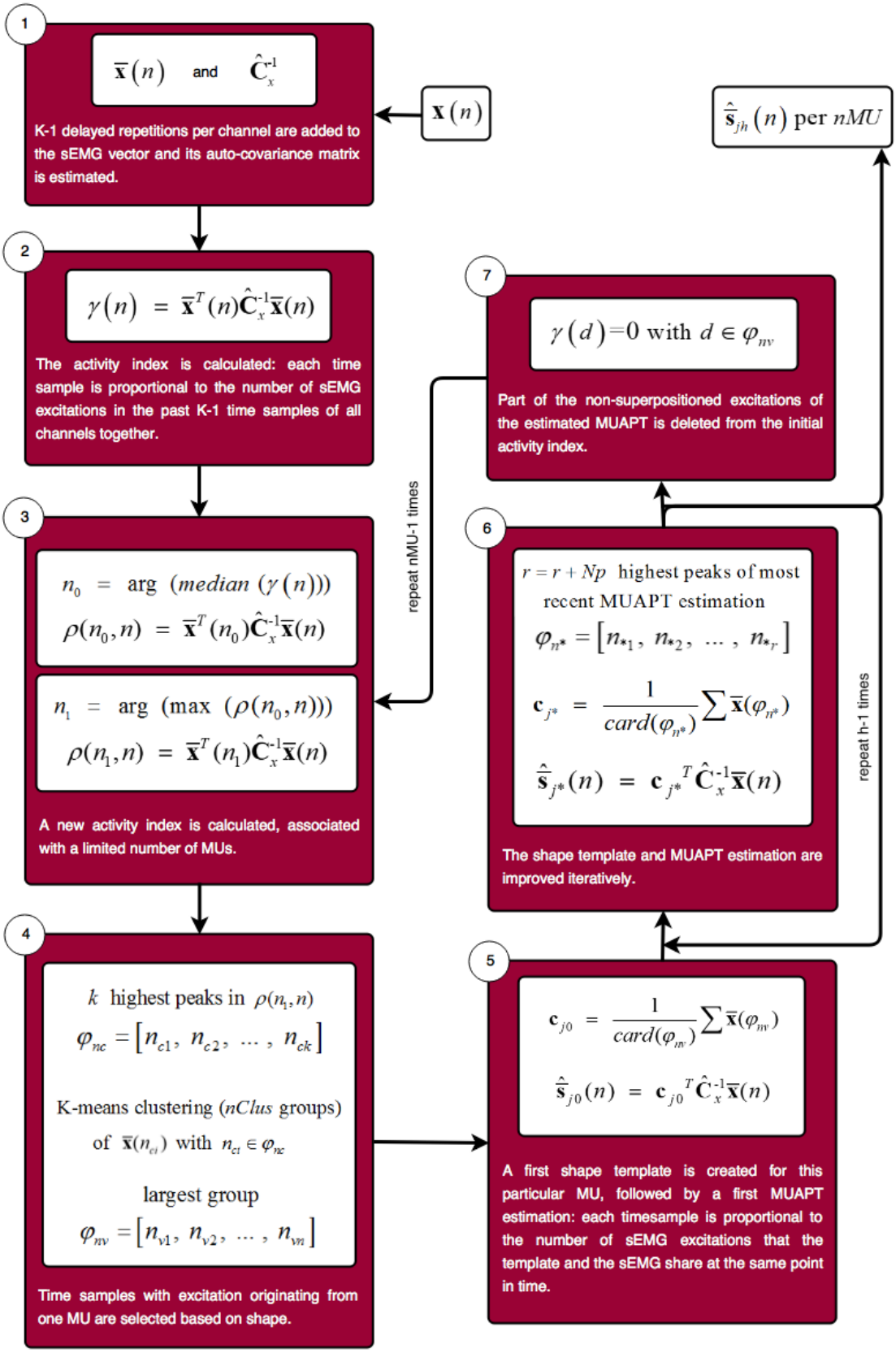

Figure 4.1 – Flowchart containing the KmCKC decomposition algorithm.

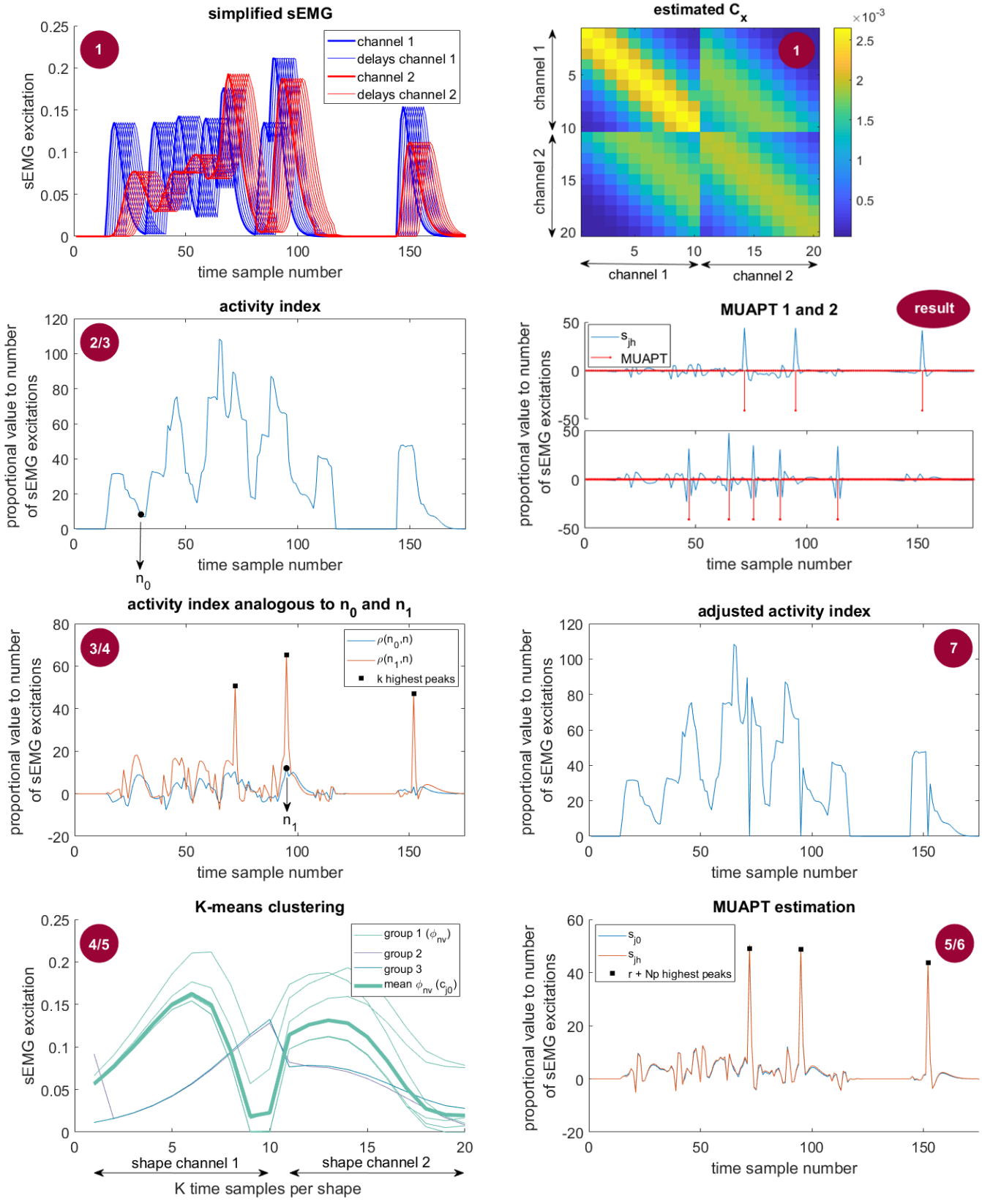

Figure 4.2 – Illustration per step (indicated by number in red circles) as described in Figure 4.1. The simulated (simple) sEMG originated from two MUs and held two channels. The length of the simplified sEMG was 500 time samples, for the purpose of clear illustrations only the first 175 time samples are shown. The parameter values were set to: K = 10, k = 12, nClus = 3, r = 4, h = 1, nMU = 2.

4.3 METHODS AND MATERIALS

4.3.1 ALGORITHM IMPLEMENTATION

The KmCKC method (Section 4.2) was implemented in MATLAB (version 2017a, MathWorks, Massachusetts, USA) (Appendix A3). A simplified representation of simulated sEMG measurements and its associated MUAPTs were used for debugging, code development, and for a first simple test, i.e. a sanity check. These sEMG measurements were simulated (Appendix A4) by convoluting random pulse trains with a mixing matrix containing a variety of density functions (of χ^2 distributions) as impulse responses. These functions are chosen as they have a smooth onset and decay, like sEMG.

4.3.2 EMG SIMULATIONS

It was essential to test the performance of the KmCKC algorithm with realistic EMG measurements with known original sources (MUAPTs). For these reasons the simulator [61] of EMGlab [62] was selected. This simulator provided access to the original MUAPTs of the simulated EMGs, yet the related impulse responses were not available. Six different EMGs were simulated, varying in electrode configuration (number, position and interelectrode distance (IED)) and activated MU numbers (Table 4.1). The number of activated MUs could be set, however there was no control over the number of MUs sensed by the electrodes. For simulation of these EMGs the major part of settings was default, simulating the m. biceps brachii. The simulator settings are included in the appendix (Appendix Figure A5-A7). Needle electrode configurations and the neuropathic MU loss fraction are adjusted per EMG. The latter was used for simulation of the numbers of activated MUs (higher MU loss fraction incorporated lower number of activated MUs). The simulator produced EMG signals with a 15 kHz sample frequency. This was resampled to the more standard 2048 Hz.

Table 4.1 – Six simulated EMGs and their configurations. The electrode configuration contains electrodes (dots with number) and the muscle fibre direction (dashed line).

	Activated MUs	Electrode configuration	IED
EMG 1	2	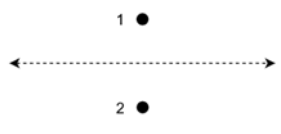	7 mm
EMG 2	8		
EMG 3	8	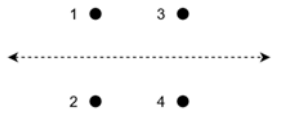	7 mm
EMG 4	32		
EMG 5	8	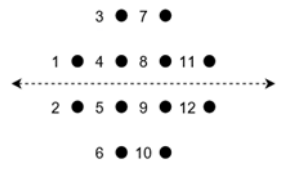	4 mm
EMG 6	32		

Table 4.2 – All parameters included in the random parameter optimization.

Parameter	Definition	Range (step size)	Based on
K	Number of delays created	1-20 (1)	Holobar et al. [39]
k	Number of highest peaks within $\rho(n_1, n)$ as input for KMC	10-300 (10)	Experience with simplified sEMG
nClus	Number of clusters within KMC	2-5 (1)	Ning et al. [1]
r	Number of highest peaks within $\hat{\mathbf{s}}_{j*}(n)$, updated every iteration of h with Np	5-20 (1)	Ning et al. [1]
h	Number of iterations for improvement of $\mathbf{c}_{j0}$	1-40 (1)	Ning et al. [1]
fc	Cut-off frequency for estimated MUAPTs filtering	5-50 (5)	Experience with simplified sEMG
frac	Fraction for MUAP definition threshold	0.25-0.75 (0.01)	Experience with simplified sEMG

4.3.3 PARAMETER OPTIMIZATION

Besides the different EMG simulation settings, the influence of parameters within the KmCKC algorithm and the subsequent signal processing was researched. Therefore, a random search for parameter optimization was added. All KmCKC parameters and two important processing parameters were considered (Table 4.2). Np, being the step size of r during the iterations for improvement of $\mathbf{c}_{j0}$, was set equal to the initial size of r [1] and therefore not included as a separate parameter. Furthermore, nMU was set to the number of activated MUs within the simulated EMG. The random search for parameter optimization was performed by application of 10,000 different parameter value combinations per EMG. The two best performing combinations were selected. The first selection criterion included the highest number of identified MUAPTs. An identified MUAPT was defined as a MUAPT with a correct percentage (Section 4.3.4) above 88%. The second selection criterion yielded the ratio of the mean correct percentage and mean overshoot percentage (Section 4.3.4) regarding the identified MUAPT(s). Both percentages were considered equally important. The parameter values of the two best performing combinations served as new parameter range for the second round of 10,000 random parameter combinations, furthermore the step size of all parameters (except $frac$) were set to one. Again, the two best performing combinations were of interest.

4.3.4 PERFORMANCE MEASURES

All simulated EMGs were used as input for the KmCKC algorithm, and for each EMG the parameters of the algorithm were optimised with the random search strategy. The resulting estimated MUAPTs were filtered (high-pass) with cut-off frequency fc. Then, each original MUAPT was matched to the most similar estimated MUAPT (Appendix A8). Two relevant performance measures were calculated per MUAPT; the percentage correct estimated action potentials (in relation to the original number of action potentials), and the percentage overshoot, being the number of incorrect estimated action potentials in

relation to the original number of action potentials (Appendix A9). These are referred to as correct percentage and overshoot percentage, respectively. For these performance measures a threshold for MUAP definition within the estimated MUAPTs was needed. This threshold was defined as a fraction $frac$ of the maximum value within the estimated MUAPT.

4.4 RESULTS

4.4.1 ALGORITHM IMPLEMENTATION

The first results involved the decomposition of the simplified representation of sEMG (Figure 4.3). The algorithm showed high correct and low overshoot percentages when decomposing the simplified representation of sEMG. Even low amplitude MUAP shapes which were hard to differentiate in the sEMG, like shape 2 in Figure 4.3, were decomposed.

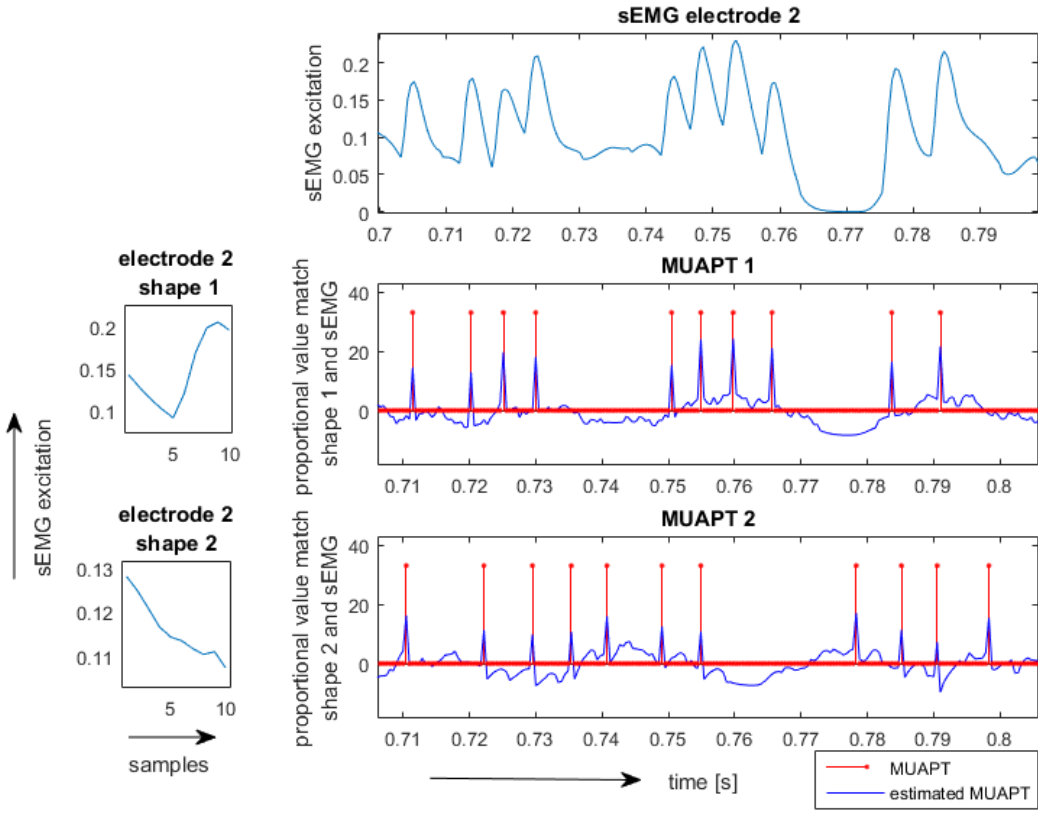

Figure 4.3 – Decomposition results from the simplified representation of sEMG. This sEMG included two electrodes (only the results for electrode 2 are shown) and two sources (MUAPTs). On the left the two MUAP shapes (impulse responses) within electrode 2 are depicted. The parameter values were set to: K = 10, k = 30, nClus = 4, r = 10, h = 5, fc = 15 Hz, frac = 3/8. Resulting in the correct-overshoot percentages 99.1%-0% and 97.3%-1.8%, for MUAPT 1 and MUAPT 2, respectively.

Table 4.3 – Six simulated EMGs and their number of sensed MUs and firing rates.

	Number of activated MUs	Total number of sensed MUs	Number of sensed MUs (per electrode row)	Mean number of firings per activated MU in first second (std)
EMG 1	2	1	1 (2)	35.5 (0.7)
EMG 2	8	4	1 (1) 3 (2)	35.4 (0.7)
EMG 3	8	7	4 (1,3) 3 (2,4)	34.9 (0.8)
EMG 4	32	14	4 (1,3) 9 (2,4) 1 (3)	34.7 (0.8)
EMG 5	8	4	3 (1,4,8,11) 4 (2,5,9,12)	35.1 (1.1)
EMG 6	32	20	13 (1,4,8,11) 10 (2,5,9,12)	33.8 (2.0)

4.4.2 Simulated EMGs

The EMGs from the EMGlab simulator appeared to detect not all the activated MUs (Table 4.3), being a realistic situation. The log of the simulator defined per electrode MUs that did not contribute significant firings. According to this, electrode 3, 6, 7, and 10 of EMG 6 should not have contained any firings. Nevertheless, an EMG was observed in these electrodes, although with lower amplitudes. Each electrode within one row sensed the same MUs, except for electrode 3 of EMG 4. Only six MUs were sensed by multiple electrode rows, three within EMG 5 and EMG 6 (Table 4.3). Also, the mean firing rates of all activated MUs over the first second are included in Table 4.3.

4.4.3 Parameter optimization

The first random search for parameter optimization (Appendix Table A10 and Figure A11) delivered the new parameter ranges for the second random search for parameter optimization. The second random search for parameter optimization (Table 4.4) did not result in significant different results. Except, EMG 3 showed major improvement, since two extra MUAPTs were identified. Unfortunately, EMG 3, 4, and 6 showed very high overshoot percentages, outranging the number of excitations in the original MUAPT (> 100%). In total, three times a MUAPT was identified which did not contribute significant firings according to the log of the EMG simulator. For example, in EMG 1 two MUAPTs were identified (Table 4.4) were one MU contributed significant firings (Table 4.3). The MUs which were sensed by more than one electrode row were not necessarily identified more often, EMG 5 and 6 contained 3 MUs sensed by two electrode rows (Table 4.3) of which 2 MUs were identified in EMG 5 and none were identified in EMG 6. The

Table 4.4 – Results of the second random search for parameter optimization. Where mean correct and mean overshoot are the averaged values within the identified MUAPTs. In some cases several parameter combinations were found for one particular outcome, then the parameter value ranges were noted. In this way, EMG 1-first contains 11 parameter combinations, EMG 1-second 55, EMG 2-first 62, EMG 2-first 449, EMG 5-first 8, EMG 5-second 2 and EMG 6-second holds 6 parameter combinations. EMG 2 showed two equal ratios for mean correct and mean overshoot percentages, so both were classified as first.

Best	Number of identified MUAPTs	Mean correct [%]	Mean overshoot [%]	K	k	nClus	r	h	fc	frac
					EMG 1					
First	2	97.2	5.8	8	176-194	2-5	7	2	32-40	0.52-0.58
Second	2	97.2	7.3	8	176-195	2-5	7-9	2	30-40	0.29-0.47
					EMG 2					
First	2	97.2	4.3	10	213-220	2	5-6	2-3	17-40	0.48-0.56
First	2	95.8	2.9	10	213-220	2	5-6	3-4	15-40	0.48-0.56
					EMG 3					
First	5	92.0	160.3	20	165	3	15	4	19	0.30
Second	5	92.0	167.5	20	165	3	15	4	38	0.29
					EMG 4					
First	2	88.4	237.8	15	102	5	7	18	32	0.29
Second	2	88.4	267.3	15	101	5	7	18	33	0.26
					EMG 5					
First	4	92.1	7.1	3	10	4	6	1	17-35	0.39-0.44
Second	4	89.9	9.6	3	10	4	7	1	36-38	0.42-0.43
					EMG 6					
First	2	90.0	268.3	14	74	3	11	10	19	0.26
Second	2	90.0	271.5	14	74-75	3	11	10	10-17	0.26

decomposition of EMG 5 (Figure 4.4) resulted in four identified MUs were four MUs (Table 4.3) were sensed. Remarkably, the MU of MUAPT 3 was sensed by the electrodes but not identified, while the MU of MUAPT 8 was not sensed but identified. This, again, questions the definition of significant firings within the log files of the simulator.

4.5 Discussion

The goal of this chapter was to verify the behavior of the decomposition algorithm that, according to the literature review, was most promising. First a sanity check was applied using a simple test environment. With a correct rate and an overshoot rate of around 98% and 1%, the algorithm performed very well. In a more realistic setting, with much more MUs and electrodes, the performance went down, but was often still reasonably good.

4.5.1 DECOMPOSITION ALGORITHM

The decomposition algorithm as applied in this thesis holds the calculation of $\rho(n_0,n)$ and $\rho(n_1,n)$, after selection of the median value of $\gamma(n)$, its index being n_0. The necessity of these steps was not fully understood. In the articles of Holobar et al. [39][59], these steps (with different n_0 selection) were part of a technique to separate superimposed sources. If multiple sources were active at n_0, the group of active sources was referred to as G_{no}. It was stated that when looking for the highest values inside $\rho(n_0,n)$, a rather high probability of finding a sample index n_1 corresponding to the firing moment of another group of sources G_{n1} would occur. The nature of innervation pulse trains makes it highly unlikely that $G_{no}=G_{n1}$. To sort out the fewer sources that fire at both n_0 and n_1, the simultaneous pulses in $\rho(n_0,n)$ and $\rho(n_1,n)$ should be selected. This was done by finding the peaks in the product $\rho(n_0,n)\cdot\rho(n_1,n)$. Repetition of this process could separate superimposed sources at n_0. Since the product $\rho(n_0,n)\cdot\rho(n_1,n)$ was not part of the algorithm applied here, the use of $\rho(n_1,n)$ seems unnecessary. The selection of n_0 via the median of $\gamma(n)$ was probably a manner to select a sample index with few or one active sources. The application of KMC was expected to reduce this to one active source, its superimposed MUAPs could be separated via CKC.

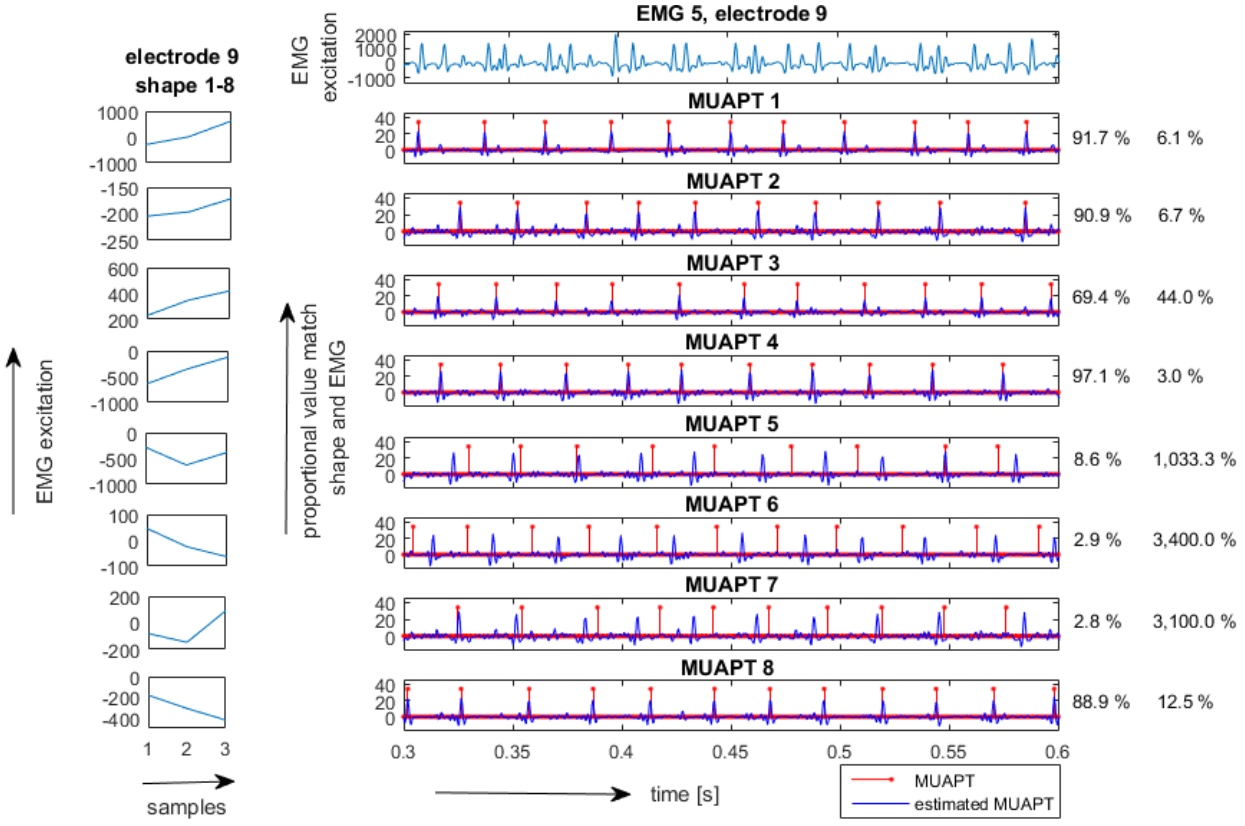

Figure 4.4 - Decomposition result of EMG 5. The parameter values were: K = 3, k = 10, nClus = 4, r = 6, h = 1, fc = 17 Hz, frac = 0.41. The shapes per MUAPT consist of three samples since K = 3, causing the shapes being just an indication for EMG excitation amplitude. On the right, the correct and overshoot percentages per MUAPT are included.

4.5.2 SIMULATED EMGS

Six different EMG simulations were applied for basic insight in the influence of electrode and MU numbers on the number of decomposed MUAPTs. The number of electrodes showed limited influence (Table 4.4). However, because of the low number of simulations, no statistically significant conclusions could be drawn. Farina et al. [45] executed a more extensive research on this subject. Surface EMG simulations with a sample rate of 4096 Hz and 200 active MUs were present. Situations with 2x1 electrodes (in transverse direction), 2x2 electrodes, and 3x3 electrodes resulted in percentages of 10.5, 11.5 and 17.4 detected MUs (upper limit), respectively. Detection of most of the MU population was observed when 9x9 Laplacian channels were uses. These small percentage differences (for 2x1, 2x2, and 3x3 electrodes), in combination with the lower number of activated MUs in this thesis, explains why the influence of electrode numbers was limited. This is unlike the number of activated MUs, which was of great influence on the number of decomposed MUAPTs. EMGs 3 and 5 showed higher numbers of decomposed MUAPTs in comparison with EMGs 4 and 6, which hold more activated MUs. A straightforward explanation, also stated by Holobar et al. [60], is the activity of several MUs at each arbitrary time moment, i.e. numerous superposition. However, Holobar et al. [60] found their simulation results not depending on the number of active MUs. The provided explanation was that sources with the highest amplitudes were privileged during the reconstruction process. Since another reconstruction process was used in this thesis and the results suggest otherwise, the first explanation is considered more likely.

The simulated EMGs require a critical note. The EMGs were obtained with simulated needle electrodes within a muscle. Needle electrodes obtain detailed and narrow MUAP shapes in comparison to surface electrodes, which obtain more similar and broad shaped MUAPs causing more superposition. The EMG simulations as used here could have caused different results than sEMG simulations would have. Application of the simulator created by Farina and Merletti [63] would be preferred in future research. Another option was to place the needle electrodes at greater distance from the simulated muscle. However, the simulator was not developed for this purpose and did not simulate any EMG excitation. The latter was also the reason for the smaller IED in EMG 5 and 6, otherwise electrode 3, 6, 7, and 10 would not have recorded any EMG excitations.

4.5.3 PARAMETER OPTIMIZATION

Through two random searches for parameter optimizations per EMG, several parameter influences could be observed. Parameter K, with a value of 10 or lower, seemed to relate to lower overshoot percentages (Table 4.4). K defines the length of the template within the matched filter. When this template is chosen too long there is a higher chance of finding coincidently (false positive) matching EMG excitation parts. Its influence on the final estimated MUAPT is limited if r and h are set low enough (discussed later) (Appendix Table A10, see second best of EMG 4). The lower K values did not always end up within the two second best of the first random search, while showing the potential for good results. See, for example,

EMG 6 at $K = 7$ (Appendix Figure A11). The influence of parameter k, the number of highest co-activity peaks, is undefined. It showed a wide range within all the results (Table 4.4 and Appendix Figure A11). Theoretically it could be thought that a lower k would increase the chance to include just one MU in φ_{nv} after KMC. For $nClus$, the number of presumed clusters, holds the opposite, a higher $nClus$ could increase the chance to include just one MU. However, also $nClus$' influence seems undefined. Contrary to that, the parameters r and h seem to have a strong relation to the overshoot percentages. The final excitation shape $\mathbf{c}_{jh}$ is the mean of $r(h + 1)$ shapes. The number $r(h + 1)$ should not exceed the number of firings of the (to be) estimated MUAPT, since shapes not belonging to this MUAPT will get involved, which causes overshoot. Preferably, $r(h + 1)$ should be equal to the number of firings of the MUAPT or less. All results did confirm this theory, around 35 firings (Table 4.3) were present in each MUAPT and $r(h + 1)$ around 35 and lower contained less overshoot in comparison to higher $r(h + 1)$ (Table 4.4). Therefore, in future application of this algorithm, it would be beneficial to have an expected minimal MU firing frequency. This frequency number can then be used as upper limit for $r(h + 1)$, in the specific case of one second EMG length. The parameter fc did not influence the results. The other processing parameter $frac$ seemed to influence the results. However, the height of $frac$ was some sort of representation of how well the MUAPTs were estimated. If the estimation was good, like EMG 1, 2, and 5 (Table 4.4), the fraction of the highest peak could be high since all correct peaks were fairly high. If the estimation was less, like EMG 3, 4, and 6 (Table 4.4). The fraction had to be lowered otherwise not enough correct peaks were high enough, involving more overshoot.

The parameter optimization of the decomposition algorithm was done by random search. Another option would have been a genetic algorithm (GA) [64] which uses a highly abstract version of evolutionary processes to evolve solutions to given problems. A GA operates on a population of artificial chromosomes (combinations of parameter values K, k, $nClus$, r, h, fc, $frac$), each representing a solution with an associated fitness (correct and overshoot percentage). The algorithm starts with a randomly generated population of chromosomes and carries out a process of fitness-based selection and recombination to produce a successor population, the next generation. This process is iterated, causing the average fitness of the chromosomes to increase until some stopping criterion is reached. This GA technique would have been an efficient alternative for the random search. However, it depends on the situation which of the two is more effective [65].

With the random search method seven parameters were optimized. However, two extra parameters are of interest, the EMG length and nMU. The EMG length was set to one second for all simulated EMGs. For the more complex EMGs, containing more sensed MUs, a longer EMG length could have been beneficial. It would increase the chance of finding time samples corresponding to excitation of one MU. In future research the EMG length should be incorporated in the parameter optimization. The nMU parameter is of interest in case of a higher value than the sensed number of motor units, although nMU was not

incorporated in the parameter optimization (was set equal to the number of activated MUs in the simulation), not all activated MUs were sensed by the electrodes involving a higher nMU value than sensed MUs. It appeared that the decomposition algorithm will continue to derive MUAPTs. Even similar MUAPTs will be generated like MUAPT 2 and 7 in Figure 4.4. However, it is more likely that the algorithm merges two MUs into one than that it splits one train into two. Therefore overestimation of the number of MUAPTs is preferred to underestimation [66]. Though, in experimental EMG this would be an arbitrary choice. In future research, addition of a motor unit number estimation (MUNE) [67] would be beneficial for decomposition with the KmCKC algorithm.

For selection of identified MUAPTs the quite arbitrary criterion of 88% correct estimated MUAPs was applied, however Holobar et al. [60] chose within the same range, 90% was their criterion.

4.6 Conclusion

The KmCKC decomposition algorithm was implemented and tested on simulated EMGs. The algorithm showed great potential for MUAPT identification. However, more evaluation should be done on simulated EMGs, preferably surface EMGs with higher electrode numbers. These additional evaluations should also incorporate parameter optimization, whereby presence of a motor unit number estimation (MUNE) method and expected minimal MU firing frequencies would be beneficial.

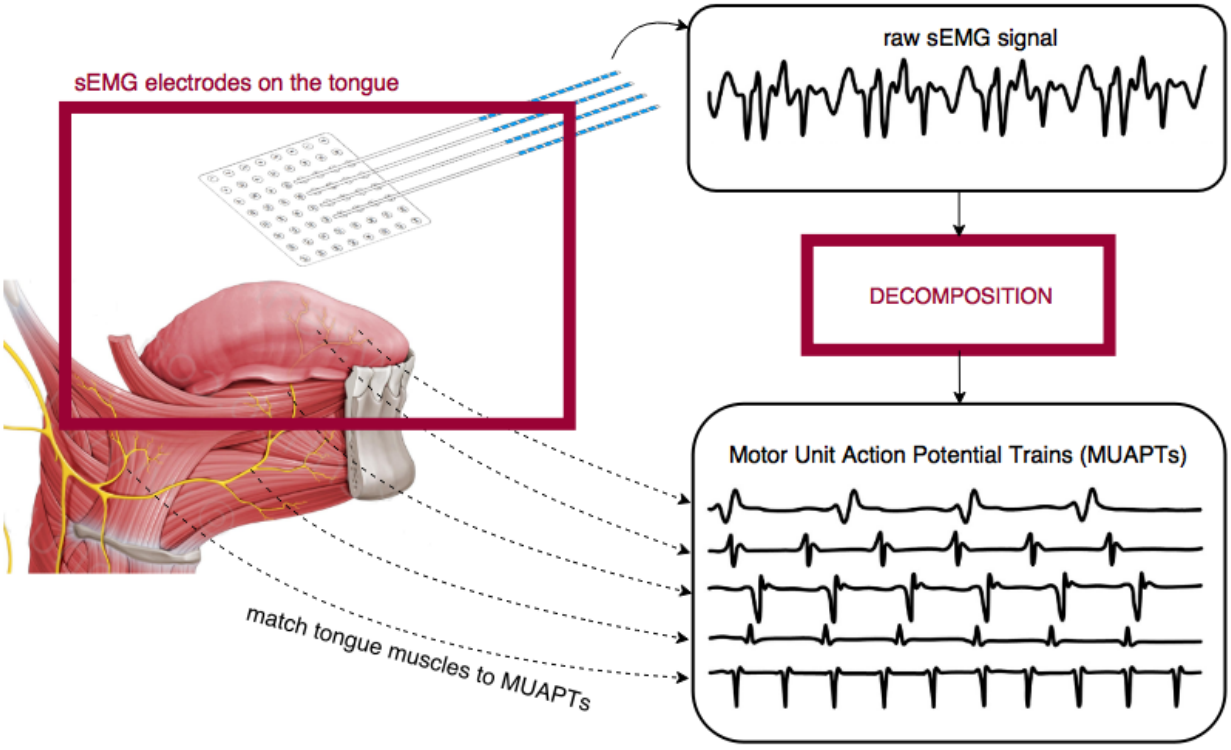
raw sEMG signal
sEMG electrodes on the tongue
DECOMPOSITION
Motor Unit Action Potential Trains (MUAPTs)
match tongue muscles to MUAPTs

5.1 INTRODUCTION

In this chapter the two selected grids from Chapter 3, the ECoG and Silic-12, are tested for measurement of sEMG signals on the tongue. Furthermore, the decomposition algorithm of Chapter 4 is applied to these sEMG signals to answer the question whether decomposition of tongue sEMG signals to derive individual MUAPTs is possible. This step brings the grid and decomposition development together and provides the possibility to evaluate these techniques for their ability to acquire neuromuscular information of various tongue muscles. Specifically, the quality of the sEMG signals and indications for tongue muscle identification are of interest.

5.2 METHOD

The Silic-12 and ECoG grid were both developed to be compatible with the Porti-system (TMSi, Oldenzaal, The Netherlands) (Figure 5.1 A). This system was used with the monopolar configuration, since it contains the entire information available from the detected signal [40], and preserves the possibility to use different configurations. Besides sEMG registration, the executed tongue movements were recorded with a 3D camera system (Figure 5.1 B). These recordings were used for identification of

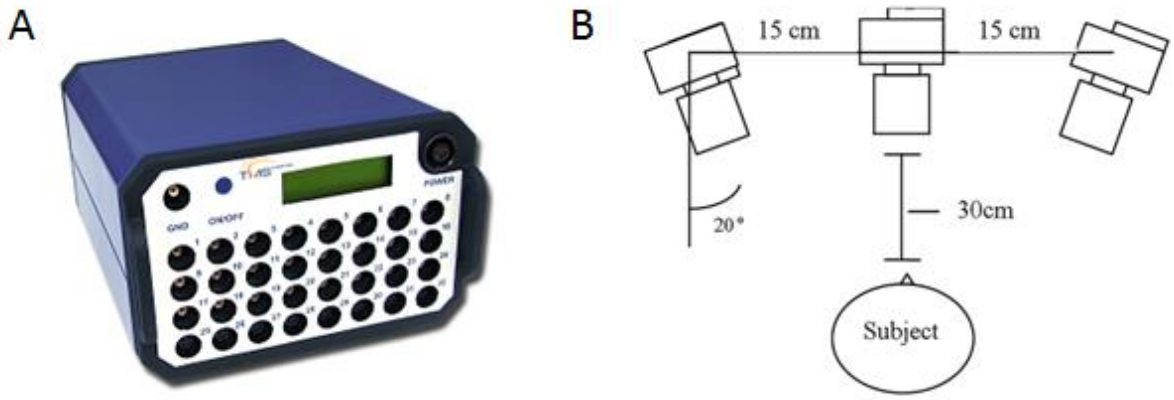

Figure 5.1 – Systems involved in sEMG measurements on the tongue. (A) The Porti-system with the maximum of 32 EMG channels. [68] (B) Schematic representation of the 3D camera system and positioning of the subject. (from above). [69]

tongue movements within the sEMG. Therefore, the surface EMGs were synchronised with the videos by transmission of a camera activation pulse to the Porti-system. For safety reasons, the sEMG measurements were not prepared by rubbing the tongue with medical abrasive paste and/or addition of conduction paste, normally used to reduce electrode-skin impedance [40]. However, the electrode-tongue noise was expected to be on a reasonable level due to the wet environment (Figure 5.2). As a reference, one micro electrode (TMSi, Oldenzaal, The Netherlands) was placed on the manubrium sterni, with additional conduction paste. Based on the results of Chapter 3, the Silic-12 was placed on the tongue

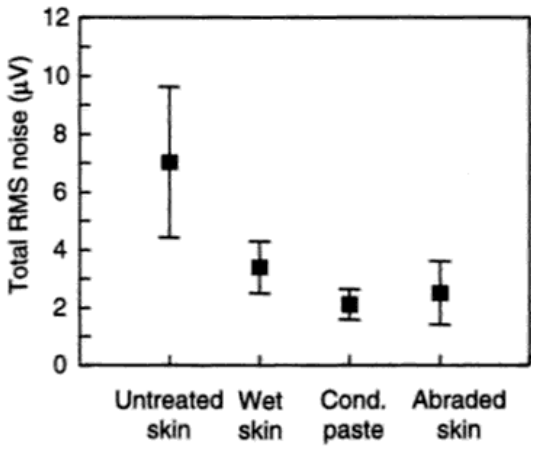

Figure 5.2 – Boxplot from Merletti and Hermens [40], who researched the influence of skin preparation on electrode noise. The measurements were done with two silver bars 10 mm long, 1 mm thick, 10 mm apart, on the m. biceps brachii. Since different electrodes were used within this thesis, the exact noise levels within this figure were not expected, it illustrates the relative influence of skin treatment.

without fixation, where the ECoG was fixated with denture prosthetic adhesive strips (Fittydent, Ridam Care BV, Breukelen, The Netherlands). After grid placement, the Porti and 3D camera system were started to record (in this order). Then six tasks were executed, being protrusion, tongue to the left, tongue to the right, tongue tip in direction of the chin, tongue tip in direction of the nose, and swallow. Each task, except task swallow, was persevered for 3 seconds and in between each task the tongue was rested in the mouth for a moment. This procedure of grid placement and six tasks was repeated four times per grid. These measurements facilitated evaluation of the sEMG quality per grid, in addition to the technical and practical scores from Chapter 3. One second of tongue sEMG was selected for decomposition with the KmCKC method from Chapter 4. The parameter settings were based on the results of EMG 5 and EMG 6 from Section 4.4.3 (Table 4.4): $K = 7$, $k = 50$, $nClus = 3$, $r = 5$, $h = 1$, $fc = 17$ H, $frac = 0.39$ and $nMU = 16$. Where r and h were based on literature about firing frequency of the GG muscle, since firing frequencies of other tongue muscles are unknown. For the GG muscle the firing frequencies range from 10-32 Hz, belonging to various tasks like protrusion [70], speech [71] and breathing [72]. Based on the results of Chapter 4, 10 was chosen for $r(h + 1)$. The decomposition results were inspected via visualization of the MU firing moments, back reconstruction of the sEMG and spatial spread on the tongue per MUAPT based on amplitude.

5.3 RESULTS

During sEMG measurements on the tongue, most of the electrodes of the Silic-12 showed minor dislocation artefacts (Figure 5.3 above), which was in line with the observed minor dislocation on the tongue. Electrode 3 and 7, located more posterior on the tongue, showed more dislocation artefacts. Especially electrode 3 was bad. The measurements with this electrode were excluded for further analysation. Besides, the electrodes marked as inoperable (Figure 3.7 C), electrode 4, 11 and 12, confirmed their inability to measure sEMG signals. Consequently, measurements from eight electrodes were left for further analysation. The ECoG grid measurements showed major dislocation artefacts, and even signal absence (Figure 5.3 below), which was in line with the observed dislocation and detachment of the grid. The ECoG electrodes marked as inoperable (Figure 3.5) appeared to be inoperable indeed, except for electrode 20, which detected some sEMG signals.

For decomposition of tongue sEMG the signals of Silic-12 were selected. sEMG signals with a duration of one second were selected in the second half of task 'right' (of the second session of tasks) since this task (part) contained least artefacts (Figure 5.3 above). The corresponding footage showed small rhythmic movements of the tongue during its position to the right. The decomposition resulted in 16 MUAPTs (since $nMU = 16$) (Figure 5.5) and their shapes per electrode. The mean firing rate of all MUAPTs was 37.4 ± 19.1 Hz. The MUAPTs and their shapes were used for sEMG reconstruction, showing similar excitations compared to the original sEMG (Figure 5.4). Furthermore, the MUAPT propagation over the tongue was visualized (Figure 5.6), where a wide variation of patterns was revealed.

5.4 DISCUSSION

Both the ECoG and Silic-12 grid showed movement artefacts in their tongue sEMG measurements, pointing out the importance of electrode fixation once again (Chapter 3). Especially the ECoG grid suffered major movement artefacts and the sEMG signals were therefore defined as unusable, which was expected to a certain extent after the test for practical use (Chapter 3). The Silic-12 was not fixated at all and showed, above expectations, relatively minor movement artefacts in most electrodes.

Due to decomposition of Silic-12 sEMG signals, sixteen MUAPTs and their firing moments were obtained (Figure 5.5). Some of the MUAPTs showed periods of higher firing frequencies, especially around 0.15 and 0.4 seconds. These could be related to the observed small rhythmic movements of the tongue during task 'right'. Another explanation could be the high firing frequencies (up to 150 Hz) at the start of a rapid muscle contraction [73]. These high firing rates decline slowly throughout the rest of the maximal contraction to rates as low as 20 Hz [73]. The applicability of the latter explanation could be doubted since this tongue 'right' task might not belong to the category of rapid and maximal contraction. Another observation, the mean firing frequency of 37.4 ± 19.1 Hz is considerably high when compared to the frequencies found in literature for the GG muscle (Section 5.1). Anatomical difference in muscle fibre type

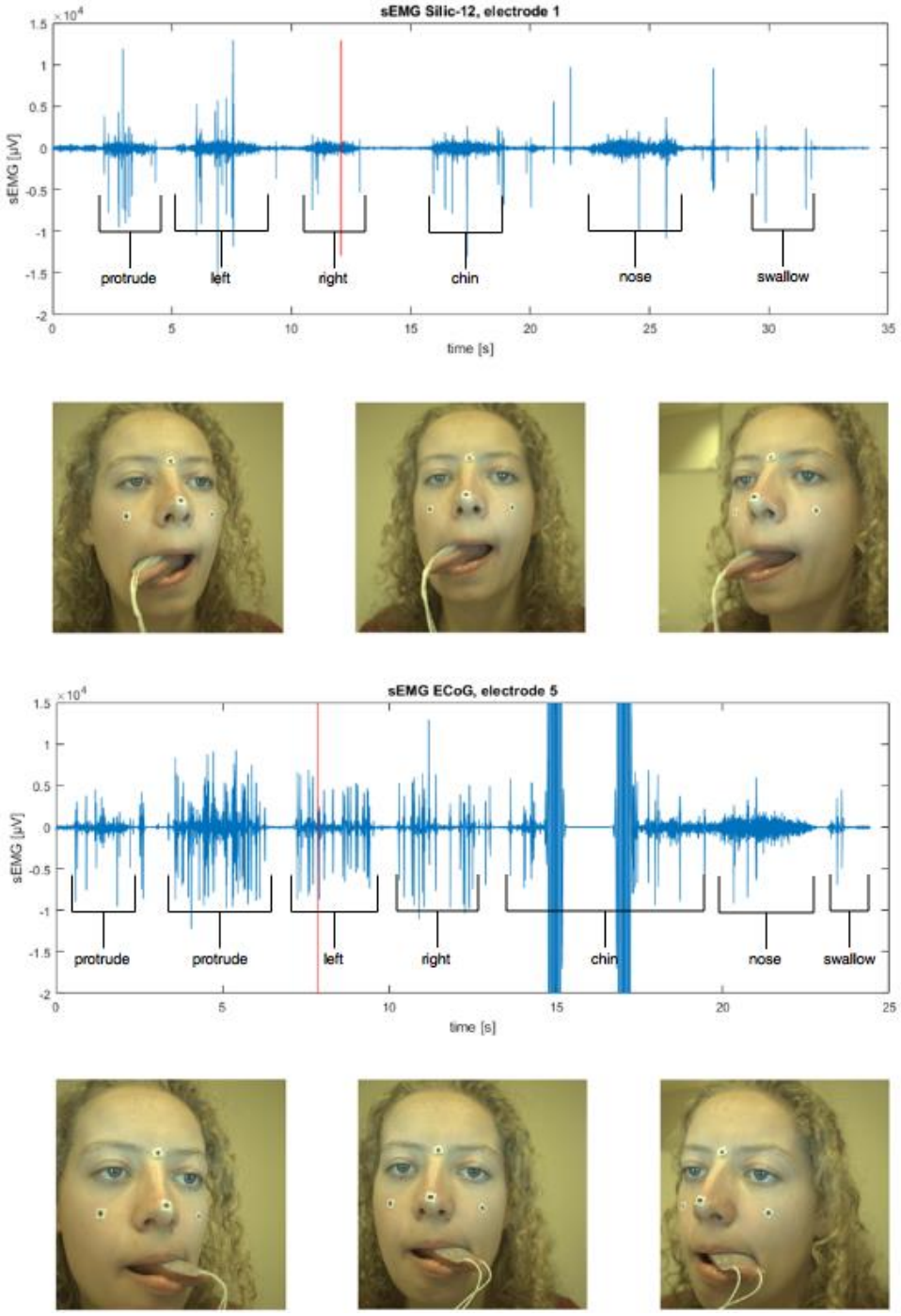

Figure 5.3 – sEMG measurements with the Silic-12 and ECoG grid, including task differentiation by video images. The vertical red line indicates the moment corresponding to the displayed video images. The markers on the face were placed for possible further research to the tongues range of motion. (Above) sEMG measurement with the Silic-12 grid and images from the 3D camera system during task 'right'. All long thin peaks visible are indicated as dislocation artefacts. (Below) sEMG measurement with the ECoG grid and images from the 3D camera system during task 'left'. The sEMG is full of dislocation artefacts (long thin peaks) and during task 'chin' major artifacts and signal absence is present due to a detachment.

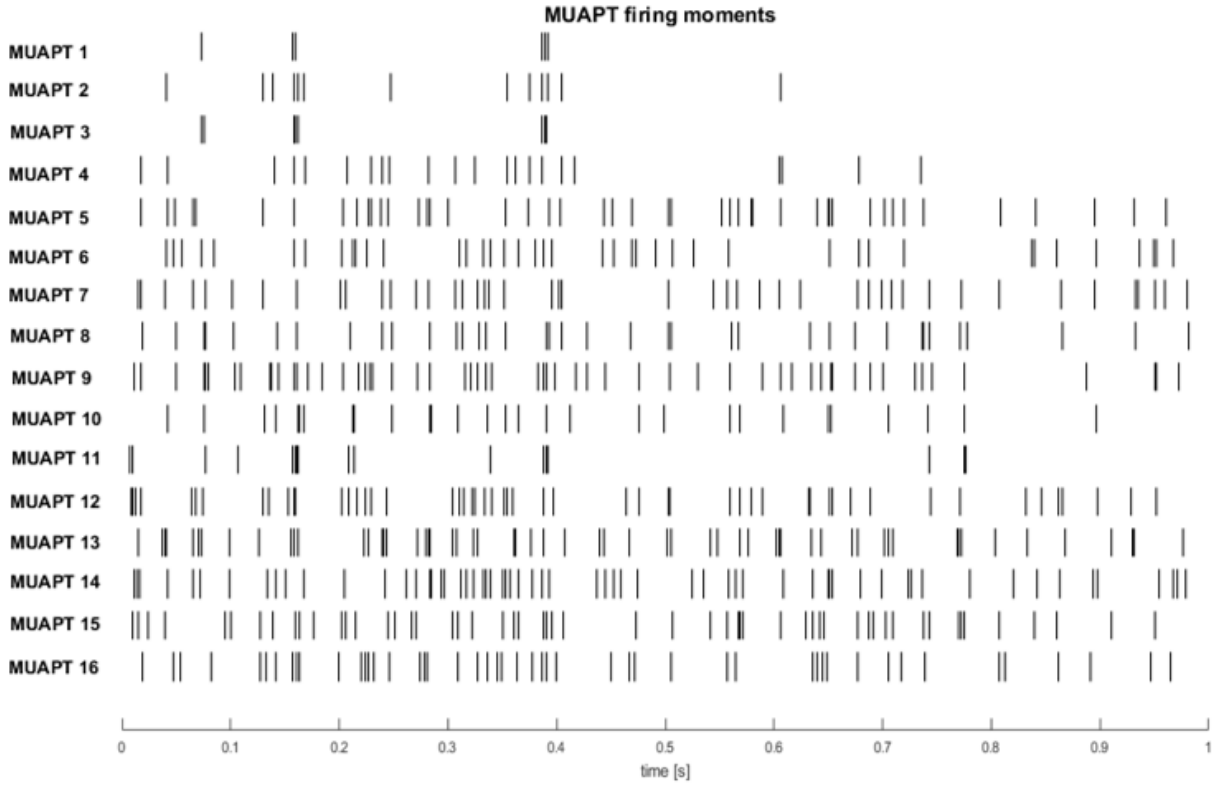

Figure 5.5 – Decomposition result of 1 second sEMG signals obtained with the Silic-12 during task 'right'. Each vertical line indicates a MU firing moment at a given time instant.

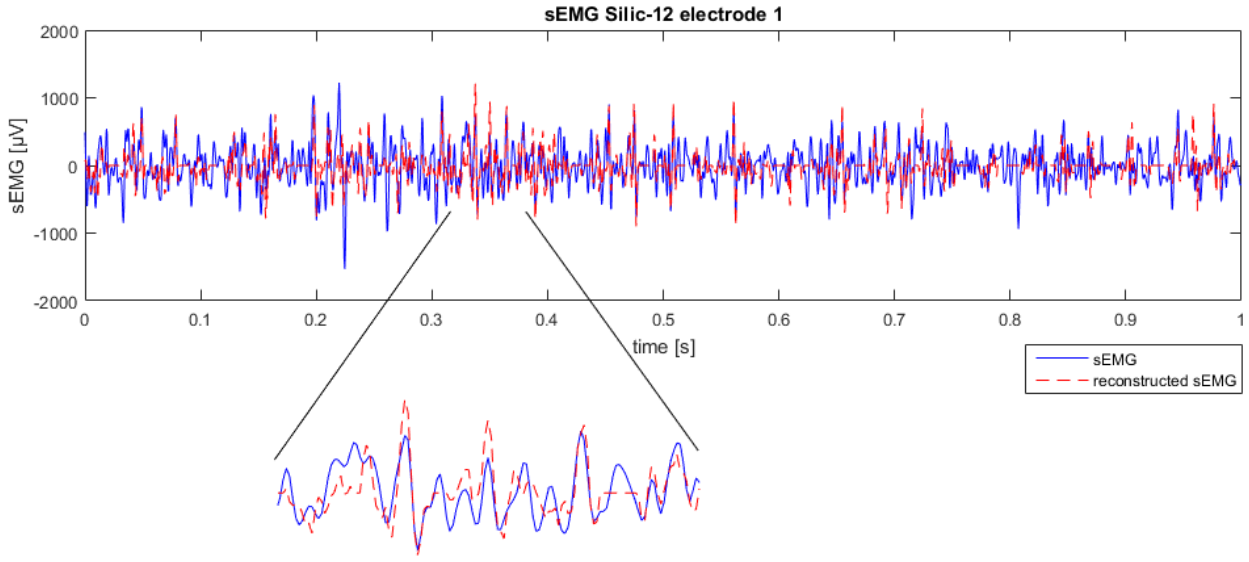

Figure 5.4 – The original sEMG and reconstructed sEMG of electrode 1, obtained with the Silic-12 during task 'right'. One part is magnified for a more detailed visualization.

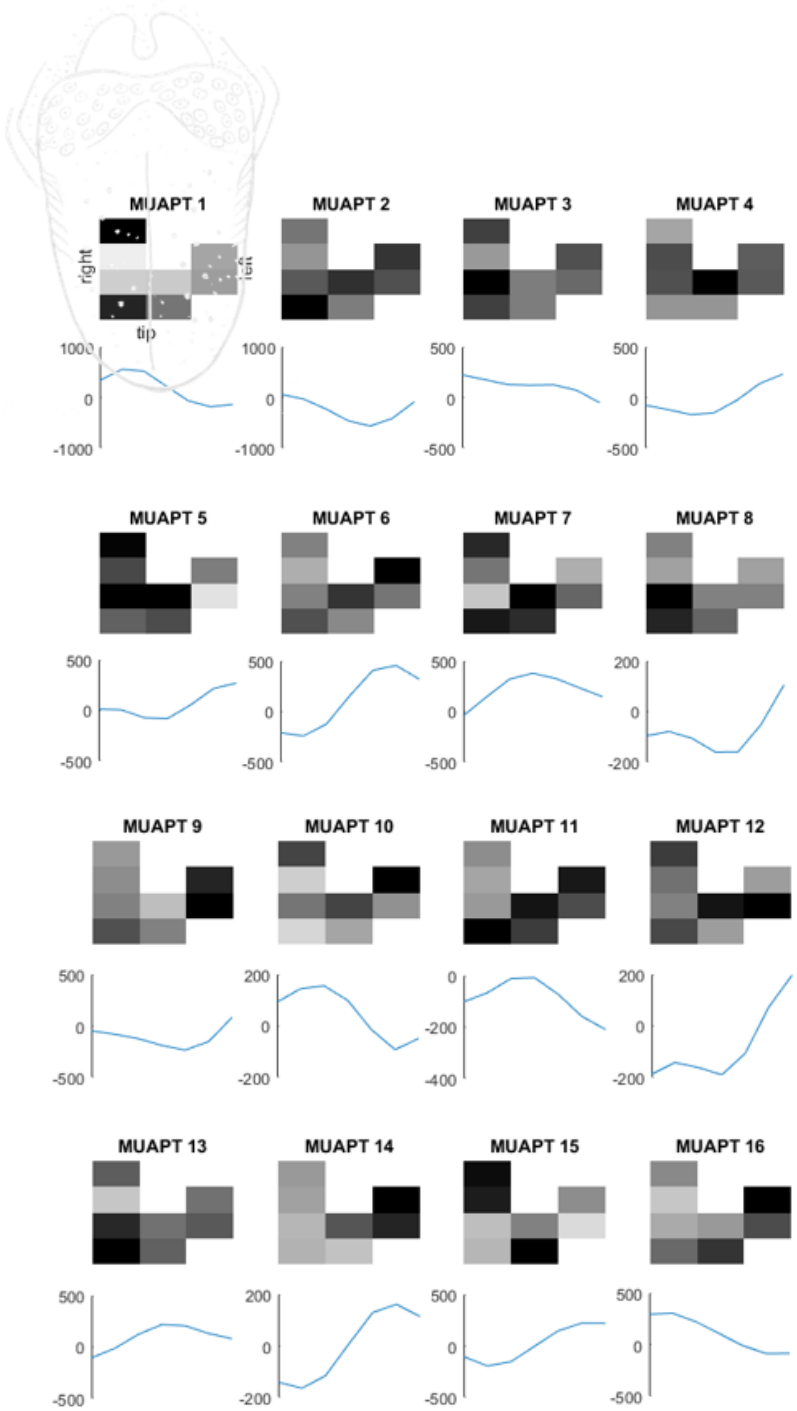

Figure 5.6 – All sixteen MUAPTs and their propagation over Silic-12. The eight grey to black rectangles indicated the operable electrodes, their position on the tongue is illustrated in the figure for MUAPT 1. The black to grey scale indicates the relative peak-to-peak amplitudes within the MUAPT, the highest peak-to-peak amplitude is represented by a black rectangle and this shape (with the peak-to-peak amplitude) is plotted below the Silic-12 visualization.

might underlie this. The majority of extrinsic muscle fibres are of type I, where intrinsic muscle fibres are mainly type II [74]–[77]. In addition, the muscle fibre type distribution within the intrinsic muscles varies for different tongue regions (Figure 5.7), from 40% type II fibres in the posterior tongue up to 75% in the anterior tongue [74]. Type II muscle fibres are fast twitch muscle fibres, which fatigue quickly and generate short-lasting bursts of strength, speed or phasic activities [79]. Conversely, type I muscle fibres are slow twitch muscle fibres, without fatigue, and therefore enable sustained or tonic activities [79]. These different muscle fibre phenotypes are strongly related to the neural activity. When fast or phasic motorneurons have been made to innervate a slow (type I) muscle, the muscle transforms to a fast (type II) muscle and vice versa [80]. Phasic motorneurons discharge at frequencies from 30-60 Hz, while with tonic motorneurones the frequency is usually 10-20 Hz [81]–[84]. The sEMG tongue signals probably consist

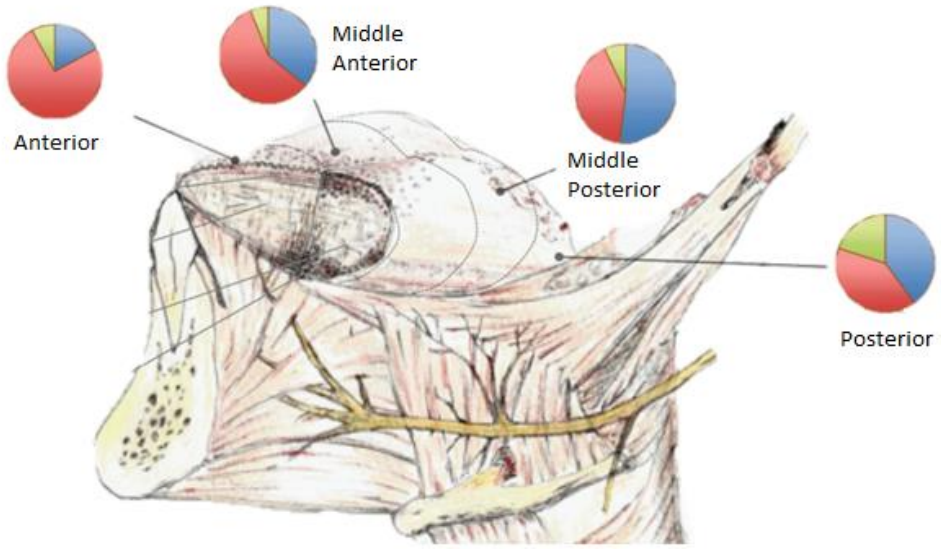

Figure 5.7 – Pie charts showing the distribution of fibre types in various locations of the tongue. Red represents type II fibres, blue type I fibres and green is a combination of both (IM and IIC fibres). [74][78]

mainly of intrinsic muscle signals, being mostly type II muscle fibres, which usually discharges at 30-60 Hz. This would explain the mean firing frequency of 37.4 ± 19.1 Hz found after decomposition. Another explanatory option would be that an estimated MUAPT includes multiple MUs or a high level of overshoot. High levels of overshoot were already observed after decomposition of simulated EMGs (Chapter 4). The only check done after decomposition in the experimental tongue sEMG setup, was reconstruction of the sEMG (summation of all shapes at their corresponding firing moments). The reconstructed sEMG (Figure 5.4) showed similar excitations compared to the original sEMG, suggesting the decomposition algorithm at least did not produce random results. Though, some excitations were missed at for instance 0.19, 0.6, 0.8 and 0.92 seconds. This might be caused by noise, too low nMU (remaining MUAPT) or missed firing moments of decomposed MUAPTs. For the same reasons, amplitude differences may have been too small. The sixteen MUAPTs after decomposition cannot all be regarded as correct. Both the simulation

results (Chapter 4) and experimental results of Ning et al. [1] underlie this. Ning et al. extracted with the KmCKC method up to 5 MUAPTs with the use of 16 electrodes on the first dorsal interosseous (FDI) muscle and 14 MUAPTs when 64 electrodes were used. Unfortunately, the sixteen tongue MUAPTs could not be revised, since neither there were needle EMGs performed, nor there were enough electrodes present for subgroup analysation (as Ning et al. [1] did). A possible MUAPT evaluation could have been the signal-based metric of Holobar et al. [85], which assesses accuracy of MU identification without any additional experimental costs. For this metric, so-called pulse-to-noise-ratio (PNR), an important 30 dB threshold was determined (involves sensitivity >90% and false alarm rate <2%) in both experimental and simulated signals. Another evaluation could have been the method of Parsaei et al. [86], their algorithm evaluates MUAP shape homogeneity, MU firing pattern consistency, and the estimated level of false classification errors in the MUAPT.

The sEMG measurements and its MUAPT propagations on the tongue allow speculation about the anatomical origin. First, the Silic-12 probably measured predominantly intrinsic tongue muscles. The earlier mentioned high firing frequencies suggest this, as well as an observation in within the different tasks. A low sEMG activity during task swallow was observed, surrounded by the dislocation artefacts during placement of the tongue against the palate and removal from the palate (Figure 5.3). In comparison to the other tasks the tongue had a flatter shape during swallowing, possibly linked to less intrinsic tongue muscle use, which could explain the lower sEMG activity. Although, literature states the use of both intrinsic and extrinsic tongue muscles during swallowing [87]. Second, the MUAPT propagations contributed to insight of which specific intrinsic tongue muscles were measured. Unfortunately, the four inoperable electrodes caused difficulties for evaluation of the propagation patterns. Therefore, the following statements should be regarded as tentative and explorative. MUAPT 4 (Figure 5.6) suggested activation of the m. transversus, since the highest peak-to-peak amplitude is located medial and it propagates in lateral directions. This corresponds to the medial innervation by the medial branch of n. hypoglossal (m-XII) (Figure 2.3 A and B) and the expected orientation of a transverse muscle fibre. More medial activations were observed in MUAPT 1, 3, 5, 7, 8, 13, and 15 (Figure 5.6), though differentiation between m. transversus and m. verticalis is ambiguous. In addition, MUAPT 5 could also be the propagation pattern of medial activation of the m. longitudinalis superior since the propagation is in anterior and posterior directions. More lateral, possibly m. longitudinalis superior activation was seen in MUAPT 9, 14, and 16 (Figure 5.6), since their propagation is in tongue tip direction and it showed a lateral origin. The lateral origin might be linked to the innervation via the lateral branch of the hypoglossal (l-XII) nerve (Figure 2.3 A and B). However, this propagation pattern could also be related to the m. longitudinalis inferior or m. styloglossus, though less likely since their greater distance from the measurement electrodes. In future research, the time-varying mean firing rates during various tasks per MU could be added as extra information, as De Luca et al. [8] did. This might contribute to the allocation of identified MUs to different tongue muscles.

5.5 CONCLUSION

In conclusion, the combination of Silic-12 sEMG measurements and KmCKC decomposition showed potential for acquisition of neuromuscular information from the superficial intrinsic tongue muscles. Even some tentative allocations of motor units to specific tongue muscles were made. Incorporation of more electrodes would increase MUAPT propagation information, which would increase certainty in MU allocation to different tongue muscles. Furthermore, improvement of grid fixation on the tongue would substantially improve the sEMG quality. For future use of these techniques, it is crucial to ensure correct decomposition by the KmCKC algorithm as the interpretation of the results of this algorithm remains difficult.

The first steps were made towards neuromuscular personalisation of the generic biomechanical tongue model. A tongue sEMG was successful acquired in one healthy subject with use of the newly developed Silic-12 electrode grid. However, several adjustments are desired to improve applicability and sEMG quality. The electrode grid should enable a firmer fixation to the tongue, hold more electrodes, and be more robust, while maintaining flexibility. The KmCKC decomposition algorithm showed reasonable results in simulated EMGs and was applied to the tongue sEMG for identification of individual motor units. Unfortunately, its performance in the tongue sEMG could not be verified. More research should be done to the KmCKC algorithm by parameter evaluation with simulated surface EMGs, for more reliable decomposition. Hereby, an expected minimal MU firing frequency and addition of a motor unit number estimation (MUNE) might appear beneficial. The MUAPT propagation patterns over the Silic-12 electrodes allowed some tentative allocations of MU activities to specific tongue muscles. Incorporation of more electrodes would increase MUAPT propagation information and therefore increase certainty in MU allocation to different tongue muscles. In short, the combination of sEMG measurements on the tongue with the Silic-12 grid and KmCKC decomposition algorithm showed potential for acquisition of neuromuscular information from the superficial intrinsic tongue muscles. Some major improvements should be made in future research before translation to input for the biomechanical tongue model can be initiated.

In future research, the tongue grid and the decomposition algorithm should be improved, to obtain reliable neuromuscular tongue information. Several solutions to the recurrent problem of fixation on the tongue were already mentioned (Section 3.5). In far future, a non-contact technique for muscle activation measurement would be ideal for this difficult measurement environment. A promising approach is the Laser Doppler myography (LDMi) (Figure 7.1), which appeared to be a valid measurement technique for assessment of muscle activity [89]. This technique is based on Laser Doppler Vibrometry (LDVi), a laser interferometric measurement instrument which enables precise muscle vibration measurements from distance and without skin contact [89]. There are several mechanisms behind the LDMi signal, all relating the vibration to the firing patterns of individual motor units, and the resultant mechanical pressure waves [88]. However, this technique has some limitations for tongue muscle activity measurements. Positioning of a laser beam to a specific tongue area during movement tasks is complex since the unique (non-skeletal) anatomy and displacement opportunities of the tongue. In addition, a decomposition method for motor unit pressure wave identification should be developed and a study should be done to the contribution of non-superficial pressure waves.

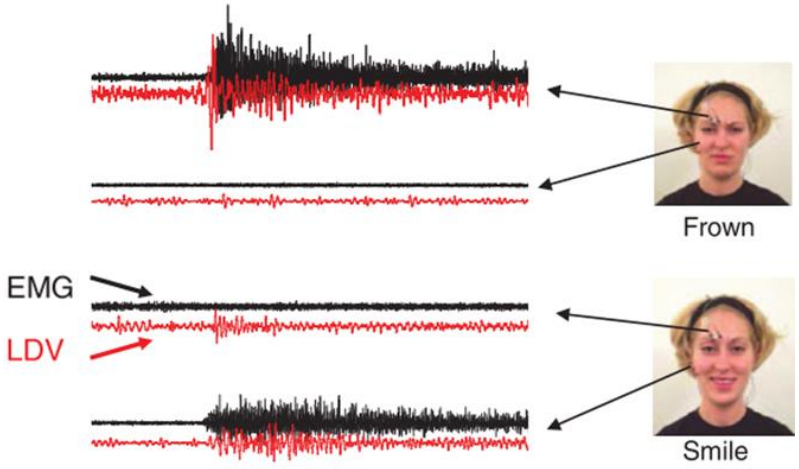

Figure 7.1 – Illustration of LDMi (LDV) and EMG of the m. corrugator and m. zygomaticus during two different facial expressions. [88]

Apart from the fixation problem, the gold standard (EMG), required the increase of electrode numbers. When the number of electrodes is significantly increased, more MU can be decomposed [45] and the optimal (complex) spatial filter arrangement [90][91] can be searched for, starting with NDD filter testing. Besides increase of electrode numbers, addition of electrode locations would provide information of extrinsic tongue muscles. Placement of a HD sEMG grid (TMSi, Oldenzaal, The Netherlands) (Figure 3.3 B) under the chin (Figure 2.5) may be useful for GG muscle measures, however accurate decomposition is required since its MUs should be distinguished from the mouth floor muscle MUs (m. geniohyoideus and

m. mylohyoideus). As mentioned in Section 3.5, addition of sEMG electrodes to the downside of the tongue might be an option, next to higher electrode density. In combination with decomposition and extra spatial filtering, it might be possible to reconstruct the 3D motor unit location within the tongue. The volume conductor between the MU and the electrodes acts on the MUAP as a spatial low-pass filter [92]. This low-pass characteristic causes action potentials of MUs located close to the recording electrodes to generate a spatially steeper potential distribution than MUs located more distant [44]. This spatial (shape) difference can be used for MU depth discrimination. When combined with the personal muscle fibre orientation, visualised with MRI techniques like diffusion tensor imaging (DTI) [93][94] (Figure 7.2) or constrained spherical deconvolution (CSD) [95], specific fibre bundle activation can be obtained. This would be of great value towards personalised (detailed) 3D neuromuscular information.

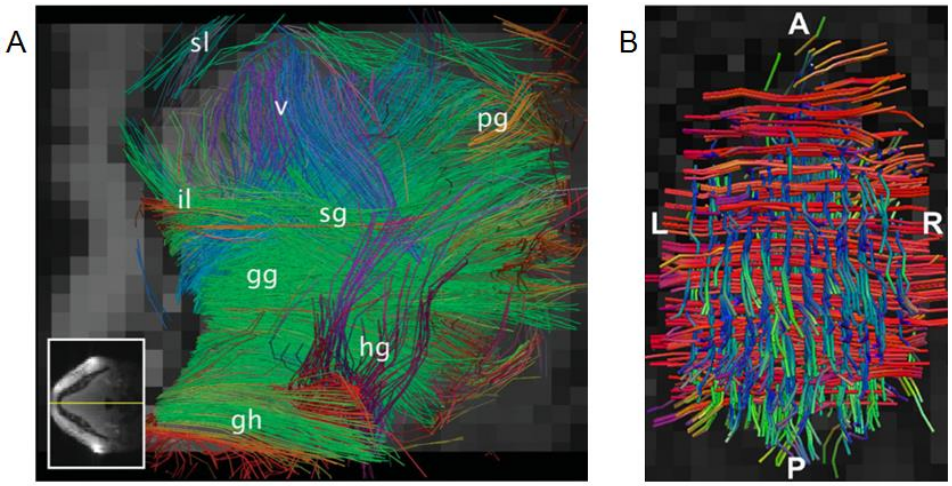

Figure 7.2 – DTI of the human tongue. (A) A sagittal view with the MRI slice location in the left lower corner. Individual muscle fibres of the tongue musculature are shown, and different muscles are indicated. [93] (B) A axial view with the standard DTI colour scheme (red: left-right; green: front-back; blue: up-down). Prior information was added to the DTI to distinguish interdigitated tongue muscles (transverse muscle in red). [94]

In prospect, when the neuromuscular information is successfully translated to input for the biomechanical tongue model, it will contribute to the goal of predicting personalised functional outcome after cancer treatment. The muscle (parts) planned to be affected by cancer treatment will be removed or changed in the tongue model (depending on the treatment), with the remaining muscle activity a functional prediction can be done. Besides, the combination of the personal neuromuscular information and the functional prediction might give insight in useful pre-treatment logopaedic exercises for muscle activity training. Apart from the Virtual Therapy goals, personal tongue neuromuscular information will be of great fundamental value itself since little is known about all complex neuromuscular varieties within the human tongue. It may provide essential information in understanding all kind of tongue related problems. One of them is the obstructive sleep apnoea syndrome (OSAS), were neuromuscular tongue information might be useful as part of a diagnostic protocol or function as a measure for indication of a n. hypoglossus stimulator (one of the treatment options).

REFERENCES

[1] Y. Ning, X. Zhu, S. Zhu, and Y. Zhang, "Surface EMG decomposition based on K-means clustering and convolution kernel compensation," *IEEE J Biomed Heal. Inform.*, vol. 19, no. 2, pp. 471–477, 2015.

[2] S. Warnakulasuriya, "Global epidemiology of oral and oropharyngeal cancer," *Oral Oncol.*, vol. 45, no. 4–5, pp. 309–316, 2009.

[3] IKNL, "Cijfers over kanker," 2017. [Online]. Available: http://www.cijfersoverkanker.nl/selecties/dataset_1/img582acd94be716?row=0&direction=down#table. [Accessed: 15-Nov-2017].

[4] S. M. Gore, A. K. Crombie, M. D. Batstone, and J. R. Clark, "Concurrent chemoradiotherapy compared with surgery and adjuvant radiotherapy for oral cavity squamous cell carcinoma," *Head Neck*, vol. 37, pp. 518–523, 2015.

[5] University of Twente, "Virtual therapy for head & neck cancer." [Online]. Available: http://www.virtualtherapy.nl/. [Accessed: 11-Nov-2016].

[6] M. Eskes, M. J. A. Van Alphen, A. J. M. Balm, L. E. Smeele, D. Brandsma, and F. Van Der Heijden, "Predicting 3D lip shapes using facial surface EMG," *PLoS One*, vol. 12, no. 4, pp. 1–16, 2017.

[7] K. L. Moore, A. F. Dalley, and A. M. R. Agur, *Clinically oriented anatomy*. 2010.

[8] C. J. De Luca, A. Adam, R. Wotiz, L. D. Gilmore, and S. H. Nawab, "Decomposition of surface EMG signals," *J Neurophysiol*, vol. 96, no. 3, pp. 1646–1657, 2006.

[9] "Anatomy learning resources," *DukeMedicine*, 2015. [Online]. Available: https://web.duke.edu/anatomy/Lab24/Lab24_clip_image002_0000.jpg. [Accessed: 15-Nov-2016].

[10] "Muscles of the tongue," *Kenhub*. [Online]. Available: https://www.kenhub.com/en/quizzes/the-muscles-of-the-tongue. [Accessed: 15-Nov-2016].

[11] L. Mu and I. Sanders, "Human tongue neuroanatomy: Nerve supply and motor endplates," *Clin. Anat.*, vol. 23, no. 7, pp. 777–791, 2010.

[12] S. Buchaillard, P. Perrier, and Y. Payan, "A biomechanical model of cardinal vowel production: muscle activations and the impact of gravity on tongue positioning.," *J. Acoust. Soc. Am.*, vol. 126, no. 4, pp. 2033–2051, 2009.

[13] K. D. R. Kappert, "Development of a surgical simulation tool for the prediction of functional impairment after partial glossectomy," University of Twente, 2016.

[14] M. Chen and P. Zhou, "A Novel Framework Based on FastICA for High Density Surface EMG Decomposition," *IEEE Trans. Neural Syst. Rehabil. Eng.*, vol. 24, no. 1, pp. 117–127, 2016.

[15] Pearson Education, "Motor Unit," 2012. [Online]. Available: https://image.slidesharecdn.com/apch6musclesstudentppt-121211103122-phpapp01/95/a-p-ch-6-musclular-system-student-ppt-21-638.jpg?cb=1355222071.

[16] "Motor Units." [Online]. Available: https://courses.washington.edu/conj/motor/motorunit.htm. [Accessed: 07-Dec-2016].

[17] K. van den Doel, U. M. Ascher, and D. K. Pai, "Computed myography: three-dimensional reconstruction of motor functions from surface EMG data," *Inverse Probl.*, vol. 24, no. 6, p. 65010, 2008.

[18] L. J. Raphael and F. Bell-Berti, "The role of the extrinsic and intrinsic tongue muscles in differentiating the English tense-lax vowel pairs." pp. 203–220, 1973.

[19] E. K. Sauerland and R. M. Harper, "The human tongue during sleep: Electromyographic activity of the genioglossus muscle," *Exp. Neurol.*, vol. 51, no. 1, pp. 160–170, 1976.

[20] T. Baer, P. J. Alfonso, and K. Honda, "Electromyography of the tongue muscles during vowels in /epvp/ environment," *Ann. Bull. RILP*, vol. 22, pp. 7–19, 1988.

[21] E. A. Doble, J. C. Leiter, S. L. Knuth, J. A. Daubenspeck, and D. Bartlett, “A noninvasive intraoral electromyographic electrode for genioglossus muscle,” *J. Appl. Physiol.*, vol. 58, no. 4, pp. 1378–1382, 1985.

[22] M. B. Blumen, A. Perez De La Sota, M. A. Quera-Salva, B. Frachet, F. Chabolle, and F. Lofaso, “Tongue mechanical characteristics and genioglossus muscle EMG in obstructive sleep apnoea patients,” *Respir. Physiol. Neurobiol.*, vol. 140, no. 2, pp. 155–164, 2004.

[23] C. M. O’Connor, M. M. Lowery, L. S. Doherty, M. McHugh, C. O’Muircheartaigh, J. Cullen, P. Nolan, W. T. McNicholas, and M. J. O’Malley, “Improved surface EMG electrode for measuring genioglossus muscle activity,” *Respir. Physiol. Neurobiol.*, vol. 159, no. 1, pp. 55–67, 2007.

[24] K. Yoshida, K. Takada, S. Adachi, and M. Sakuda, “Clinical Science: EMG Approach to Assessing Tongue Activity Using Miniature Surface Electrodes,” *J. Dent. Res.*, vol. 61, no. 10, pp. 1148–1152, 1982.

[25] D. Inagaki, Y. Miyaoka, I. Ashida, K. Ueda, and Y. Yamada, “Influences of body posture on duration of oral swallowing in normal young adults,” *J. Oral Rehabil.*, vol. 34, pp. 414–421, 2007.

[26] D. Inagaki, Y. Miyaoka, I. Ashida, and Y. Yamada, “Influence of food properties and body position on swallowing-related muscle activity amplitude,” *Journal of Oral Rehabilitation*, vol. 36, no. 3. pp. 176–183, 2009.

[27] R. Bekhuis, “Feasibility of movement classification of the tongue based on sEMG signals,” University of Twente, 2016.

[28] K. Englehart, B. Hudgins, P. A. Parker, and M. Stevenson, “Classification of the myoelectric signal using time-frequency based representations,” *Med. Eng. Phys.*, vol. 21, no. 6–7, pp. 431–438, 1999.

[29] K. E. Member, B. H. Member, P. A. Parker, and S. Member, “A Wavelet Based Continuous Classification Scheme for Multifunction Myoelectric Control,” *IEEE Trans. Biomed. Eng.*, vol. 48, no. 3, pp. 1–31, 2001.

[30] N. Jiang, K. B. Englehart, and P. A. Parker, “Extracting simultaneous and proportional neural control information for multiple-dof prostheses from the surface electromyographic signal,” *IEEE Trans. Biomed. Eng.*, vol. 56, no. 4, pp. 1070–1080, 2009.

[31] S. H. Nawab, S.-S. Chang, and C. J. De Luca, “High-yield decomposition of surface EMG signals,” *Clin. Neurophysiol.*, vol. 121, no. 10, pp. 1602–1615, 2010.

[32] D. Stashuk, “EMG signal descomposition: how can it be accomplished and used?,” *J. Electromyogr. Kinesiol.*, vol. 11, no. 1, pp. 151–173, 2001.

[33] H. R. Marateb and K. C. McGill, “Electromyographic (EMG) Decomposition,” *Wiley Encycl. Electr. Electron. Eng.*, pp. 1–15, 2016.

[34] M. Gazzoni, D. Farina, and R. Merletti, “A new method for the extraction and classification of single motor unit action potentials from surface EMG signals,” *J. Neurosci. Methods*, vol. 136, no. 2, pp. 165–177, 2004.

[35] B. U. Kleine, J. P. van Dijk, B. G. Lapatki, M. J. Zwarts, and D. F. Stegeman, “Using two-dimensional spatial information in decomposition of surface EMG signals,” *J. Electromyogr. Kinesiol.*, vol. 17, no. 5, pp. 535–548, 2007.

[36] B. U. Kleine, J. H. Blok, R. Oostenveld, P. Praamstra, and D. F. Stegeman, “Magnetic stimulation-induced modulations of motor unit firings extracted from multi-channel surface EMG,” *Muscle and Nerve*, vol. 23, no. 7, pp. 1005–1015, 2000.

[37] B. Lapatki, R. Oostenveld, J. van Dijk, I. Jonas, M. Zwarts, and D. Stegeman, “Topographical Characteristics of Motor Units of the Lower Facial Musculature Revealed by Means of High-Density Surface EMG,” *J. Neurophysiol.*, vol. 95, pp. 342–354, 2006.

[38] J. Akazawa and R. Okuno, “A method for quantitative SEMG decomposition and MUAP classification during voluntary isovelocity elbow flexion,” *Proc. Annu. Int. Conf. IEEE Eng. Med. Biol. Soc. EMBS*, pp. 6776–6779, 2013.

[39] A. Holobar and D. Zazula, “Multichannel blind source separation using convolution Kernel compensation,” *IEEE Transactions on Signal Processing*, vol. 55, no. 9. pp. 4487–4496, 2007.

[40] R. Merletti and H. J. Hermens, “5 Detection and conditioning of the surface EMG signal,” in *Electromyography: Physiology, Engineering, and Noninvasive Applications*, Hoboken, New Jersey: John Wiley & Sons, 2004, pp. 107–131.

[41] L. A. Geddes and L. E. Baker, *Principles of Applied Biomedical Instrumentation*. New York: Wiley, 1968.

[42] H. Broman, G. Bilotto, and C. J. De Luca, “Myoelectric signal conduction velocity and spectral parameters: influence of force and time,” *J.Appl.Physiol.*, vol. 58, no. 5, pp. 1428–1437, 1985.

[43] T. Masuda and T. Sadoyama, “The propagation of single motor unit action potentials detected by a surface electrode array,” *Electroencephalogr. Clin. Neurophysiol.*, vol. 63, no. 6, pp. 590–598, 1986.

[44] D. Farina, R. Merletti, and C. Disselhorst-Klug, “7 Multi-channel techniques for information extraction from the surface EMG,” in *Electromyography: Physiology, Engineering, and Noninvasive Applications*, 2004, pp. 169–203.

[45] D. Farina, F. Negro, M. Gazzoni, and R. M. Enoka, “Detecting the unique representation of motor-unit action potentials in the surface electromyogram,” *J. Neurophysiol.*, vol. 100, no. 3, pp. 1223–1233, 2008.

[46] F. Buchthal, C. Guld, and P. Risenfalck, “Volume conduction of the spike of the motor unit potential investigated with a new type of multielectrode,” *Acta Physiol Scand.*, vol. 38, no. 3–4, pp. 331–54, 1957.

[47] A. Gydikov, D. Kosarov, and N. Tankov, “Studying the alpha motoneurone activity by investigating motor units of various sizes,” *Electromyogr Clin Neurophysiol.*, vol. 12, no. 2, pp. 99–117, 1972.

[48] K. Roeleveld, D. F. Stegeman, H. M. Vingerhoets, and A. Van Oosterom, “Motor unit potential contribution to surface electromyography,” *Acta Physiol. Scand.*, vol. 160, no. 2, pp. 175–183, 1997.

[49] K. Roeleveld, D. F. Stegeman, H. M. Vingerhoets, and M. Zwarts, “How inter-electrode distance and motor unit depth influence surface potentials,” *SENIAM 5: The state of the art on sensors and sensor placement procedure in surface EMG, Roessingh Research and Development, Enschede, The Netherlands*, p. 55, 1997.

[50] C. J. De Luca, M. Kuznetsov, L. D. Gilmore, and S. H. Roy, “Inter-electrode spacing of surface EMG sensors: Reduction of crosstalk contamination during voluntary contractions,” *J. Biomech.*, vol. 45, no. 3, pp. 555–561, 2012.

[51] Smooth-On, “Ecoflex Series,” 2017. [Online]. Available: https://www.smooth-on.com/product-line/ecoflex/. [Accessed: 31-May-2017].

[52] M. S. Fifer, M. Mollazadeh, S. Acharya, N. V Thakor, and N. E. Crone, “Asynchronous Decoding of Grasp Aperture from Human ECoG During a Reach-to-Grasp Task,” in *IEEE Eng Med Biol Soc.*, 2011, pp. 4584–4587.

[53] Medasil, “Silicone Silastic Sheet.” [Online]. Available: http://www.medasil.com/product/silicone-silastic-sheet/. [Accessed: 08-May-2017].

[54] ProCare, “Strässle Easy II Zuigelektrodensysteem,” 2017. [Online]. Available: https://www.procarebv.nl/product/strassle-easy-ii-zuigelektrodensysteem/.

[55] NanoGriptech, “Setex.” [Online]. Available: http://nanogriptech.com/products/gripping-friction-material.

[56] Techaw, “Tongue2Teeth Wants You to Use Your Tongue to Clean Your Teeth,” 2013. [Online]. Available: http://www.techaw.com/tongue2teeth-wants-you-to-use-your-tongue-to-clean-your-teeth/.

[57] Techaw, “Tongue Cover Guards You from Any Bitter Exposure,” 2013. [Online]. Available: http://www.techaw.com/tongue-cover-guards-you-from-any-bitter-exposure/.

[58] “Harvard Researchers Manufacture Flexible and Wearable Electronics by Hybrid 3D Printing,” *D Printing Media Network*, 2017. [Online]. Available: https://www.3dprintingbusiness.directory/news/harvard-researchers-manufacture-flexible-wearable-electronics-hybrid-3d-printing/. [Accessed: 16-Oct-2017].

[59] A. Holobar and D. Zazula, “Gradient Convolution Kernel Compensation Applied to Surface Electromyograms,” *Indep. Compon. Anal. Signal Sep.*, vol. 4666, pp. 617–624, 2007.

[60] A. Holobar and D. Zazula, “Correlation-based decomposition of surface electromyograms at low contraction

forces," *Med. Biol. Eng. Comput.*, vol. 42, no. 4, pp. 487–495, 2004.

[61] A. Hamilton-Wright and D. W. Stashun, "Physiologically based simulation of clinical EMG signals," *IEEE Trans Biomed Eng.*, vol. 52, pp. 171–183, 2005.

[62] "EMGLAB: A forum for sharing software, data, and information related to EMG decomposition," *2007*. [Online]. Available: http://www.emglab.net/.

[63] D. Farina and R. Merletti, "A novel approach for precise simulation of the EMG signal detected by surface electrodes," *IEEE Trans Biomed Eng.*, vol. 48, no. 6, pp. 637–646, 2001.

[64] J. McCall, "Genetic algorithms for modelling and optimisation," *J. Comput. Appl. Math.*, vol. 184, no. 1, pp. 205–222, 2005.

[65] M. Kozak, "Comparison of Random Search Method and Genetic Algorithm for Stratification," *Commun. Stat. - Simul. Comput.*, vol. 43, no. 2, pp. 249–253, 2014.

[66] D. W. Stashuk, D. Farina, and K. Søgaard, "3 Decomposition of intramuscular EMG signals," in *Electromyography: Physiology, Engineering, and Noninvasive Applications*, 2004, pp. 47–77.

[67] M. B. I. Reaz, M. S. Hussain, and F. Mohd-Yasin, "Techniques of EMG signal analysis: detection, processing, classification and applications," *Biol. Proced. Online*, vol. 8, no. 1, pp. 163–163, 2006.

[68] TMSi, "Porti." [Online]. Available: https://www.tmsi.com/products/systems/item/porti. [Accessed: 18-Sep-2017].

[69] S. van Dijk, M. J. A. van Alphen, I. Jacobi, L. E. Smeele, F. van der Heijden, and A. J. M. Balm, "A New Accurate 3D Measurement Tool to Assess the Range of Motion of the Tongue in Oral Cancer Patients: A Standardized Model," *Dysphagia*, vol. 31, no. 1, pp. 97–103, 2016.

[70] E. F. Bailey, A. D. Rice, and A. J. Fuglevand, "Firing Patterns of Human Genioglossus Motor Units During Voluntary Tongue Movement," *J. Neurophysiol.*, vol. 97, no. 1, pp. 933–936, 2007.

[71] K. R. Shumway, D. J. Porfirio, and E. F. Bailey, "Phonation related rate coding and recruitment in the genioglossus muscle," *Exp. Brain Res.*, vol. 233, no. 7, pp. 165–187, 2015.

[72] P. A. Richardson and E. F. Bailey, "Tonically discharging genioglossus motor units show no evidence of rate coding with hypercapnia," *J Neurophysiol*, vol. 103, no. 3, pp. 1315–1321, 2010.

[73] J. C. Rothwell, *Control of human voluntary movement*. 1987.

[74] P. Stal, S. Marklund, L. E. Thornell, R. De Paul, and P. O. Eriksson, "Fibre composition of human intrinsic tongue muscles," *Cells Tissues Organs*, vol. 173, no. 3, pp. 147–161, 2003.

[75] H. Saigusa, S. Niimi, T. Gotoh, K. Yamashita, and M. Kumada, "Morphological and histochemical studies of the genioglossus muscle," *Ann. Otol. Rhinol. Laryngol.*, vol. 110, no. 8, pp. 779–784, 2001.

[76] A. J. Sokoloff, B. Yang, H. Li, and T. J. Burkholder, "Immunohistochemical characterization of slow and fast myosin heavy chain composition of muscle fibres in the styloglossus muscle of the human and macaque (Macaca rhesus)," *Arch. Oral Biol.*, vol. 52, no. 6, pp. 533–543, 2007.

[77] A. J. Sokoloff, M. Daugherty, and H. Li, "Myosin heavy-chain composition of the human hyoglossus muscle," *Dysphagia*, vol. 25, no. 2, pp. 81–93, 2010.

[78] F. N. Zaidi, P. Meadows, O. Jacobowitz, and T. M. Davidson, "Tongue anatomy and physiology, the scientific basis for a novel targeted neurostimulation system designed for the treatment of obstructive sleep apnea," *Int. Neuromodulation Soc.*, 2012.

[79] W. Scott, J. Stevens, and S. A. Binder-macleod, "Human Skeletal Muscle Fiber Type Classifications," *Phys Ther.*, vol. 81, no. 11, pp. 1810–1816, 2001.

[80] A. J. Buller, J. C. Eccles, and R. M. Eccles, "Interactions between motoneurones and muscles in respect of the characteristic speeds of their responses," *J. Physiol.*, vol. 150, no. 2, pp. 417–439, 1960.

[81] D. Denny-Brown, "On the nature of postural reflexes," *Proc. Roy. Soc. B*, vol. 104, pp. 253–301, 1929.

[82] E. D. Adrian and K. Umrath, “The impulse discharge from the Pacinian corpuscle,” *J. Physiol.*, vol. 68, pp. 139–154, 1929.

[83] R. Granit, H. D. Henatsch, and G. Steg, “Tonic and phasic ventral horn cells differentiated by post-tetanic potentiation in cat extensors,” *Acta Physiol Scand.*, vol. 37, pp. 114–126, 1956.

[84] R. Granit, C. G. Philips, S. Skoglund, and G. Steg, “Differentiation of tonic from phasic alpha ventral horn cells by stretch, pinna and crossed extensor reflexes,” *J. Physiol.*, vol. 20, pp. 470–481, 1957.

[85] A. Holobar, M. A. Minetto, and D. Farina, “Accurate identification of motor unit discharge patterns from high-density surface EMG and validation with a novel signal-based performance metric,” *J. Neural Eng.*, vol. 11, no. 1, p. 16008, 2014.

[86] H. Parsaei and D. W. Stashuk, “Automatic validation of motor unit potential trains extracted by EMG signal decomposition,” in *24th Canadian Conference on Electrical and Computer Engineering (CCECE)*, 2011.

[87] S. M. Felton, T. A. Gaige, T. G. Reese, V. J. Wedeen, and R. J. Gilbert, “Mechanical basis for lingual deformation during the propulsive phase of swallowing as determined by phase-contrast magnetic resonance imaging,” *J. Appl. Physiol.*, vol. 103, pp. 255–265, 2007.

[88] J. W. Rohrbaugh, E. J. Sirevaag, and E. J. Richter, “Laser Doppler vibrometry measurement of the mechanical myogram,” *AIP Conf. Proc.*, vol. 1457, pp. 266–274, 2012.

[89] L. Scalise, S. Casaccia, P. Marchionni, I. Ercoli, and E. Tomasini, “Laser doppler myography (LDMi): A novel non-contact measurement method for the muscle activity,” *Laser Ther.*, vol. 22, no. 4, pp. 261–8, 2013.

[90] C. Disselhorst-Klug, J. Silny, and G. Rau, “Improvement of spatial resolution in surface-EMG: a theoretical and experimental comparison of different spatial filters,” *IEEE Trans. Biomed. Eng.*, vol. 44, no. 7, pp. 567–574, 1997.

[91] D. Farina and A. Rainoldi, “Compensation of the effect of sub-cutaneous tissue layers on surface EMG: A simulation study,” *Med. Eng. Phys.*, vol. 21, no. 6–7, pp. 487–497, 1999.

[92] L. H. Lindström and R. I. Magnusson, “Interpretation of Myoelectric Power Spectra: A Model and Its Applications,” *Proc. IEEE*, vol. 65, no. 5, pp. 653–662, 1977.

[93] T. A. Gaige, T. Benner, R. Wang, V. J. Wedeen, and R. J. Gilbert, “Three dimensional myoarchitecture of the human tongue determined in vivo by diffusion tensor imaging with tractography,” *J. Magn. Reson. Imaging*, vol. 26, no. 3, pp. 654–661, 2007.

[94] C. Ye, E. Murano, M. Stone, and J. L. Prince, “A Bayesian approach to distinguishing interdigitated tongue muscles from limited diffusion magnetic resonance imaging,” *Comput. Med. Imaging Graph.*, vol. 45, pp. 63–74, 2015.

[95] L. Voskuilen, V. Mazzoli, J. Oudeman, L. E. Smeele, A. J. M. Balm, F. Van der Heijden, M. Froeling, G. J. Strijkers, and A. J. Nederveen, “Crossing muscle fibres in the tongue resolved using constrained spherical deconvolution,” in *ISMRM 26th Annual Meeting & Exhibition*, 2017, p. #5006.

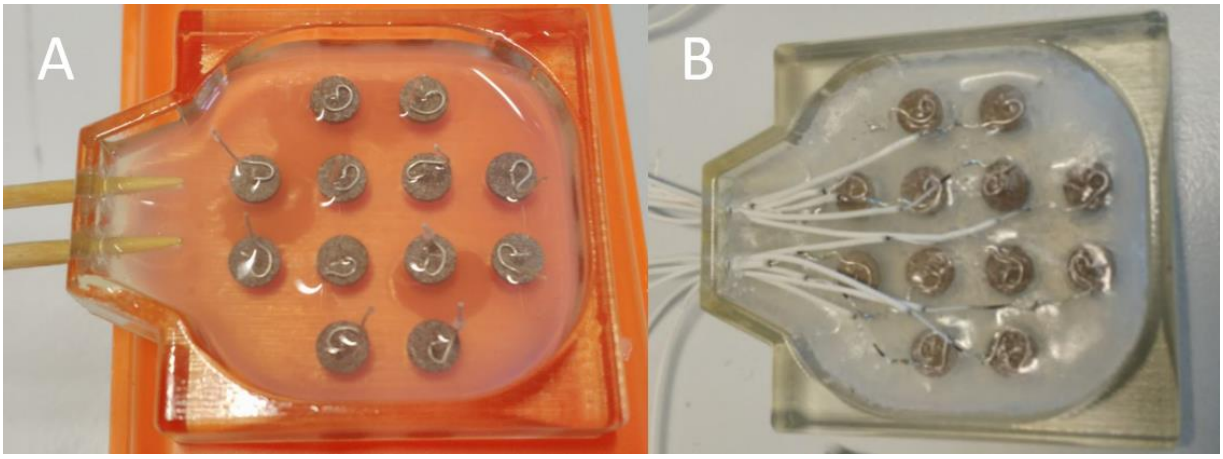

Figure A1 – Prototype sEMG grid building in the mould. (A) The first layer of silicone and the 12 electrodes with bended leads. Two wooden sticks were added for keeping open the canal for the electrode cables. (B) The electrode cables were soldered to the electrode leads.

A2 - An activity measure of a single source and a single sensor[1]

1. Signal model

A single source is considered that generates a time series $s(n)$ with $n = 1, 2, \ldots$. This source generates a sequence of short pulses, i.e. a time discrete version of a Poisson point process. Such a sequence is characterized by the density P_{rate} (mean number of pulses per unit time), and an amplitude. The sequence is uncorrelated with expectation μ_s and standard deviation σ_s given by:

$$\begin{aligned} \mu_s &= E[s] = aP_{rate} + b(1 - P_{rate}) \\ E[s^2] &= a^2 P_{rate} + b^2(1 - P_{rate}) \\ \sigma_s^2 &= E[s^2] - \mu_s^2 = P_{rate}(1 - P_{rate})(a - b)^2 \end{aligned} \tag{1}$$

with a the pulse height, and b the signal level between pulses.

The activity of this source is measured by means of a surface electrode. The observed voltage is denoted by $x(n)$. It is assumed that the relation between the source and the measurement is given by a convolution with finite impulse response $h(n)$ with $n = 0, \cdots, P-1$:

$$x(n) = \sum_{k=0}^{P-1} s(n-k)h(k) \tag{2}$$

[1] This appendix is a result of a joint effort of F. van der Heijden and E.S. van Staveren.

This process can be brought into matrix-vector notation as follows:

$$x(n) = \begin{bmatrix} h(0) & h(1) & \cdots & h(P-1) \end{bmatrix}^T \begin{bmatrix} s(n) \\ s(n-1) \\ \vdots \\ s(n-P+1) \end{bmatrix} \tag{3}$$

For the analysis it is useful to have not only $x(n)$, but also the past K values $x(n-1),\ \cdots,\ x(n-K+1)$ captured in one vector. Therefore, the vectors are defined as:

$$\bar{\mathbf{x}}(n) \overset{def}{=} \begin{bmatrix} x(n) \\ x(n-1) \\ \vdots \\ x(n-K+1) \end{bmatrix} \text{ and } \mathbf{s}(n) \overset{def}{=} \begin{bmatrix} s(n) \\ s(n-1) \\ \vdots \\ s(n-K-P+2) \end{bmatrix} \tag{4}$$

and a matrix:

$$\mathbf{H} \overset{def}{=} \underbrace{\left.\begin{bmatrix} h(0) & h(1) & \cdots & h(P-1) & 0 & 0 & \cdots & & 0 \\ 0 & h(0) & h(1) & \cdots & h(P-1) & 0 & 0 & & 0 \\ & 0 & h(0) & h(1) & \cdots & h(P-1) & 0 & 0 & \\ & & 0 & \ddots & & & \ddots & 0 & 0 \\ 0 & \cdots & & 0 & \ddots & & & 0 & 0 \\ 0 & & & & & & & \ddots & 0 \\ 0 & 0 & 0 & & 0 & h(0) & h(1) & \cdots & h(P-1) \end{bmatrix}\right\} K \text{ rows}}_{P+K-1 \text{ columns}} \tag{5}$$

to arrive at a model:

$$\bar{\mathbf{x}}(n) = \mathbf{H}\mathbf{s}(n) + \mathbf{e}(n) \tag{6}$$

where $\mathbf{e}(n)$ is a vector representing the sensor noise. The standard deviation of the noise is σ_n.

2. Activity index

For the sake of brevity, it is assumed that the mean of $\mathbf{s}(n)$ will be zero. Under this condition, the covariance matrix of $\mathbf{s}(n)$ is defined as the $K \times K$ matrix $\mathbf{C}_\mathbf{s} = \mathrm{E}\left[\mathbf{s}(n)\mathbf{s}(n)^T\right]$. Since $s(n)$ is uncorrelated, $\mathrm{E}\left[s(n)s(m)\right] = 0$ for $n \neq m$. Therefore, $\mathbf{C}_\mathbf{s} = \sigma_s^2\mathbf{I}$. Likewise, the noise covariance matrix is $\mathbf{C}_\mathbf{e} = \sigma_n^2\mathbf{I}$. Using the property that $\mathrm{E}\left[\mathbf{H}\mathbf{s}(n)\mathbf{s}(n)^T\mathbf{H}^T\right] = \mathbf{H}\mathrm{E}\left[\mathbf{s}(n)\mathbf{s}(n)^T\right]\mathbf{H}^T$ the covariance matrix of $\bar{\mathbf{x}}(n)$ becomes:

$$\mathbf{C}_\mathbf{x} = \mathbf{H}\mathbf{C}_\mathbf{s}\mathbf{H}^T + \sigma_n^2\mathbf{I} = \sigma_s^2\mathbf{H}\mathbf{H}^T + \sigma_n^2\mathbf{I} \tag{7}$$

The next step is to calculate the activity index defined as:

$$\gamma(n) = \bar{\mathbf{x}}(n)^T \hat{\mathbf{C}}_{\mathbf{x}}^{-1} \bar{\mathbf{x}}(n) \tag{8}$$

in which $\hat{\mathbf{C}}_{\mathbf{x}}$ is an estimate of the covariance matrix using an observation of vectors $\bar{\mathbf{x}}(n)$.

3. Interpretation of activity index

To see what this activity index represents, the following theorems will be applied:

Theorem 1: singular value decomposition

Any $K \times L$ matrix $\mathbf{H}$ can be decomposed into an orthonormal $K \times K$ matrix $\mathbf{V}$, a diagonal $K \times L$ matrix $\mathbf{S}$, and a second orthonormal $L \times L$ matrix $\mathbf{W}$:

$$\mathbf{H} = \mathbf{V}\mathbf{S}\mathbf{W}^T$$

Theorem 2:

Any covariance matrix $\mathbf{C}$ can be decomposed into an orthonormal matrix $\mathbf{V}$ and a diagonal matrix $\mathbf{L}$:

$$\mathbf{C} = \mathbf{V}\mathbf{L}\mathbf{V}^T$$

The matrices $\mathbf{V}$ and $\mathbf{L}$ are obtained as the solutions from the eigenvalue problem: $\mathbf{C}\mathbf{v}_k = \ell_k \mathbf{v}_k$, with:

$$\mathbf{V} = \begin{bmatrix} \mathbf{v}_1 & \cdots & \mathbf{v}_K \end{bmatrix} \text{ and } \mathbf{L} = \text{diag}\left(\ell_1, \cdots, \ell_K\right)$$

Corollary:

If $\mathbf{v}$ is an eigenvector of $\mathbf{C}$, and ℓ is the corresponding eigenvalue, then $\mathbf{v}$ is also an eigenvector of the matrix $\mathbf{C} + \alpha\mathbf{I}$. The corresponding eigenvalue is $\ell + \alpha$.

Application of theorem 2 to $\mathbf{C}_{\mathbf{x}}$ in (7) shows that $\mathbf{V}$ and $\mathbf{L}$ are the eigenvectors/values of $\mathbf{H}\mathbf{H}^T$ so that $\mathbf{C}_{\mathbf{x}} = \mathbf{V}\left(\sigma_s^2\mathbf{L} + \sigma_n^2\mathbf{I}\right)\mathbf{V}^T$. Consequently:

$$\begin{aligned} \mathbf{C}_{\mathbf{x}}^{-1} &= \left(\mathbf{V}(\sigma_s^2\mathbf{L} + \sigma_n^2\mathbf{I})^{\frac{1}{2}}(\sigma_s^2\mathbf{L} + \sigma_n^2\mathbf{I})^{\frac{1}{2}}\mathbf{V}^T\right)^{-1} \\ &= \left((\sigma_s^2\mathbf{L} + \sigma_n^2\mathbf{I})^{\frac{1}{2}}\mathbf{V}^T\right)^{-1}\left(\mathbf{V}(\sigma_s^2\mathbf{L} + \sigma_n^2\mathbf{I})^{\frac{1}{2}}\right)^{-1} \\ &= \mathbf{V}(\sigma_s^2\mathbf{L} + \sigma_n^2\mathbf{I})^{-\frac{1}{2}}(\sigma_s^2\mathbf{L} + \sigma_n^2\mathbf{I})^{-\frac{1}{2}}\mathbf{V}^T \end{aligned} \tag{9}$$

Furthermore, since $\mathbf{H} = \mathbf{V}\mathbf{S}\mathbf{W}^T$ (theorem 1) and $\mathbf{H}\mathbf{H}^T = \mathbf{V}\mathbf{L}\mathbf{V}^T$ (theorem 2), $\mathbf{S} = \mathbf{L}^{\frac{1}{2}}$ and $\mathbf{H} = \mathbf{V}\mathbf{L}^{\frac{1}{2}}\mathbf{W}^T$, so that according to (6):

$$\bar{\mathbf{x}}(n) = \mathbf{V}\mathbf{L}^{\frac{1}{2}}\mathbf{W}^T\mathbf{s}(n) + \mathbf{e}(n) \tag{10}$$

Substitution of (9) and (10) in (8) yields:

$$\begin{aligned}\gamma(n) &\approx \left(\mathbf{V}\mathbf{L}^{\frac{1}{2}}\mathbf{W}^T\mathbf{s}(n)+\mathbf{e}(n)\right)^T \mathbf{V}(\sigma_s^2\mathbf{L}+\sigma_n^2\mathbf{I})^{-\frac{1}{2}}(\sigma_s^2\mathbf{L}+\sigma_n^2\mathbf{I})^{-\frac{1}{2}}\mathbf{V}^T\left(\mathbf{V}\mathbf{L}^{\frac{1}{2}}\mathbf{W}^T\mathbf{s}(n)+\mathbf{e}(n)\right) \\ &= \left(\left((\sigma_s^2\mathbf{L}+\sigma_n^2\mathbf{I})^{-\frac{1}{2}}\right)\mathbf{V}^T\left(\mathbf{V}\mathbf{L}^{\frac{1}{2}}\mathbf{W}^T\mathbf{s}(n)+\mathbf{e}(n)\right)\right)^T (\sigma_s^2\mathbf{L}+\sigma_n^2\mathbf{I})^{-\frac{1}{2}}\mathbf{V}^T\left(\mathbf{V}\mathbf{L}^{\frac{1}{2}}\mathbf{W}^T\mathbf{s}(n)+\mathbf{e}(n)\right) \\ &\qquad\qquad \text{because } (\mathbf{AB})^T=\mathbf{B}^T\mathbf{A}^T \\ &= \left\|(\sigma_s^2\mathbf{L}+\sigma_n^2\mathbf{I})^{-\frac{1}{2}}\mathbf{V}^T\left(\mathbf{V}\mathbf{L}^{\frac{1}{2}}\mathbf{W}^T\mathbf{s}(n)+\mathbf{e}(n)\right)\right\|^2 \qquad \text{because } \mathbf{a}^T\mathbf{a}=\|\mathbf{a}\|^2\end{aligned} \tag{11}$$

A further simplification occurs when is noticed that $\mathbf{V}^T\mathbf{e}(n)$ is also a white noise sequence as $\mathbf{V}$ is an orthonormal matrix. Therefore, $\mathbf{V}^T\mathbf{e}(n)$ is replaced by $\breve{\mathbf{e}}(n)$:

$$\gamma(n) \approx \left\|(\sigma_s^2\mathbf{L}+\sigma_n^2\mathbf{I})^{-\frac{1}{2}}\left(\mathbf{L}^{\frac{1}{2}}\mathbf{W}^T\mathbf{s}(n)+\breve{\mathbf{e}}(n)\right)\right\|^2 \tag{12}$$

Since $\mathbf{L}$ and $\mathbf{I}$ are diagonal matrices and $\mathbf{W}^T\mathbf{s}(n)$ can be represented as $\breve{\mathbf{s}}(n)$, this can be brought back to scalar equations:

$$\gamma(n) \approx \sum_{k=1}^{K}\left(\sqrt{\frac{l_k}{\sigma_s^2 l_k+\sigma_n^2}}\breve{\mathbf{s}}(n-k+1) + \sqrt{\frac{1}{\sigma_s^2 l_k+\sigma_n^2}}\,\breve{\mathbf{e}}(n-k+1)\right)^2 \tag{13}$$

To investigate what is happening, a specific scenario with $\sigma_s^2\ell_k >> \sigma_n^2$ is computed (high signal-to-noise ratio). In this scenario, the following approximations hold true:

$$\frac{l_k}{\sigma_s^2 l_k+\sigma_n^2} \approx \frac{1}{\sigma_s^2} \quad \text{and} \quad \sqrt{\frac{1}{\sigma_s^2 l_k+\sigma_n^2}}\,\breve{\mathbf{e}}(n) \approx 0 \tag{14}$$

The latter approximation is based on the fact that $\breve{\mathbf{e}}(n)$ is on the order of magnitude of σ_n . Substitution in (13) yields:

$$\gamma(n) \approx \sum_{k=1}^{K}\left(\frac{\breve{\mathbf{s}}(n-k+1)}{\sigma_s}\right)^2 = \sum_{k=1}^{K}\left(\frac{\mathbf{s}(n-k+1)}{\sigma_s}\right)^2 \quad \text{because } \|\mathbf{s}(n)\|^2 = \left\|\mathbf{W}^T\mathbf{s}(n)\right\|^2 \tag{15}$$

Now suppose the interval from $n-\mathrm{K}+1$ to n contains m pulses. Then:

$$\sum_{k=1}^{K}\mathbf{s}^2(n-k+1) = ma^2 + (K-m)b^2 \tag{16}$$

Thus, the activity index is:

$$\gamma(n) \approx \frac{ma^2+(K-m)b^2}{\sigma_s^2} = m\frac{a^2-b^2}{\sigma_s^2} + \frac{Kb^2}{\sigma_s^2} \tag{17}$$

In the particular case when $b = 0$, and using (1), this simplifies to:

$$\gamma(n) \approx \frac{m}{P_{rate}(1-P_{rate})} \tag{18}$$

In conclusion, under suitable conditions, the activity index is proportional to the number pulses in an interval of K samples. A property of Poisson point processes is that m, being the number of events in an interval of K samples, has a Poisson distribution with expectation $\mu_m = KP_{rate}$ and variance $\sigma_m^2 = KP_{rate}$. However, since we have a time discrete version the variance is $\sigma_m^2 = KP_{rate}(1-P_{rate})$, whereas the expectation is still $\mu_m = KP_{rate}$. Therefore, it is expected:

$$\mathrm{E}[\gamma] = \frac{K}{1-P_{rate}} \qquad \mathrm{Var}[\gamma] = \frac{K}{P_{rate}(1-P_{rate})} \tag{19}$$

4. Co-activity index

The co-activity index is defined as:

$$\rho(n_0,n) = \bar{\mathbf{x}}(n_0)^T \hat{\mathbf{C}}_{\mathbf{x}}^{-1} \bar{\mathbf{x}}(n) \tag{20}$$

Substitution of (9) and (10) in (20) yield:

$$\begin{aligned}
\rho(n_0,n) \approx & \left(\mathbf{V}\mathbf{L}^{\frac{1}{2}}\mathbf{W}^T\mathbf{s}(n_0)+\mathbf{e}(n_0)\right)^T \mathbf{V}(\sigma_s^2\mathbf{L}+\sigma_n^2\mathbf{I})^{-\frac{1}{2}}(\sigma_s^2\mathbf{L}+\sigma_n^2\mathbf{I})^{-\frac{1}{2}}\mathbf{V}^T\left(\mathbf{V}\mathbf{L}^{\frac{1}{2}}\mathbf{W}^T\mathbf{s}(n)+\mathbf{e}(n)\right) \\
= & \left(\mathbf{V}\mathbf{L}^{\frac{1}{2}}\mathbf{W}^T\mathbf{s}(n_0)\right)^T \mathbf{V}(\sigma_s^2\mathbf{L}+\sigma_n^2\mathbf{I})^{-\frac{1}{2}}(\sigma_s^2\mathbf{L}+\sigma_n^2\mathbf{I})^{-\frac{1}{2}}\mathbf{V}^T\left(\mathbf{V}\mathbf{L}^{\frac{1}{2}}\mathbf{W}^T\mathbf{s}(n)\right)+ \\
& \left(\mathbf{e}(n_0)\right)^T \mathbf{V}(\sigma_s^2\mathbf{L}+\sigma_n^2\mathbf{I})^{-\frac{1}{2}}(\sigma_s^2\mathbf{L}+\sigma_n^2\mathbf{I})^{-\frac{1}{2}}\mathbf{V}^T\left(\mathbf{e}(n)\right)+ \\
& \left(\mathbf{V}\mathbf{L}^{\frac{1}{2}}\mathbf{W}^T\mathbf{s}(n_0)\right)^T \mathbf{V}(\sigma_s^2\mathbf{L}+\sigma_n^2\mathbf{I})^{-\frac{1}{2}}(\sigma_s^2\mathbf{L}+\sigma_n^2\mathbf{I})^{-\frac{1}{2}}\mathbf{V}^T\left(\mathbf{e}(n)\right)+ \\
& \left(\mathbf{e}(n_0)\right)^T \mathbf{V}(\sigma_s^2\mathbf{L}+\sigma_n^2\mathbf{I})^{-\frac{1}{2}}(\sigma_s^2\mathbf{L}+\sigma_n^2\mathbf{I})^{-\frac{1}{2}}\mathbf{V}^T\left(\mathbf{V}\mathbf{L}^{\frac{1}{2}}\mathbf{W}^T\mathbf{s}(n)\right)
\end{aligned} \tag{21}$$

If the signal components are much larger than the noise components, the first term prevails. In that case, $\sigma_n^2\mathbf{I}$ will be much less than $\sigma_s^2\mathbf{L}$ and can be neglected. Thus:

$$\begin{aligned}
\rho(n_0,n) \approx & \left(\mathbf{V}\mathbf{L}^{\frac{1}{2}}\mathbf{W}^T\mathbf{s}(n_0)\right)^T \mathbf{V}(\sigma_s^2\mathbf{L})^{-\frac{1}{2}}(\sigma_s^2\mathbf{L})^{-\frac{1}{2}}\mathbf{V}^T\left(\mathbf{V}\mathbf{L}^{\frac{1}{2}}\mathbf{W}^T\mathbf{s}(n)\right) \\
= & \ \mathbf{s}^T(n_0)\sigma_s^{-2}\mathbf{s}(n)
\end{aligned} \tag{22}$$

The conclusion is that $\rho(n_0,n)$ is proportional to the number of pulses that the records $\bar{\mathbf{x}}(n_0)$ and $\bar{\mathbf{x}}(n)$ share at the same points in time.

A3 – The KmCKC algorithm

```
function [IPTs,shape]  = KmCKCnew(sEMG,K,nMU,k,nClus,r,Np,h)
%% function for sEMG decomposition
% derived from Ning et al. (2015) - Surface EMG decomposition based on K-means
clustering and convolution kernel compensation
% sEMG  = sEMG of tongue of a certain task
% K     = number of delays to be created
% N     = number of samples
% M     = number of electrodes
% nMU   = the maximum number of MU that can be extracted
% r     = number of different highest peaks
% Np    = step for higher r
% h     = number of repeats of step 4
% k     = number of highest peak in sn1
% nClus = number of clusters during KMC clustering

%% step 1 - create delays and covariance matrix
M = size(sEMG,1);
N = size(sEMG,2);

place  = 1;
X      = zeros(K*M,N);
for i = 1:M
    for j = 0:K-1
        X(place,:) = circshift(sEMG(i,:),j,2);
        place = place + 1;
    end
end
Cxx = cov(X');

%% step 2 - compute y(n), n0, sn0(n), n1, sn1 and PHInc
y = sum(X.*(Cxx\X));

for Nmdl = 1:nMU
[~,ind] = sort(y);
n0 = ind(round(N/2));
sn0 = sum(X(:,n0).*(Cxx\X));

% maximum value of sn0 on time n1
maxsn0  = max(sn0);
[~, n1] = find(sn0==maxsn0);

% compute sn1(n)
sn1 = sum(X(:,n1).*(Cxx\X));

% k highest peaks of sn1 (PHInc)
[~, PHInc] = findpeaks(sn1,'SortStr','descend','NPeaks',k);

%% step 3 - KMC clustering, PHInv, Cxsj0 and sj0
% generate initial cluster centers, in this case a space-diagonal equally
spaced
X_PHInc = X(:,PHInc)';
minX    = min(X_PHInc,[],1);
maxX    = max(X_PHInc,[],1);
```

```
nsamp   = size(X_PHInc,1);
initialcenters = repmat(minX, nsamp, 1) + bsxfun(@times, (0:nsamp-1).', (maxX
- minX) ./ (nsamp-1));
initialcenters = initialcenters(1:nClus,:);

% KMC clustering
KMC = kmeans(X_PHInc,nClus,'start',initialcenters);

% group with largest number of elements
[a,~]       = hist(KMC,unique(KMC));
[~, group]  = find(a==max(a));
[KMCloc, ~] = find(KMC==group);
PHInv       = PHInc(1,KMCloc);

% cross-correlation between estimated pulse train and all observations
Cxsj0 = mean(X(:,PHInv),2);

%% step (3), 4 and 5 - illiterate estimation of pulse train
% estimation of initial pulse train
sj      = zeros(h+2,N);
sj(1,:) = sum((Cxsj0.*(Cxx\X)));

for i = 1:h
    r = r + Np;
    [~, PHI] = findpeaks(sj(i,:),'SortStr','descend','NPeaks',r);
    Cxsj = mean(X(:,PHI),2);
    sj(i+1,:) = sum((Cxsj.*(Cxx\X)));
end
shape(Nmdl,:) = Cxsj';
IPTs(Nmdl,:) = sj(h+1,:);

%% step 6 - remove peaks from y
y(1,PHInv) = 0;

clearvars -except sEMGb EMG X y Nmdl nMU sources IPTs r Np h N H Hparm k K nMU
r Np Cxx nClus shape;
end
end
```

A4 – Simulation of simplified representation of sEMG

```
function [X,sources,H,P] = simulateEMG(NS,PR,Hparm)
%% simulation of a sEMG
% NS         = number of EMG samples
% PR         = pulse rate per source
% Hparm(i,j) = parameter of impulse response from source i to electrode j

[M,N] = size(Hparm);
% M = number of electrodes
% N = number of sources

DOFmax = max(Hparm(:));
P      = ceil(DOFmax+3*sqrt(DOFmax));    % maximal length neccessary for
impulse response

%% generate sources
sources = zeros(N,NS);

% random locations of impulses
for i = 1:N                          % loop through sources
    impulse = sort(randperm(NS,round(NS*PR)));
    for j = 1:size(impulse,2)-1
        if impulse(j+1)-impulse(j) < 0.25*P     % set distance of minimal
0.25*P between impulses
            impulse(j+1)=impulse(j);
        end
    end
    impulse = unique(impulse);
    sources(i,impulse) = 1;
end

%% generate the mixing matrix H
H      = zeros(M,P*N);
for i = 1:N                % loop through sources
    for j = 1:M            % loop through electrodes
        h = chi2pdf(0:P-1,Hparm(j,i));  % create impulse response
        H(j,(i-1)*P+1:i*P) = h;     % put impulse response in right place of H
        hlist{j,i} = h;             % overview (list) of H
    end
end

%% generate sEMG
X = zeros(M,NS);
for i = 1:N
    for j = 1:M
        X(j,:) = X(j,:) + conv(sources(i,:),hlist{j,i},'same');
    end
end
end
```

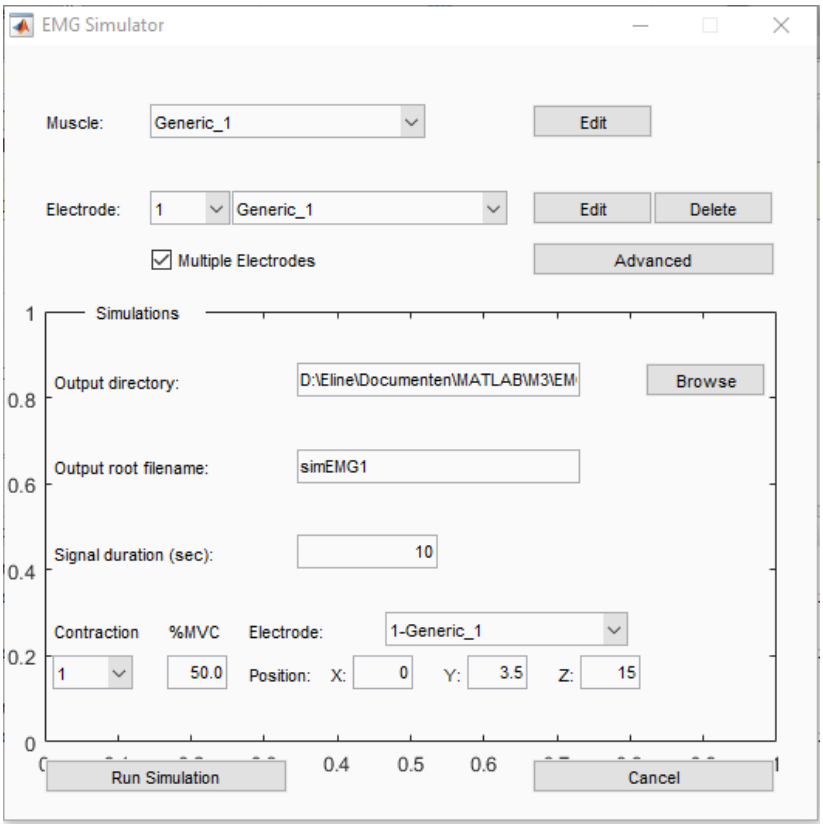

Figure A5 – Main window of the EMG simulator. With settings for electrode 1 of EMG 1. [61]

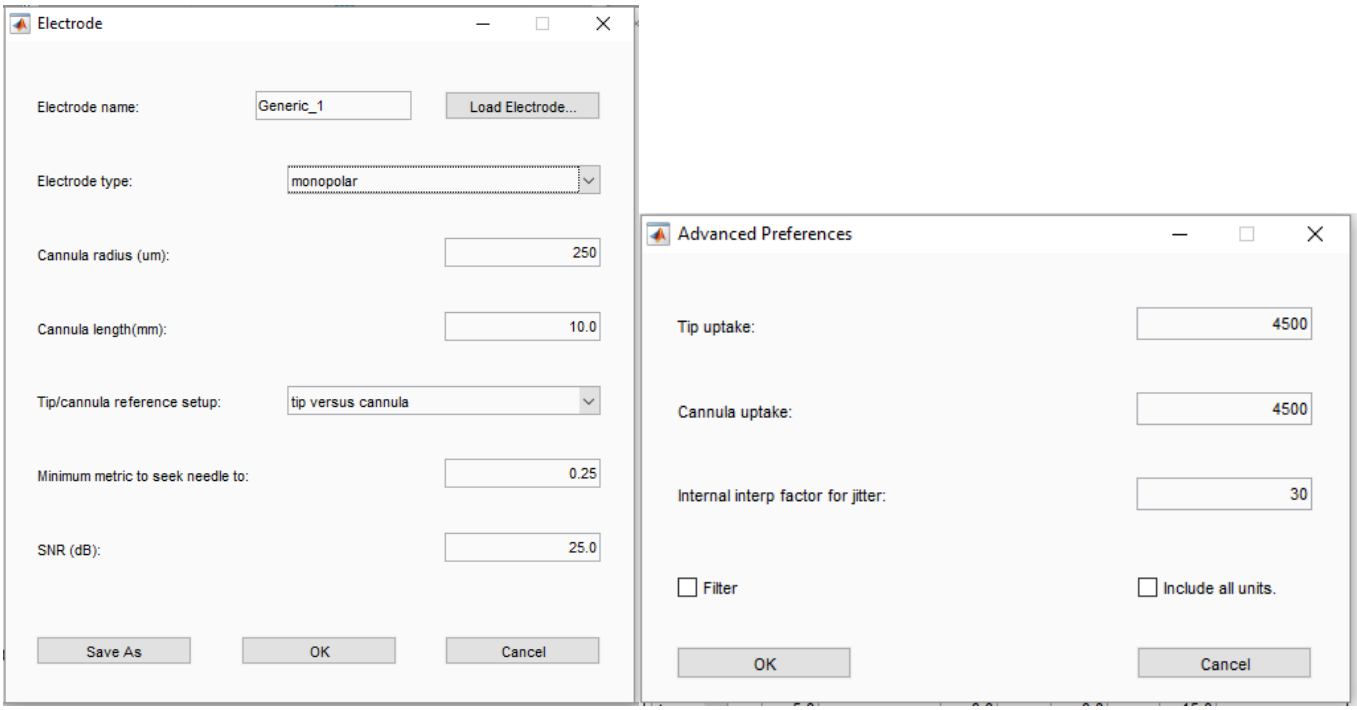

Figure A6 – Electrode windows of the EMG simulator. With settings for all EMGs. [61]

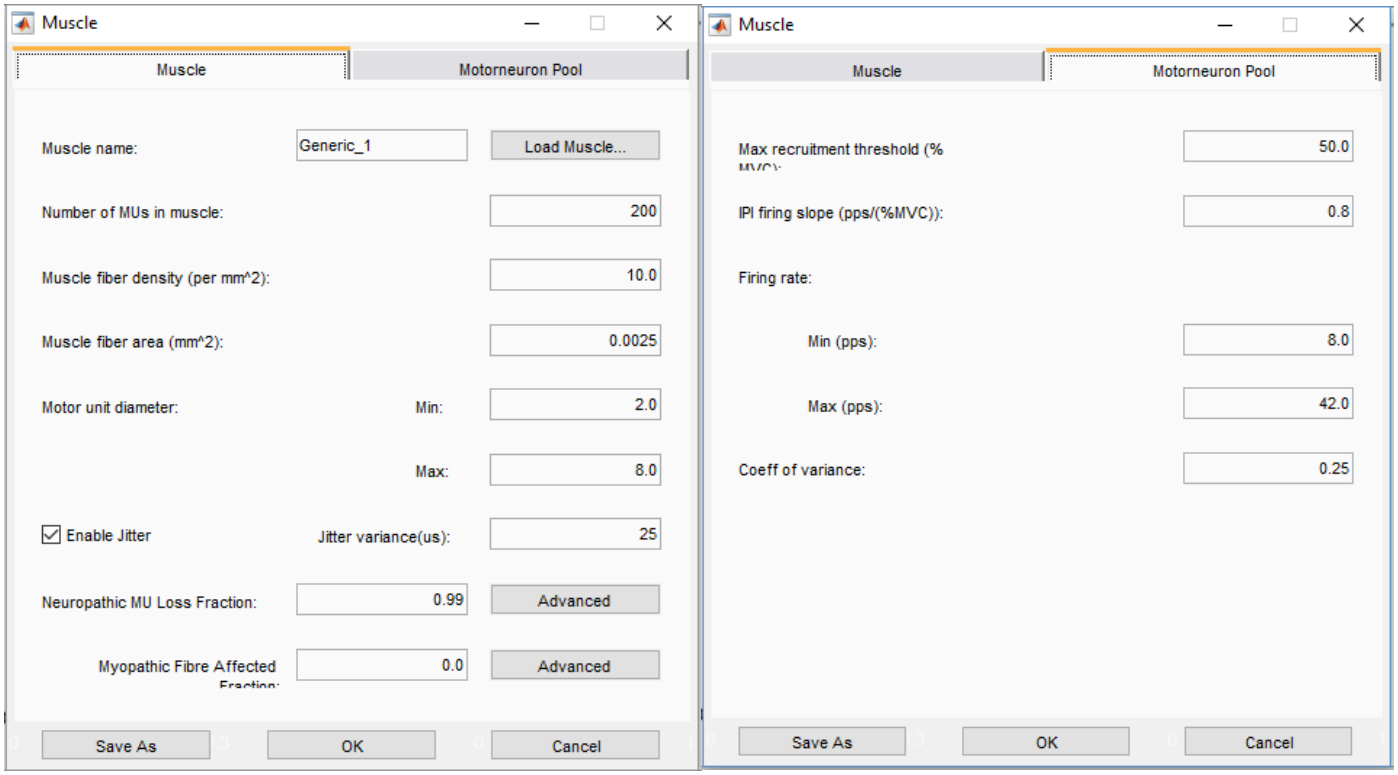

Figure A7 – Muscle windows of the EMG simulator. With 'neuropathic MU loss fraction' for EMG 1. The other settings concern all EMGs. [61]

A8 – Match estimated MUAPT to original MUAPT

```
function [IPT,IPTn]  = matchIPTsource(IPTs,MUs)
%% function to match IPT to source (MU)
% IPTs    = IPTs following from KmCKC
% sources = original MUAPS of simulated EMG
place    = 1;
Q        = 50;  % number of delays for finding match
IPTdelay = zeros(size(IPTs,1)*50,size(IPTs,2));
for i = 1:size(IPTs,1)
    for q = 0:Q-1
        if q < 25
           IPTdelay(place,:) = circshift(IPTs(i,:),q,2);
        else
           s = q-(0.5*Q);
           IPTdelay(place,:) = circshift(IPTs(i,:),-s,2);
        end
        place = place + 1;
    end
end
match         = MUs*IPTdelay';
matchIPT      = max(match,[],2);
[IPTn, shift] = find(matchIPT==match);
IPT(IPTn,:)   = IPTdelay(shift,:);
end
```

A9 – Two percentage performance measures per estimated MUAPT

```
function [pcorrect,povershoot]  = pscore(IPT,MUs,frac)
%% function for percentage score of KmCKC outcome compared to original sources
% IPTs    = IPTs following from KmCKC
% sources = original MUAPS of simulated EMG
% frac    = fraction for determination of the threshold for peak selection
dummy  = max(IPT,[],2);
thresh = dummy*frac;
for i = 1:size(MUs,1)
    [peak,loc] = findpeaks(IPT(i,:),'MinPeakHeight',thresh(i,1));
    pks{i} = [peak;loc];
end
for i = 1:size(MUs,1)
    [pulse,loc] = findpeaks(MUs(i,:),'MinPeakHeight',0.9);
    pls{i} = [pulse;loc];
end
for i = 1:size(IPT,1)
    correct       = ismember(pls{i}(2,:),pks{i}(2,:));
    pcorrect(i)   = (sum(correct)/size(pls{i},2))*100;
    povershoot(i) = ((size(pks{i},2)-sum(correct))/sum(correct))*100;
end
end
```

Table A10 – Results of the first random search for parameter optimization. Where mean correct, and mean overshoot are the averaged values within the identified MUAPTs.

Best	Number of identified MUAPTs	Mean correct [%]	Mean overshoot [%]	K	k	nClus	r	h	fc	frac
EMG 1										
First	2	92.9	11.1	8	200	5	16	1	30	0.58
Second	2	91.5	14.1	8	150	2	7	2	40	0.29
EMG 2										
First	2	94.4	4.5	10	220	2	5	6	15	0.48
Second	2	93.1	4.7	10	210	3	7	2	40	0.56
EMG 3										
First	3	93.3	114.6	19	30	2	12	4	10	0.29
Second	3	92.2	124.6	20	180	4	15	4	50	0.34
EMG 4										
First	2	88.4	270.6	15	110	5	6	21	35	0.26
Second	1	88.2	10.0	14	80	5	13	2	30	0.61
EMG 5										
First	4	92.1	7.1	3	10	4	6	1	15	0.44
Second	3	93.2	5.3	8	20	2	11	1	40	0.38
EMG 6										
First	2	88.6	354.8	14	70	2	17	9	20	0.26
Second	2	88.6	383.9	14	80	5	11	13	10	0.25

Figure A11 - Results of the first random search for parameter optimization. All EMGs and their seven parameters are visualised. The colours indicate the number of identified MUAPTs, defined as ≥ 88% correct estimated excitations. The red frames indicate the parameter values used for the second random search for parameter optimization, defined by the best two estimated MUAPTs (overshoot percentage incorporated).